École Polytechnique Fédérale de Lausanne
PV-Lab Neuchâtel, 2019

Fully Evaporated Solar Cells Exploiting High-Bandgap $CsPbI_2Br$

Characterisation and device engineering

POLITECNICO DI TORINO

Assunta Scognamillo
Supervisor(s): Andrea Lamberti, Jeangros Quentin, Fan Fu

A thesis submitted in fulfilment of the requirements for the degree of:
Master of Engineering in Nanotechnologies for ICTs

Acknowledgements

Firstly, I would like to thank Andrea Lamberti from the Politecnico di Torino, who offered me his expertise and worked with me to finish this thesis in a qualitative and timely manner. I'd like to acknowledge Fan Fu from Empa for giving me the possibility to continue his project and providing me with the basic directions. Furthermore, Jeangros Quentin from PV-Lab (EPFL), who contributed his field-specific knowledge to subtly guide my exploration of the subject. Thanks also go out to my PV-Lab colleagues for their ever-present informative and moral support, Peter Fiala and Ricardo Razera in particular.

I would like to thank my parents, who sustained me economically and personally throughout my studies.

Another person who deserves to be thanked is my friend Eva, who was there by my side to encourage my studies throughout my path at the Politecnico di Torino, and motivated me to continue the work on this thesis.

Lastly, I would like to offer a warm thanks to Chris Baljé from the Delft University of Technology, who acted as my second reader to offer me many suggestions and advice on how to manage the large amount of information that had to be processed for this thesis. I would not be motivated and determined in the same manner without him in the last year of my path.

Politecnico di Torino

Torino, October 9, 2019

Assunta Scognamillo

Abstract

To push the Shockley-Queisser limit for photovoltaic cell PCE, tunable perovskite-based top cells for triple-junctions have been investigated. The tunability of the bandgap of $CsPbI_2Br$, in combination with its photo-physical properties and thermal stability, makes the material ideal for this application, but it needs to be engineered and deeply characterised. Furthermore, being fully evaporated, the cell can avoid the annealing step usually needed, preventing changes in the underlying tandem induced by high temperatures. The objective of this thesis is to investigate the air- and photo-stability of co-evaporated, high-bandgap $CsPbI_2Br$-based solar cells, and to analyse and engineer this cell for triple-junction applicability. Dual source thermal co-evaporation of CsBr and PbI_2 was used to form a photoactive $CsPbI_2Br$ layer, with a bandgap of 1.92 eV. TEM, SEM, XRD, PL, UV-Vis-NIR, PDS, EQE, and J-V measurements were employed to analyse its air- and photo-stability, and its photovoltaic parameters in a single junction. The effects of various low-temperature annealing steps in a controlled atmosphere were compared. The air-stability mainly depends on phase transition under humidity. Stoichiometric and CsBr-rich perovskite exhibit a distorted perovskite γ-phase, making them relatively air-stable. Moreover, the influence of the thin film thickness has been investigated, revealing that $CsPbI_2Br$ layers over 185 nm are significantly more air-stable than thinner layers. The choice of HTL material strongly influences the phase transition rate of the perovskite. Concerning photo-stability, it depends on phase segregation, influenced by layer thickness, laser intensity, surrounding atmosphere, and crystal structure. Thin $CsPbI_2Br$ layers exhibit a quicker phase segregation than thicker layers. Annealed samples show a changed crystal structure, notably the absence of a δ-phase XRD peak. The optimal layer thicknesses for the investigated configurations are 190 nm for $CsPbI_2Br$, 10 nm for Spiro-TTB, 30 nm for C_{60}. A record PCE for this composition is obtained of 9.33% (J_{sc}=12.88 mA/cm^2, V_{oc}=1.01 V, FF=71.7%, stabilised PCE=8.82%), with those thicknesses, using a device structure of glass/ITO/Spiro-TTB/$CsPbI_2Br$/C_{60}/TmPyPb/Ag. The air- and photo-stability of the perovskite are increased by engineering of the crystal structure and adjacent layers. The effects of phase segregation distinguished in this thesis can be explained through a polaronic model, and are significantly reduced using a $CsPbI_2Br$ thickness above 185 nm, an inert atmosphere, and an annealing at 80°. However, the annealing step lowers the J_{sc} due to an introduction of defects.

Keywords – Master thesis, CsPbI2Br, perovskite, co-evaporated, all-inorganic, photovoltaic, solar cell, fully evaporated, characterisation, device engineering, annealing, photo-stability, air-stability, phase segregation, phase transition, degradation, efficiency, stability, NiO, Spiro-TTB, BF-DPB, Spiro-MeOTAD, C60, TmPyPb, interface, single-junction, triple-junction, TEM, SEM, XRD, PL, UV-Vis-NIR, PDS, EQE, J-V, cubic, orthorhombic, crystal structure

Contents

List of Figures

List of Symbols and Abbreviations

Abbreviation/Symbol	Description
Ag	Silver
BF	Bright field
BF-DPB	N4,N4'-Bis(9,9-dimethyl-9H-fluoren-2-yl)-N4,N4'-diphenylbiphenyl-4,4'-diamine
Br	Bromide
BSE	Back-scattered electrons
c	Speed of light in vacuum
C_{60}	[60]fullerene
Ca	Calcium
$CaTiO_3$	Calcium titanate
CCD	Charged coupled device
CdTe	Cadmium telluride
CGIS	Copper indium gallium selenide
$CH_3NH_3PbBr_3$	Methylammonium lead tribromide
$CH_3NH_3PbCl_3$	Methylammonium lead trichloride
$CH_3NH_3PbI_3$	Methylammonium lead triiodide
$CH_3NH_3PbX_3$	Methylammonium lead halides where $X = I$, Br, or Cl
Cs	Caesium
CsBr	Caesium bromide
CSEM	Swiss Center for Electronics and Microtechnology
c-Si	Crystalline silicon
$CsPbI_2Br$	Ceasium lead iodide bromide
$CsPbX_3$	Ceasium lead halides
CzTS	Copper zinc tin sulfide
d	Interplanar distance for a crystalline solid
DSSC	Dye-sensitised solar cell
DUT	Device under test
e	Elementary charge
EBL	Electron blocking layer
$E_{photons}$	Photon energy
EQE	External quantum efficiency
ETL	Electron transporting layer
FAI	Formamidinium iodide
FET	Field-effect transistor

Abbreviation/Symbol	Description
FF	Fill factor
FIB	Focused ion beam
Ga	Gallium
GaAs	Gallium arsenide
h	Planck constant
H_2O	Dihydrogen Monoxide
HBL	Hole blocking layer
HOMO	Highest occupied molecular orbital
HTL	Hole transport layer
I^-	Iodide
$I_{SC,DUT}$	Short circuit current of the device under test
$I_{SC,monitor}$	Short circuit current of the monitor cell
$I_{SC,ref}$	Short circuit current of a reference cell
I_2	Iodine
IEA	International energy agency
InGaAs	Indium gallium arsenide
IR	Infra red
ITO	Indium tin oxide
J	Current density
J_0	Reverse saturation current density
J_D	Diode current density
J_{mpp}	Density of current at maximum power point
J_{ph}	Current density of photons
J_{sc}	Short circuit current density
k_B	Boltzman constant
KRICT	Korean research institute of chemical technology
LCOE	Levelized cost of electricity
LED	Light emitting diode
LUMO	Lowest unocuppied molecular orbital
MAI	Methylammonium iodide
$MAPb(I_{1-x}Br_x)_3$	Methylammonium lead iodide bromide
MIT	Massachusetts institute of technology
MoO_3	Molybdenum(VI) oxide

Abbreviation/Symbol	Description
mpp	Maximum power point
$n_{\text{electrons}}$	Number of generated electrons
n_{photons}	Number of incident photons
N_2	Nitrogen
NiO	Nickel oxide
NREL	The National Renewable Energy Laboratory
O^-	Oxygen ion
O_2	Dioxygen
Oxford PV	Oxford photovoltaic
Pb	Lead
Pb^{2+}	Lead(II) ion
PbI_2	Lead iodide
PCE	Power conversion efficiency
PDS	Photothermal deflection spectroscopy
P_{in}	Incident power
PL	Photoluminescence
P_{mpp}	Power at maximum power point
PMT	Photomultiplier tube
P_{out}	Output power
PV	Photovoltaics
PVD	Physical Vapor Deposition
Pv-lab	Photovoltaic laboratory
q	Elementary charge
QE	Quantum efficiency
R_A	Ionic radius of A cation
R_B	Ionic radius of B cation
R_X	Ionic radius of halides
R_s	Shunt resistance
R_{sh}	Series resistance
SE	Secondary electrons
SEM	Scanning electron microscopy
Si	Silicon
Sn	Tin

Abbreviation/Symbol	Description
Spiro-OMeTAD	2,2´,7,7´-tetrakis-(N,N-di-p-methoxyphenylamine)9,9´-spirobifluorene
Spiro-TTB	2,2',7,7'-Tetra(N,N -di-p -tolyl)amino-9,9-spirobifluorene
S-Q	Shockley-Queisser
SR	Spectral response
SR_{DUT}	Spectral response of the device under test
SR_{REF}	Spectral response of a reference cell
STEM BF	Scanning Transmission Electron Microscopy bright field
STEM EDX	Scanning Transmission Electron Microscopy energy dispersive X-ray
STEM HAADF	Scanning Transmission Electron Microscopy High-angle annular dark-field imaging
T	temperature
t	tolerance factor
TEM	Transmission electron microscopy
Ti^{3+}	Titanium(III) ion titanous ion
TiO_2	Titanium dioxide
TmPyPb	1,3,5-Tris(3-pyridyl-3-phenyl)benzene
UV-VIS-NIR	Ultraviolet-visible-near infra-red
V_{mpp}	Voltage at maximum power point
V_{oc}	Open circuit voltage
XRD	X-ray diffraction
Zn	Zinc
ZnO	Zinc oxide

Greek letters	Description
λ	Wavelength
μ	Octahedral factor
ν	Frequency

1 Introduction

1.1 Context

In the recent years, the area of renewable energy has experienced rapid growth. This was mainly driven by a decrease in costs due to technological developments and the growing need for a clean energy alternative to traditional fossil fuels, in anticipation of the evolving greenhouse effect and a potential future fuel crisis. Since a fuel crisis would imply a steep increase in price for classical energy sources (coal, oil, gas), it naturally drives the innovation towards more sustainable energy sources. Facilities for different renewable energies are being funded and installed in a majority of countries. Currently, wind power and photovoltaics are the most commonly exploited renewable energy principles. However, the effective costs of exploitation, storage, and transport continue to show significant opportunities for optimisation. In light of this, the international energy agency (IEA) collaborates with stakeholders through in-depth market analysis, regulatory advice for governments, and the provision of a clear sight on the necessary technology for a rapid scale-up of the electricity and heat produced through renewable sources. According to the IEA [1] renewable energy will provide up to 30% of the global demand in 2023. Photovoltaic energy will produce a large part of the projected renewable energy. A particularly large global wave of growth in photovoltaic energy production is expected until 2023, primarily attributable to Chinese investments [1]. This thesis investigated specifically photovoltaic cells based on co-evaporated all-inorganic high-bandgap $CsPbI_2Br$.

1.2 Co-evaporated $CsPbI_2Br$ state-of-the-art

The perovskite layer that is analysed in this thesis is obtained through thermal co-evaporation. At the writing of this paper, a literature gap exists for the investigation of thermally co-evaporated $CsPbI_2Br$ with a 1.92 eV bandgap, especially without the use of an annealing step. Only three analyses were reported of pure co-evaporated $CsPbI_2Br$, with slight differences in composition, resulting in a variation of their bandgaps. Firstly, the most relevant result for this thesis was reported by Qingshan Ma in 2017 for a bandgap of 1.90 eV [2], reaching a PCE of 7.7% under reverse scan and a stabilised PCE of 6.7% for a 0.159 cm^2 active area, and a PCE of 6.8% under reverse scan and a stabilised PCE of 5.5% for a 1.2 cm^2 active area. Secondly, in January 2017, Chen et al. used a 1.82 eV bandgap energy to reach a PCE of 6.8%, with a V_{oc} of 1.1 V, a J_{sc} of 10.7 mA/cm^2, and a FF of 58%. Furthermore, Chen et al. used the same bandgap in combination with annealing (at 260° for 80s) to reach a a PCE of 11.8% in reverse scan and a stabilised

PCE of 11.5% for an annealed cell [3]. Lastly, in January 2019, Park et al. reported an efficiency of 5.7% for a bandgap of 1.97 eV, for a device that used an annealed perovskite layer (300° for 60s) [4].

The stability and degradation factors of $CsPbI_2Br$ were analysed by several researchers. Most notably, Mariotti et al. reviewed and investigated the behaviour of spin coated $CsPbI_2Br$ under humidity, oxygen and ozone. Humidity was the only singular factor to fully convert cubic phase perovskite into its non-photoactive orthorhombic phase in less than a week. Additionally, it was proven that $CsPbI_2Br$ does not react with an inert N_2 atmosphere. Furthermore, Mariotti et al. noted that the $CsPbI_2Br$ phase transition turns the cubic phase with a bandgap of 1.92 eV into an orthorhombic phase with a bandgap of 2.85 eV. Lastly, it was observed that the phase transition of an inorganic perovskite layer could be reversed through high temperature annealing, in contrast to the complete decomposition of organic perovskite, resulting from the loss of its halides or organic cations [5].

1.3 Thesis statement and goals

This thesis has two main aims. The first is to investigate the stability of a co-evaporated, high-bandgap $CsPbI_2Br$ layer, focusing on phase transition and phase segregation phenomena. As a key driving factor for this investigation is the low-temperature manufacturing process necessary for a multi-junction top cell, the base samples will not be annealed. The second is to analyse and optimise solar cells based on this photoactive layer for usage in triple-junctions, focusing on the short circuit current density, open circuit voltage, fill factor, and hysteretic behaviour.

For the investigation of the stability, the goal is to create clarity on the causes and effects of the observed phenomena, mainly phase transition and phase segregation. As it can be hypothesised that improving the stability of a cell without changing its chemical composition decreases its attainable efficiency, it is desirable to find a suitable trade-off between both factors. Furthermore, a thorough understanding of the phase segregation and phase transition of co-evaporated, inorganic perovskite could form the basis for a large improvement of the current state-of-the-art perovskite solar cell fabrication.

Then, for the analysis and optimisation of the cell efficiency in this bandgap, the goal is to engineer the high-bandgap perovskite based cell for advantageous application as a top cell of a triple-junction. To achieve this, it is important to consider the thickness of the different layers, as well as their interaction and interfaces. This thesis focuses on the analysis of the hole transport layer (HTL), the photoactive layer, the electron transport layer (ETL), and the interfaces between these layers.

1.4 Thesis overview

This thesis consists mainly of the measurement and analysis of photovoltaic samples with varying properties, in order to characterise the influence of these properties on the functioning of the cell. The information obtained from these measurements is then used to engineer a device based on the found principles, to see if an improvement can be made on the established literature.

The general structure for the thesis after this introductory chapter can be summarised as follows: Firstly, before the measurements are introduced, a basic understanding of the driving principles behind the investigated solar cells is provided in Chapter 2, and the current state-of-art is discussed. Secondly, in Chapter 3, the methodology for the performed analyses is given alongside a concise overview of the material and cell properties relevant for the work in this thesis. Thirdly, the results of the performed measurements and analyses are portrayed in Chapter 4, where there is a strong focus on the investigation of the phase transition and phase segregation phenomena, respectively in section 4.1.1 and section 4.4. Also in Chapter 4, sections 4.2 and 4.3 aim to characterise the perovskite layer morphology, crystallinity, and chemical composition. Fourthly, an attempt is made to engineer the investigated device for efficiency and stability in Chapter 5. After a description of the optimisation process, a detailed account of the resulting record cells is given in section 5.7. Lastly, Chapter 6 summarises and discusses the conclusions that can be taken from this thesis, and outlines a number of recommendations for future work based on the obtained results.

2 Background

2.1 Photovoltaic effect

The photovoltaic effect is the underlying principle for solar cells, enabling them to generate renewable electricity from sunlight. The effect was discovered by Becquerel in 1839, when an electrode exposed to light in an electrolytic solution produced electricity. Over a century after this discovery, in 1954, the first silicon solar cell was made, having a conversion efficiency of 6%. In 1985, this efficiency had risen to 20%, but the large production costs were detrimental for global application. Since then, technological developments decreased the manufacturing costs and confirmed silicon to be an appropriate material for solar cell production, mainly because its availability in large quantities and its non-toxicity. The current record efficiency for a silicon hetero-junction of 26.7% was achieved in 2017 [6]. This efficiency is remarkably near to the Shockley-Queisser limit, which is evaluated at 29.43% for the silicon bandgap of 1.1 eV under usual AM 1.5G conditions [7]. High cell efficiency decreases the levelised cost of electricity (LCOE), so that cheaper photovoltaic installations are possible. Nonetheless, although the LCOE depends on the solar cell production and efficiency, it also depends significantly on transport costs, module creation, grid connection, site preparation, and maintenance, which are costs that are difficult to further optimise. However, maximising the cell efficiency is a method to decrease the LCOE [8, 9].

2.2 Shockley-Queisser limit

Solar cells generate a hole-electron pair after a photon absorption. Photons are absorbed only if their energy is equal to or higher than the bandgap energy. If it is higher, their energy is not completely converted and part is lost in charge carrier thermalisation. The Shockley-Queisser limit or detailed balance limit can be described as the maximum efficiency that a p-n junction can reach, where the two main limitations are the unavoidable presence of recombination, which can be seen as a opposite process to the formation of an electron-hole couple, and the out-of-spectrum photons with energy that cannot be properly absorbed by the bandgap of the solar cell. Recombination of the carriers represents a problem for solar cells because it causes a decrease in the short circuit current density and open circuit voltage, and consequently in the efficiency. Possible recombination mechanisms include band tail recombination, Auger recombination and recombination due to defects in bulk, surface or interface [10]. Other losses derive from contact losses, solar radiation power fluctuation, and the angle of incidence of the radiation beam. The maximum Shockley-Queisser limit for a p-n single junction was recalculated in 2016 to be at 33.7% for a bandgap of 1.34 eV [6]. It is determined using the maximum theoretical power output of a cell, at a voltage equal to that bandgap energy and a current generated by photons with energy superior to that of the bandgap, and with the maximum possible extraction rate of the generated carriers. However, the Shockley Queisser limit does only apply to single junctions. Therefore, an increased cell efficiency can be obtained through use of multiple junctions. Most recently a record efficiency of 47.1% has been reached under a light concentrator by a 4-junction solar cell, based on materials of the III-V groups [11, 10]. Nevertheless, the production of such a cell is still too expensive to be an economically viable option for commercial distribution.

2.3 Thin film solar cells

Solar cells are classified per generation. The first generation consists of silicon wafer based solar cells, the second generation introduces thin films, and the third generation includes Dye-sensitised solar cells (DSSC), thin films, multi-junctions, and quantum solar cells. Currently, research on thin film solar cells is done mostly with GaAs, CdTe, CIGS, CZTS, amorphous silicon, perovskite and organic solar cells [10]. The photoactive layer of these thin films is on a scale of only a few micrometers, and from 2010 their maximum efficiency has grown more rapid than silicon solar cells. The current record efficiencies and limitations of these materials is discussed as follows, always in reference to a single junction cell configuration:

- DSSCs can be produced using materials with low costs and toxicity compared to other solar cell technologies. The main drawback is the low thermal stability of the photo-active dye. DSSCs have reached an efficiency of 12.3% [12].
- CGIS solar cells have a bandgap that can be tuned from 1 to 2.4 eV. An efficiency of 23.35% for a bandgap of 1.13 eV has been reached [8, 13]. However, CGIS is not suitable for tandem application because of a low efficiency for higher bandgaps. Furthermore, the inclusion of Indium is a limitation, because of its rare and expensive nature;
- CdTe solar cells have reached an efficiency of 22.1% for a bandgap of 1.43 eV [10, 13], near the ideal bandgap of 1.34 eV [6], but recombination losses at the interface and in the crystal grains cause efficiency losses. Furthermore, cadmium is a toxic element and tellurium is not widely available;
- CZTS, with a tunable bandgap from 1 eV to 1.6 eV, has a comparable chemical structure to CGIS, where Indium is substituted by Zn and the Ga by Sn. It has only reached a maximum efficiency of 12.6% [10] due to interface extraction losses

and bulk recombination;

- Organic solar cells are non-toxic, flexible and low cost, but contain carrier traps and have low crystallinity. For this reason, the current record efficiency is only 16.4% [10, 13];
- Amorphous silicon based cells have a bandgap around 1.7-1.8 eV, far from the ideal bandgap of 1.34 eV [6]. Additionally, the short circuit current density of amorphous silicon is strongly limited by the necessity to have a layer thickness that allows for photon absorption, as this thick layer also causes a large recombination rate. Mainly due to this issue, the reached efficiency is only 10.2% [10];
- Perovskite solar cells have reached an efficiency of 25.2% in the past 10 years [11]. They have a very high Voc compared to the other solar cells. The main issues are the absorption of part of the spectrum by the hole transport layer (HTL) and the contacts, and the imperfect crystalline structure of perovskite that lowers the current;
- GaAs was used to obtain the highest efficiency for a single junction in AM 1.5G conditions, equal to 29.1% [13]. Nonetheless, the drawbacks of GaAs as compared to silicon are its lower heat resistance and its higher price, and the inclusion of arsenic is very dangerous for the health [10, 8].

In figure 2.1, the growth trend of the mentioned solar cells is schematised:

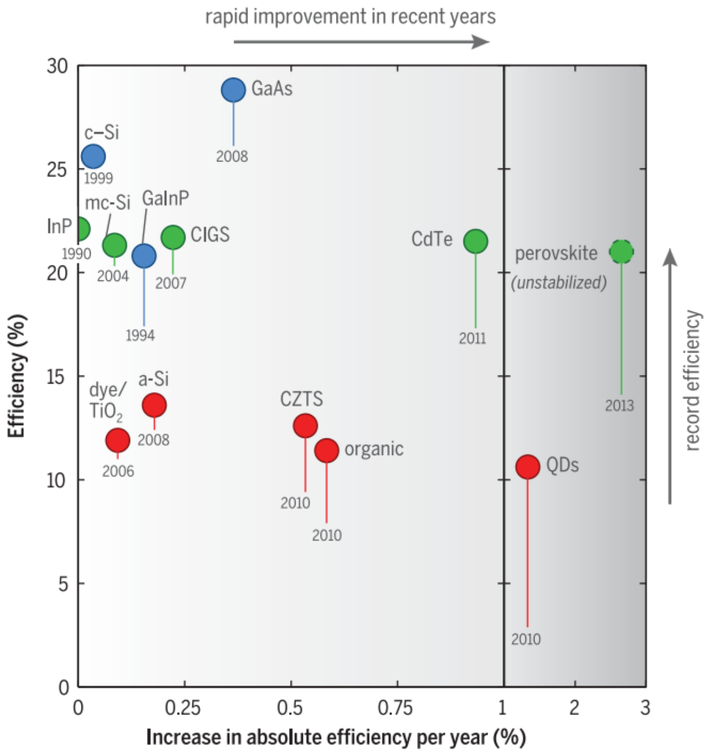

Figure 2.1: Yearly efficiency increase of solar cells based on different photoactive layer materials (2016) [10]

The NREL provides the data of efficiency growth for single junctions and multiple junctions, this data is portrayed in figure 2.2:

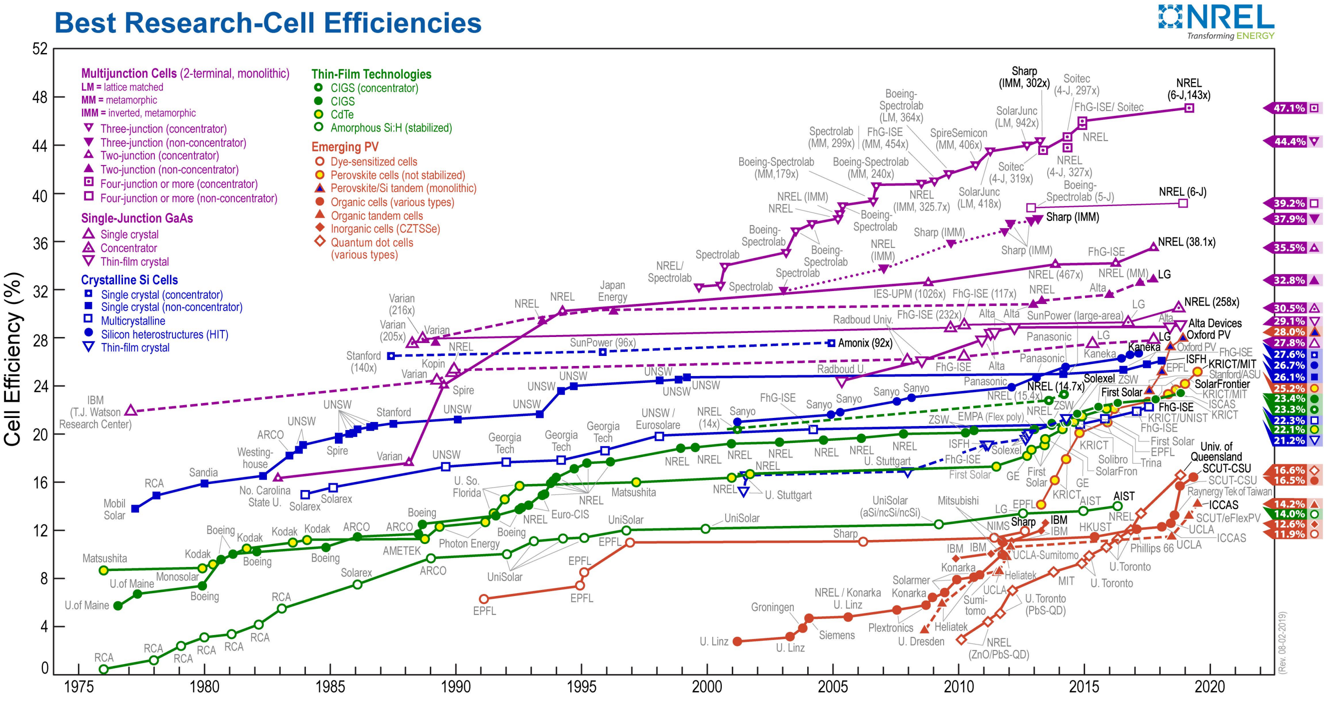

Figure 2.2: NREL solar cells efficiency records over time [11]

2.4 Origin of Perovskite

In the Ural mountains, in 1839, calcium titanate ($CaTiO_3$) was discovered by Gustave Rose. This atomic structure was named perovskite, after the mineralogist Lev Perovski. In 1945, Megaw resolved the perovskite crystal structure [14]. Afterwards, compounds with the same crystal structure could be synthesised. The generalised chemical formula covering several perovskite compounds is ABX_3; where A is a cation, B is a smaller cation, and X is a halide or an oxide. In figure 2.3, the crystal structure of $CaTiO_3$ is represented. The A cation (Ca^+) is represented by the yellow spheres, the B (Ti^{3+}) cation by the white sphere, the X (O^-) by the red spheres:

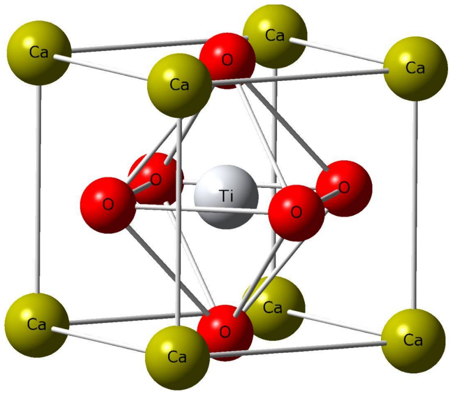

Figure 2.3: Schematised $CaTiO_3$ to illustrate the ABX_3 cubic crystal structure

Perovskite can be divided into alkali halide perovskite (ABX_3) and chalcogenide perovskite (AMO_3). Alkali halide perovskite can be organic or inorganic, depending on the A cation composition. In 1893, $CsPbX_3$ compounds were identified by Wells [15]. Alkali halide perovskite was first studied as $CsPbX_3$ in 1958 [16]. Organic/inorganic lead halide perovskites has favourable excitonic properties, which are useful for LED and FET, and a high absorption coefficient and electrical conductivity, which make it ideal for solar cells applications. The first perovskite solar cell was presented in 2009 by Miyasaka et al., but it had a low efficiency (3.13% for $CH_3NH_3PbBr_3$ as a perovskite layer and 3.81% for $CH_3NH_3PbI_3$ [17]), so it was not immediately considered worthwhile to further investigate. In this cell, $CH_3NH_3PbX_3/TiO_2$ was the photoelectrode and a Pt-coated FTO glass as cathode. Between the two electrodes an organic electrolyte solution of lithium halide and halogen was inserted to create a redox couple. In 2012, organic/inorganic metal halide perovskite began to be considered as a viable option for photovoltaic purposes, when Kim, Gratzel and Park et al. made a solid-state meso-superstructured perovskite cell with an efficiency of 9.7%, in which Spiro-MeOTAD was used as HTL and mesoporous TiO_2 as ETL [18]. The application of a solid state HTL instead of a liquid one considerably increased the efficiency. As of the writing of this paper, the record for a single junction perovskite is 25.2%, as obtained by KRICT and MIT, and 28% for tandem, as obtained by Oxford PV [11].

2.5 Spin coated $CsPbI_2Br$ state-of-the-art

The Shockley Queisser limit for $CsPbI_2Br$ with a bandgap of 1.92 eV is given by a J_{sc} (short circuit current density) of 16.3 mA/cm^2 and a V_{oc} (open circuit voltage) of 1.63 V [19]. In 2016 Sutton et al. made a solar cell using spin coated $CsPbI_2Br$ with a bandgap of 1.92 eV as its photoactive layer, and obtained a J_{sc} of 11.89 mA/cm^2, a V_{oc} of 1.11 V, and a fill factor (FF) of 75%, reaching a maximum efficiency of 7.8% in forward scan, 9.84% in reverse scan, but only 5.6% for stabilised PCE [19]. In 2018 Liu et al. improved the perovskite/ETL interface, and reached 13.3% as their record efficiency [20], and in July of the same year Yan et al. used the same interface to reach an efficiency of 14.6% in reverse bias, a V_{oc} of 1.23 V, an FF of 78.8%, and a J_{sc} of 15.0 mA/cm^2, with a stabilised PCE of 14.1% [21]. As of the writing of this thesis, this is the record PCE reached for spin-coated solar cells with pure $CsPbI_2Br$ as their photoactive layer.

2.6 Perovskite multi-junction solar cells

Multi-junctions consist of multiple solar cells that can be considered to function as diodes connected in series. Each cell absorbs a part of the solar radiation spectrum, allowing for more effective photovoltaic absorption of photons than a single cell could. A potential drawback of this function is the limitation of the maximum short circuit current by the lowest individual cell current in case of asynchronous maximum power points across the different cells, consequently limiting the maximum reachable efficiency. In the case of perovskite multi-junction cells, a tandem solar cell is created by growing a perovskite solar cell, with a bandgap typically between 1.4 eV and 1.7 eV, on top of a mono-crystalline Si solar cell. Furthermore, a triple-junction cell can be produced by growing a high bandgap perovskite cell on a perovskite/c-Si stack. These concepts are further illustrated by figure 2.4. The solar irradiation spectrum relevant for the functioning of these cells is given in figure 2.5.

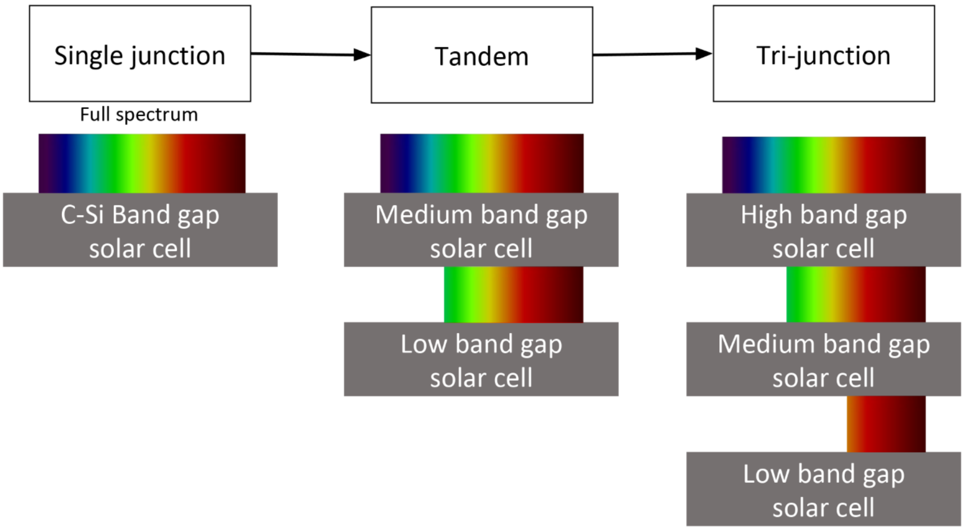

Figure 2.4: Bandgap overlap in multi-junction solar cells

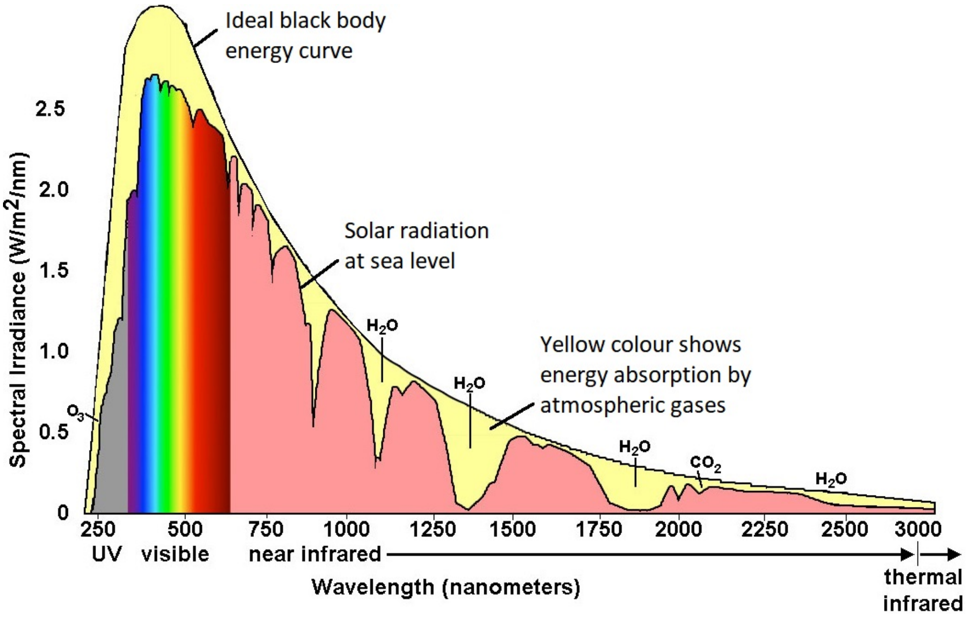

Figure 2.5: Solar irradiation intensity per wavelength in atmosphere [22]

3 Methodology and Materials

3.1 Material properties

This section gives an overview of the material properties that are used to produce the investigated solar cell configurations. The glass/ITO undergoes a plasma oxygen treatment to weaken any polymeric bonds present on the ITO, then the samples are rinsed in a cleaning machine. Lastly, a UV treatment is applied on the ITO surface. The main hole transport layer materials investigated in this thesis are NiO and Spiro-TTB, and a comparison is made between their general behaviour. For the NiO to be sufficiently conductive, an annealing step is necessary after its deposition. For this, the sample is put on a cold hot plate and is subjected to a 15-minute ramp until a stable temperature of 300°C, where it is maintained for another 15 minutes. Finally, the system is cooled down slowly over the course of 15 minutes.

- Substrate: Kintec Glass+ITO
  - Indium-tin-oxide (ITO) is deposited on glass by magnetron sputtering. The ITO sheet resistance is 15 $\Omega/\square$. The optical transmission is higher than 85% at 555 nm. The product configuration is glass, SiO_2 (23 nm) as a buffer, and ITO (125 nm)[23].
- EBL: Sigma Aldrich MoO_3
  - Molybdenum(VI) trioxide(MoO_3) [24]
- HTL (a): Lumtec LT-N138C Spiro-TTB
  - 2,2',7,7'-Tetra(N,N-di-p-tolyl)amino-9,9-spirobifluorene (Spiro-TTB, $C_{81}H_{68}N_4$) has a purity grade of 98% [25, 26].
- HTL (b): CSEM NiO
  - Nickel oxide (NiO) is deposited through sputtering using a Oerlikon Clusterline at CSEM in Neuchâtel [27].
- HTL (c): Lumtec LT-N1002 BF-DPB
  - N4,N4'-Bis(9,9-dimethyl-9H-fluoren-2-yl)-N4,N4'-diphenylbiphenyl-4,4'-diamine (BF-DPB)is sublimed, with a grade of $> 99\%$ [25]
- HTL (d): Lumtec LT-S922 Spiro-MeOTAD [25]
  - Grade of $> 99.5\%$ [25]
- Photoactive layer: Co-evaporated perovskite
  - Sigma aldrich 203017-10G Ceasium bromide (CsBr) comes in the form of beads, with purity 99.999% [28].
  - Alpha aesar MDL:MFCD00011163 Lead(II)iodide (PbI_2) powder, purity 99.9985%, melting point 402°C, and the boiling point is 954°C [29].

- ETL: Nano-C RC190412 C_{60}
  - Fullerene (C_{60}) is a black powder, with a purity over 99.95% [30].
- HBL: Lumtec TmPyPb
  - 1,3,5-Tri[(3-pyridyl)-phen-3-yl]benzene (TmPyPb, $C_{39}H_{27}N_3$) is a white powder, with a purity over 99.5% [25].

3.2 Cell configurations

Since the cell thickness is typically less than one micrometer, it is grown on a glass substrate to ensure structural integrity. The first layer is a thin indium oxide (ITO) contact layer, that is sputtered on the glass substrate. The next layer has the functionality to help holes extraction and is hence named the hole transport layer (HTL), which is thermally evaporated onto the contact layer. The third layer is the photoconductive layer, perovskite ($CsPbI_2Br$), in which hole-electron couples are created and conducted towards the HTL and the electron transport layer (ETL) respectively. It is thermally co-evaporated, with a rate of 0.39 Å/s with a tooling factor of 21.0 for CsBr and a rate of 0.6 Å/s with a tooling factor of 21.39 for PbI_2, and an operating pressure of $1.3 \cdot 10^{-6}$ Torr. The fourth layer is then the ETL, thermally evaporated fullerene (C_{60}) onto the perovskite, in order to enable the extraction of electrons. The fifth layer is a hole blocking layer, TmPyPb, that favors electron extraction by acting as a barrier for the holes. The last layer is the positive contact, silver (Ag), which is thermally evaporated on the TmPyPb layer. In summary, the base solar cell treated in this thesis is illustrated figure 3.1, where its bandgaps align as schematised in figure 3.2:

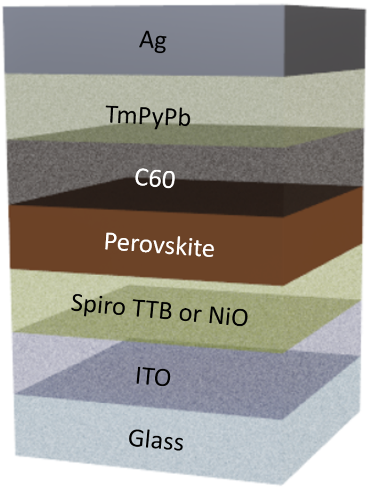

Figure 3.1:
Schematic of the investigated solar cell configurations

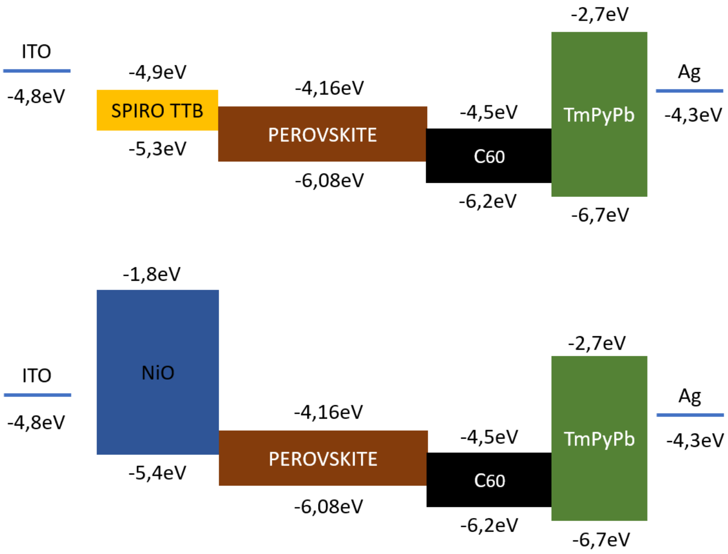

Figure 3.2:
Band alignments compared to perovskite of the investigated configurations [23, 21, 31, 32, 33, 34, 35]

3.3 Manufacturing process

The perovskite layer can be deposited on a substrate through different approaches. State-of-art perovskite layers are obtained through spin coating, with either the one-step, the two-step, or the hybrid solution method. However, in this thesis the applicability of thermal vapour deposition is investigated.

3.3.1 Thermal vapour deposition

Thermal vapour deposition allows for the growth conditions of the material on the substrate to be controlled effectively. The material is put in a crucible for evaporation at a certain temperature and pressure. If the material is solid, it is sublimated, the vapour expands in the chamber and it condenses on the unheated substrate. The sublimation of the material is possible if the chamber pressure is below the triple point pressure [30]. This concept is further portrayed by figure 3.3:

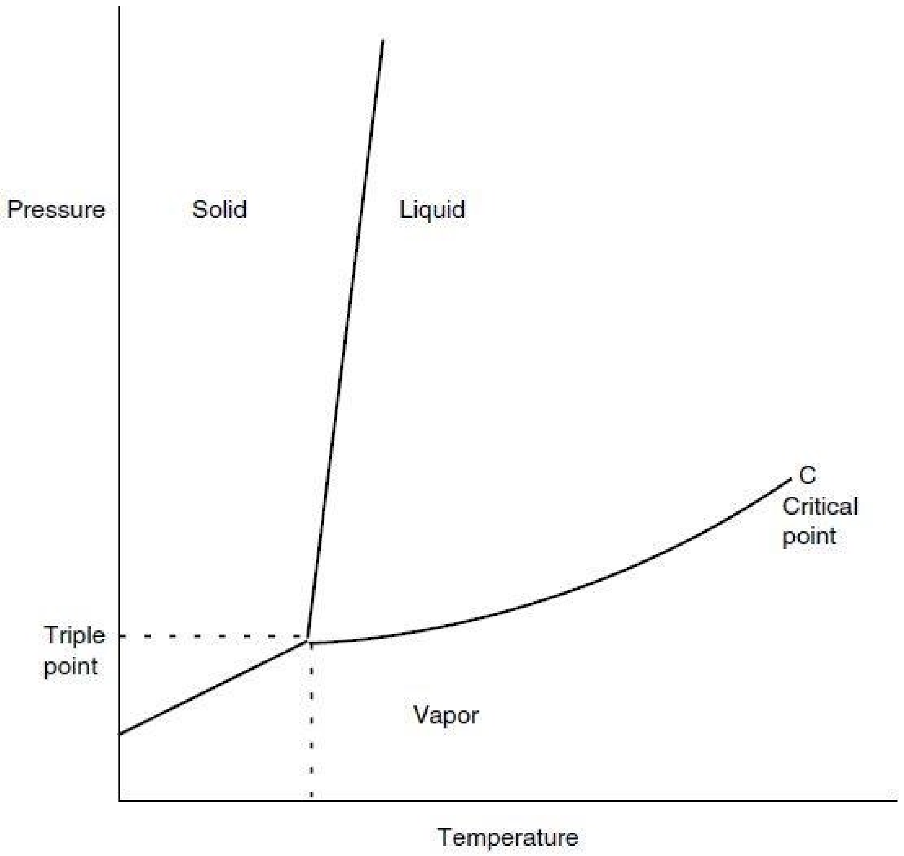

Figure 3.3: Phase diagram showing the triple point for a one-component system [36]

When heating a material to the point where inter-molecular bonds on its surface are broken by the transferred thermal energy, a transition to the vapour phase occurs. Since the vapour pressure depends exponentially on the temperature, the crucible temperature should be closely monitored in order to maintain a constant evaporation rate. Furthermore, perovskite vapour deposition (PVD) requires a vacuum set up, which is achieved by evacuating inert gas from the deposition chamber. The deposition then happens at a low working pressure (for perovskite precursors $1.5 \cdot 10^{-6}$ Torr or lower). Evaporation is a viable manufacturing technique for many different layers, organic and inorganic alike. Overall, the material that is to be deposited is placed in a crucible topped with a shutter to aid precise timing control. The thickness of the deposited layer is determined through quartz crystal micro-balance sensors and tooling factors. The tooling factor represents the ratio between the material deposited on the sensor and the material deposited on the substrate. The material deposited on the substrate is different from the material deposited on the crystal, since the sensor cannot be positioned at the same location as the substrates because of shadowing issues. In general, thermal vapour deposition is characterised by minimal surface damage, as the samples are placed upside down to provide increased control over the growth conditions and reduce the probability of particulate contamination.

For large organic molecules like the organic perovskite precursor, it can be difficult to accurately determine the evaporation rate, or to establish the layer growth rate using thermal co-evaporation. This is because organic materials like MAI and FAI have low molecular mass and high vapour pressure. This combination leads to an increased vacuum pressure and a more widespread evaporation, as opposed to the preferred directionality, in addition to a low sticking coefficient to crystal quartz monitors. Therefore, it can be hard to determine the layer thickness through the quartz micro balance system. Examples of this issue are given by different authors such as: Malinkiewicz et al, Borchert et al., Zhao et al; all of whom had difficulties accurately measuring the MAI deposition rate [37, 38, 39]. However, in contrast to the issues of organic perovskite, inorganic perovskite presents a superior thermal stability and does not exhibit significant non-directional evaporation.

3.3.2 Perovskite thermal co-evaporation

An inorganic perovskite layer can be grown on a substrate by thermal co-evaporation. Through the simultaneous evaporation of CsBr and PbI_2, a $CsPbI_2Br$ layer is formed. This process is especially advantageous for this compound because of the following properties:

- It is reproducible;
- It allows for precise composition ratio determination;
- It enables the production of a homogeneous layer;
- It allows for (up-)scaling of active cell area;
- It negates the need for annealing;
- The necessary facilities for it are readily available in the industry.

The set of figures below illustrates the mentioned concepts. Figure 3.4 portrays the simplicity of a shutter screening the substrate from the evaporated substance, figure 3.5 portrays a single directional evaporation, and figure 3.6 illustrates the discussed co-evaporation. For these figures, it is important to note that the substrate holder continuously rotates during the process to ensure a uniform deposition. In this thesis, the co-evaporation of perovskite is done using an evaporator system of the Kurt J. Lesker company.

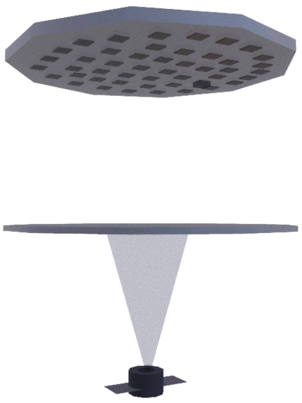

Figure 3.4:
Screened evaporator

Figure 3.5:
Single-source evaporation

Figure 3.6:
Co-evaporation

After deposition of the perovskite layer, the sample can optionally be put on a pre-heated hot plate for an annealing step. The hot plate is kept inside the glove box. For this thesis, the annealing temperatures are 80°C and 100°C.

3.4 Methods of analysis

3.4.1 Current density-voltage measurements

The sunlight-to-electricity conversion of a solar cell can be evaluated through the power conversion efficiency (PCE), determined by means of current density-voltage (J-V) measurements. A range of voltages is applied to the solar cell under AM 1.5G illumination conditions. The sunlight radiation is mimicked with a Xenon and a Halogen lamp. The solar cell holder is positioned perpendicularly to these lamps in order to obtain the maximum radiant illumination. A 4-point probe is used to measure the photovoltaic response of the illuminated cell, in order to minimise contact resistance issues. The holder consists of two pins at the cathode of the cell and two pins at the anode, one pin for supplying an input voltage and one for collecting the current. The anode pin is responsible for the voltage ground state. The main parameters of the resulting circuit that can be analysed are:

- Short circuit current J_{sc} - The generated current when the applied bias is equal to zero.
- Open circuit voltage V_{oc} - The voltage when the input current is equal to the output current, so the net current is zero.
- Maximum power point P_{mpp} - The point on a current-voltage curve that has the highest $I \cdot V$ product, i.e. the highest power output.

- Voltage and current density at the maximum power point $\mathrm{V_{mpp}}$ and $\mathrm{J_{mpp}}$ - The voltage and current density determined at the maximum power point.
- Fill factor FF - The ratio between the product of the $\mathrm{V_{mpp}}$ and $\mathrm{J_{mpp}}$ and the product of the $\mathrm{V_{oc}}$ and the $\mathrm{J_{sc}}$.

With these parameters, the output power conversion efficiency can simply be calculated through equation 3.1 [40]:

$$\mathrm{PCE} = \frac{P_{\mathrm{out}}}{P_{\mathrm{in}}} = \frac{J_{\mathrm{sc}} \cdot V_{\mathrm{oc}} \cdot \mathrm{FF}}{P_{\mathrm{in}}} \tag{3.1}$$

This power conversion efficiency is dependent on the inner resistance of the cell. A solar cell can be analytically modelled as a diode, having a resistance in series and a resistance in parallel (shunt resistance). The electrical circuit that results from this model is visually depicted in figure 3.7.

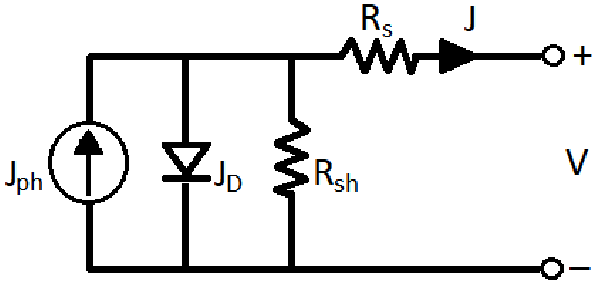

Figure 3.7: Analytically modelled solar cell as a diode-resistance circuit

For computation of the current density as a function of the net voltage, equation 3.2 applies [41]:

$$J(V) = J_{\mathrm{ph}} - J_0 \left[\exp\left(\frac{e\,(V + JR_{\mathrm{s}})}{nk_{\mathrm{B}}T} \right) - 1 \right] - \frac{V + JR_{\mathrm{s}}}{R_{\mathrm{sh}}} \tag{3.2}$$

Where $\mathrm{J_{ph}}$ is the photo-generated current density, $\mathrm{J_0}$ is the reverse saturation current density, $\mathrm{R_s}$ is the specific series resistance (sheet resistance), $\mathrm{k_B}$ is the Boltzmann constant, and $\mathrm{R_{sh}}$ is the specific shunt resistance. Shunt resistance indicates the presence of a shunt, which is an alternate path for the current, decreasing the available solar cell voltage. Both series and shunt resistances reduce the fill factor. High values of series resistance will additionally negatively impact the short-circuit current.

The J-V graph is obtained by plotting two curves of the current density J as a function of the applied voltage V. One curve represents the forward scan (increase from 0 V to 1.2 V) and the other the reverse scan (decrease from 1.2 V to 0 V). In perovskite solar cells, the forward and reverse scans do not precisely coincide, which is known as hysteresis.

For short integration times, this effect can also cause a deformation in the curve, like an initial “bump” for the reverse scan. This phenomenon can be attributed to a charge accumulation at the interfaces of a perovskite layer, caused by the presence and migration of mobile ions in the material [42, 43]. The algorithm used to determine the PCE during maximum power point tracking is based on a three point weight comparison method [41].

3.4.2 Scanning electron microscopy

Scanning electron microscopy (SEM) images the surface of a sample using a beam of electrons accelerated by an applied voltage. Figure 3.8 schematically represents the ray path of such a beam in a SEM setup. These electrons are scattered back by the sample material, and the resulting back-scattered electrons, secondary electrons and X-rays can be detected to image the material. Secondary electrons are emitted after a surface impact by the electron beam, and the removal of inner-shell electrons causes the emission of X-rays. Back-scattered electrons (BSE) are elastically scattered and they have a higher average energy than secondary electrons (SE), because they originate from deeper inside the material. The electrons are collected by a BSE+SE detector and their energy difference enables the imaging process. The resolution can be scaled down to 1 nm. The specimen has to be smaller than its holder, grounded, and it has to be conductive or covered with a conductive nanometric layer, to avoid charge accumulation. A non-conductive specimen like perovskite is commonly grounded using copper tape to aid the discharge of accumulated charge through the holder. The specimen is inserted for analysis into a vacuum chamber through a loading chamber, to avoid breaking the vacuum of the main chamber. The vacuum enables the correct functioning of the SEM, by avoiding scattering due to the presence of undesired particles in the chamber. The SEM analysis in this thesis was conducted with electrons accelerated by a potential of 5 KeV and a probe current of 7 mA in a JEOL scanning electron microscope.

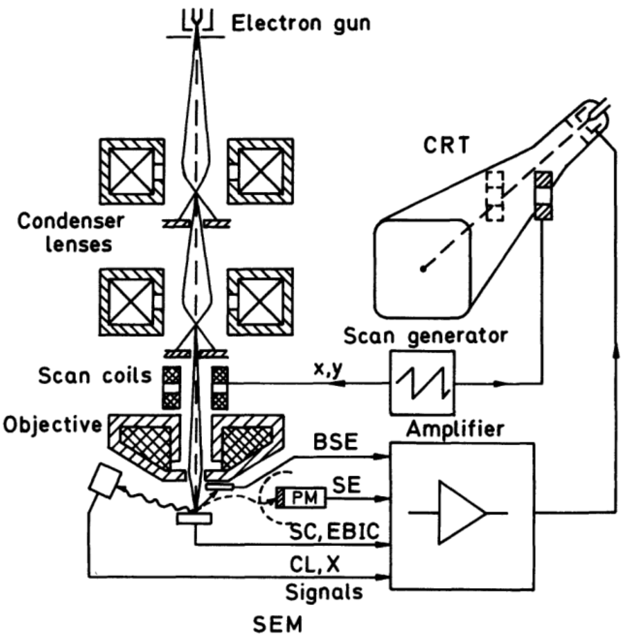

Figure 3.8: Schematised ray path for a scanning electron microscope [44]

3.4.3 X-ray diffraction

X-ray diffraction (XRD) is an analysis technique for the crystallography of a material. This crystalline material acts as a 3D diffraction grating for wavelengths of the size of crystal planes, as satisfied by the X-rays. In the sample holder, the material is subjected to a collimated, monochromatic radiation generated by a cathode ray tube. The diffraction is considered constructive when Bragg's law, $n\lambda = 2d \sin\theta$, is satisfied, and destructive when it is not [45]. In Bragg's law, λ refers to the X-ray wavelength, d to the crystal plane spacing, and θ to the angle of incidence of the X-ray. Bragg's law is illustrated by figure 3.9. The X-rays that are diffracted by the sample are collected by an X-ray detector and categorised. The employed XRD machine for this thesis is an Oxford diffraction machine, Rigaku, and the targets are copper and molybdenum.

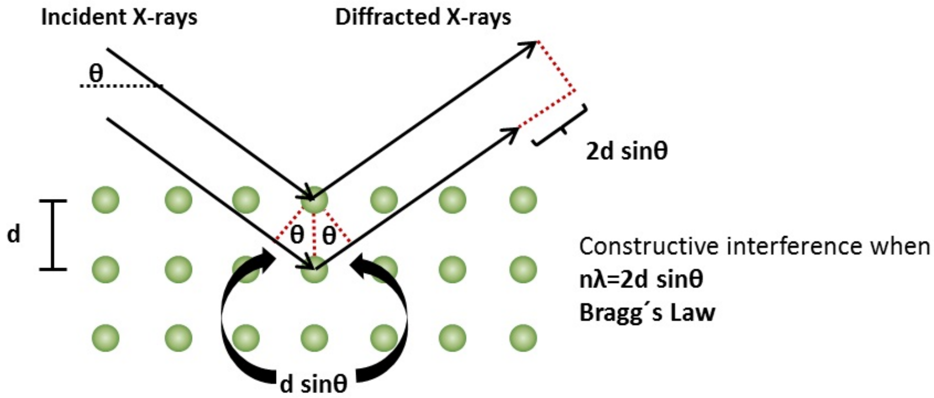

Figure 3.9: Schematised representation of the functioning of X-ray diffraction through Bragg's law [45]

3.4.4 Transmission electron microscopy

Transmission electron microscopy (TEM) is a method able to provide morphological, crystallographic and chemical analysis. In transmission electron microscopy an electron gun emits electrons, which pass through condenser lenses to tune the illumination aperture and area. Then, a system of lenses enables the imaging procedure by controlling the electron intensity distribution behind the specimen. An electron can be elastically scattered by nuclei with a negligible loss of energy, or diffracted according to Bragg's law. In the latter case, they can be considered as a Bloch wave field with the lattice periodicity of the specimen, or in-elastically scattered by an interaction with another electron. Two microscopy methods are distinguished: the bright field (BF) or the dark field (DF) imaging. In the first, the objective aperture selects the transmitted electrons. The contrast is given by crystalline or high mass materials. In dark field imaging, only the scattered electrons are analysed, the transmitted electrons are not considered. The areas with absence of scattered electrons will appear dark. In both methods, electrons are collected by an energy loss spectrometer. X-rays are produced by an interaction of electrons with the specimen. The energy-dispersive X-ray spectroscopy is used in combination with TEM BF and HAADF (high-angle annular dark field imaging) to assess the chemical composition of the samples in relation to their nano-structure. Lamellae from solar cells are prepared for TEM using the focused ion beam (FIB) lift-out method. Since the electrons are to be transmitted through the sample, its thickness can generally not overpass 300 nm.

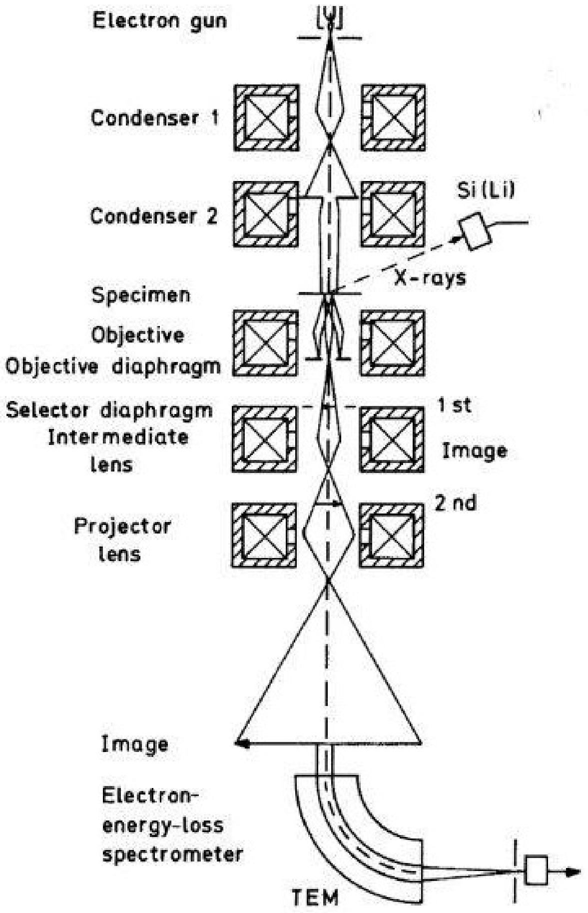

Figure 3.10: Schematised representation of a transmission electron microscope [44]

3.4.5 External quantum efficiency

The external quantum efficiency (EQE) is the number of generated electrons in the external circuit by all the incident photons at an established wavelength. The EQE can be measured and graphed by plotting the number of photons that generate electrons against the spectrum of wavelengths for which it is measured, and then normalising it to obtain a probability range. A light beam is generated by a xenon lamp, and split through a grating into radiation waves with different wavelengths. After isolating each wavelength through a monochromator, a chopper is applied to alternately put these in on/off states. Then, the respective wavelength collimated towards the active area of the solar cell and the produced current is collected and compared to a reference value. The exposed area of the cell to the beam is equal to 1 mm^2. During this process, it is important to maintain a constant optical path to avoid inconsistencies. The EQE is finally computed with equation 3.3a, where the spectral response SR is determined by equation 3.3b [46]:

$$\mathrm{EQE} = \frac{n_{\text{electrons}}}{n_{\text{photons}}} = \frac{\frac{J_{\mathrm{SC}}}{q}}{\frac{E_{\text{photo}}}{h \cdot v}} = \mathrm{SR} \cdot \frac{h \cdot c}{q \cdot \lambda} \tag{3.3a}$$

$$\mathrm{SR} = \frac{\mathrm{J}_{\mathrm{SC}}(\lambda)}{\mathrm{E}_{\mathrm{AM1.5g}}(\lambda)} \tag{3.3b}$$

The spectral response of the cell under test is compared to that of a reference cell and a monitor cell, in order to keep a baseline and avoid errors. A schematic visualisation of the setup used to determine the EQE is given in figure 3.11. In equational form, the Device Under Test (DUT) spectral response is calculated through equation 3.4:

$$\mathrm{SR}_{\mathrm{DUT}} = \overbrace{\underbrace{\mathrm{SR}_{\mathrm{ref}}}_{\substack{\text{certified measurement}\\ \text{stored in LabView code}}} \cdot \underbrace{\frac{\mathrm{I}_{\mathrm{SC,monitor}}(\lambda)}{\mathrm{I}_{\mathrm{SC,ref}}(\lambda)}}_{\substack{\text{taken during}\\ \text{calibration measurement}}}}^{\text{stored in calibration file after calibration}} \cdot \underbrace{\frac{\mathrm{I}_{\mathrm{SC,DUT}}(\lambda)}{\mathrm{I}_{\mathrm{SC,monitor}}(\lambda)}}_{\substack{\text{taken during}\\ \text{measurement of DUT}}} \tag{3.4}$$

At short wavelengths, the EQE is mainly limited by frontal surface recombination, and at long wavelengths it is mainly limited by rear surface recombination. An overall QE reduction is caused by a reflection of the EQE beam on the glass substrate, and parasitic absorption. Furthermore, this reflection limits the diffusion of the beam. Additionally, the EQE measurement is used to determine the short circuit current density of a solar cell.

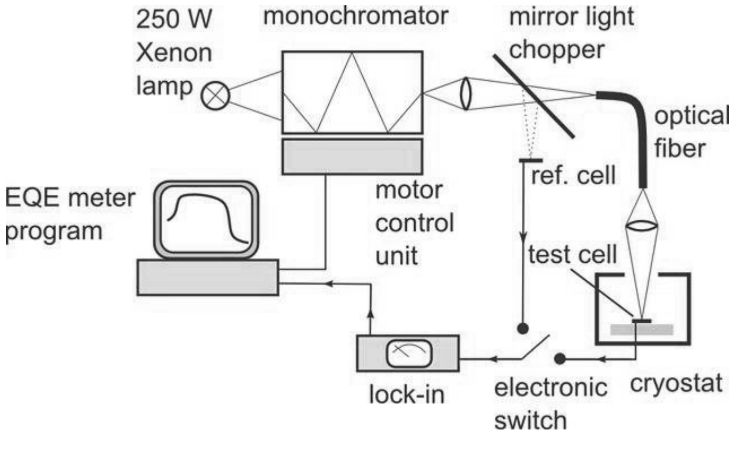

Figure 3.11: External quantum efficiency measurement scheme [47]

3.4.6 Photoluminescence spectroscopy

Photoluminescence spectroscopy is used to contactlessly study the electronic and optical properties of a material. The emission of light is a consequence of the phonon-electron interaction. When photons are absorbed by a material, the resulting light emission is called photoluminescence. After absorbing a photon, an electron is promoted to a higher energy level, resulting in an additional electron in the conduction band and the hole that it leaves in the valence band, with a finite k-moment; an electron-hole recombination is then responsible for the light emission process. The photoluminescent properties of $CsPbI_2Br$ is investigated through a fixed-wavelength, diode-pumped solid-state laser (Cobolt Fandango), operating at a wavelength of 514 nm [48]. The laser head collimates and emits a laser beam through a manual shutter. The emitted beam power is long-term stable due to an optical feedback loop. The instrumentation configuration is summed up as follows:

- PL instrumentation: Monovista CRS+ (Spectroscopy and Imaging GmbH)
- Grating groove density: 300 grooves/nm
- Objective: Olympus LC Plan IR objectives for imaging
- Magnification: 50x
- Numerical aperture: 0.65
- Working distance: 4.5mm
- Spectroscopy camera: InGaAs CCD fully integrated camera, cooled at -70 °C

The measurements were performed under various illumination power conditions, obtained by attenuating the power of the beam with regard to its spot size and power density. This results in a laser power density of 6 mW/cm^2 and a spot size diameter of 50-65 µm, taking into account it has a Gaussian distribution shape.

As the bandgap energy corresponds to the energy of the emitted photons consequential to the passage from valence band to conduction band, it can be determined by inducing that passage and measuring the expelled energy with PL spectroscopy. Furthermore, defects in the material induce defect levels in the bandgap, and can be detected through PL spectroscopy because they exhibit specific radiative transitions. Consequently, two peaks may appear on the resulting PL graph, which implies recombination due to a variety of energy states. Lastly,the evolution of the PL peak positions may provide insights into phase segregation.

3.4.7 Absorbance and Absorptance

The Spectro UV-VIS-NIR is employed to indirectly determine the absorbance of a material by measuring its transmittance and reflectance, using the relationship given in equation 3.5. The absorbance is mainly important for determining to what extent a layer absorbs photons in the desired wavelengths, which is necessary for the generation of electricity by the photoactive layer.

$$\%\text{Absorbance} = 100\% - \%\text{Reflectance} - \%\text{Transmittance} \tag{3.5}$$

The specific instrument used for this thesis, the Perkin Elmer UV/VIS/NIR lambda 950, consists of the following [49]: Light sources: A halogen gas in the bulb of a tungsten lamp is used to produce a spectrum in the VIS/NIR region (300-3500 nm), and a deuterium gas in the bulb of the tungsten lamp supplies the UV region (175-400 nm). Two monochromators select the same wavelength, to make the cutoff level lower ($10^{-3} \cdot 10^{-3} = 10^{-6}$). Two detectors, one is an Si-based PMT with a spectral response from 150 nm to 900 nm, the other is a cooled InGaAs photodiode with a SR from 800 nm to 2500 nm. An integrating sphere, used to integrate the light distribution of hazy samples in the space.

The absorptance is measured by photothermal deflection spectroscopy (PDS), as this method is able to measure small values of absorptance directly. This technique is based on local heating of a sample under certain sub-gap wavelength light exposure. This light is absorbed and converted into heat by non-radiative recombination, generating a periodic temperature fluctuation that causes periodic changes in the refractive index of the sample. These changes are then detected from the surrounding environment with a HeNe laser directed parallel to the sample surface. The magnitude of the deflection is finally measured with a position sensitive detector and a lock-in amplifier, through which the absorptance of the sample can be accurately determined. For this thesis, the PDS measurement of the samples is conducted in a basin of Fluorinert, characterised by a large $\delta n/\delta T$.

4 Characterisation Results

4.1 Phase transition and efficiency

Solar cells can be exposed to various operational conditions, mainly depending on the location where they are installed and on the period of the year. The exterior temperature can roughly vary from -20°C to 45°C, and solar radiation further heats the device. Additionally, it is important to consider the physical and chemical stability of the solar cell, in order to develop a product that does not deteriorate rapidly under operational conditions. Poglitsch was the first to notice that the chemical structures of $CH_3NH_3PbBr_3$, $CH_3NH_3PbI_3$ and $CH_3NH_3PbCl_3$ were dependent on the temperature [50]. These three compounds have varying colours in accordance to their various bandgaps. Poglitsch noted that a change of solution temperature implies a change of the colour for each compound. For example, $CH_3NH_3PbI_3$ becomes transparent below 40°C although it is initially black. Perovskite for solar cells is mainly considered in three different crystal structures: cubic, orthorhombic and tetragonal. The cubic phase is also categorised by an α-phase and is the most photoactive; the tetragonal phase is less photoactive and is considered a δ-phase; the orthorhombic phase is considered non photoactive and is also a δ-phase. Another typical of perovskite lattice is the trigonal one, but it does not appear in the PV temperature range. The transition from α-phase to δ-phase consists of in a change of the crystal structure.

For estimating the crystal structure of a perovskite layer, the octahedral factor and the Goldschmidt tolerance factor are used. These factors and their practical use were described in detail by Li et al. in 2008 and Kronmüller et al. in 2007 [51, 52]. For halide perovskite the octahedral factor, $\mu = R_B/R_X$, exists in the range $0.44 < \mu < 0.90$, and the tolerance factor, $t = (R_A + R_X) / \left(\sqrt{2} \cdot R_B \cdot R_X\right)$, assumes a value between $0.81 < t < 1.11$ [22][49]. Considering the perovskite structure ABX_3, each parameter RA, RB and RX in the above quoted formulas refers to the respective ion radii of A, B, and X. The crystal structure is trigonal or orthorhombic if $t < 0.9$, cubic it $0.9 < t < 1.0$, and tetragonal if $t > 1.0$. In the cubic ABX_3 perovskite structure (a = 3.905 Å, space group Pm-3m, Z = 1), the A atoms are in Wyckoff position 1b, 1/2,1/2,1/2; the B atoms in 1a, 0,0,0; and the X atoms in 3d 1/2,0,0; 0,1/2,0; 0,0,1/2, all being special positions [51]. This structure is visually depicted in figure 4.1.

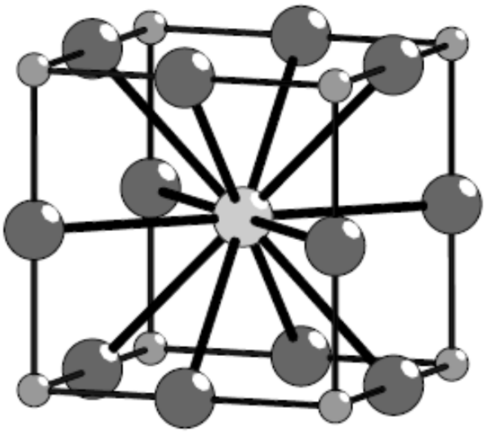

Figure 4.1: Generalised α-phase of ABX_3 perovskite structural model [51]

The hygroscopic nature of the perovskite and the temperature are responsible for the phase transition phenomenon, that highly influences the electrical properties of the perovskite. Furthermore, high temperatures can temporarily stabilise the α-phase or can turn a δ-phase into an α-phase. However, as $CsPbI_2Br$ has a high thermal stability, humidity is mainly responsible for the instability of the α-phase. The phase change rate sharply increases under high relative humidity. Figure 4.2 further illustrates the phase transition, under influence of certain temperatures, and the crystal structures adopted by the perovskite in the different phases.

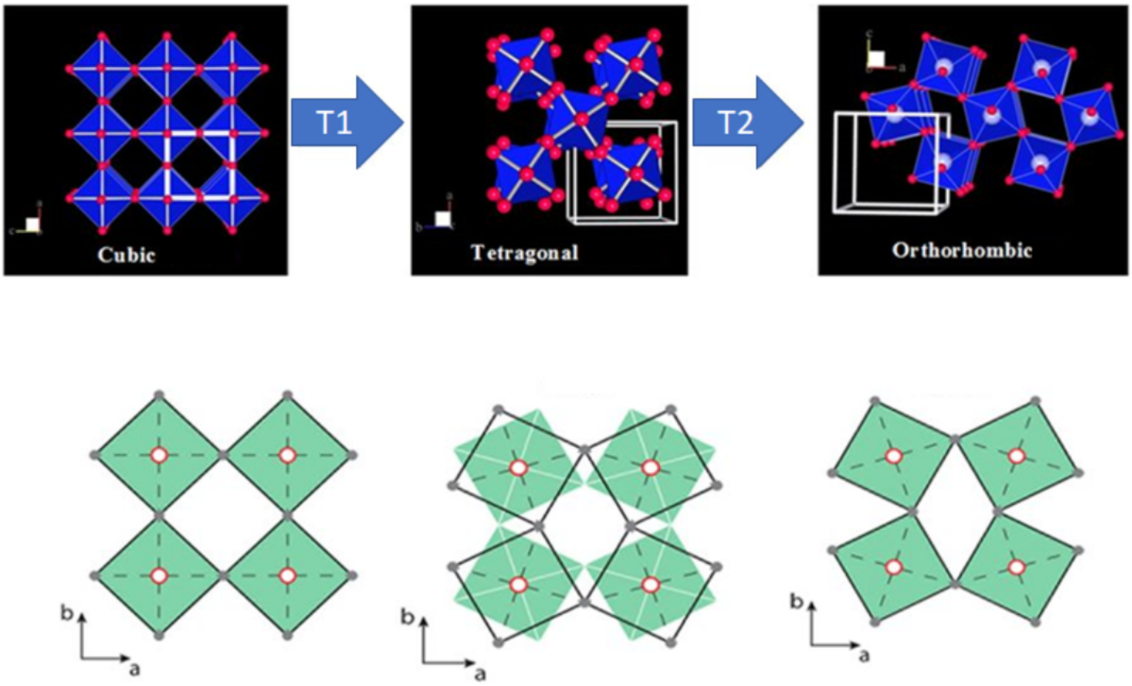

Figure 4.2: Crystal structures and distortions adopted by perovskite during phase transition under influence of temperature and humidity [53]

Besides the effect on an atomic level, the phase change is macroscopically visible because a color change in the perovskite layer is apparent by virtue of the changing bandgap. In the $CsPbI_2Br$, it turns from opaque brown to transparent because of this effect.

Phase transition from the cubic to the orthorhombic phase decreases the cell efficiency and lifespan. The J-V, P_{mpp}, V_{oc}, V_{mpp} and FF graphs that are discussed in this chapter aid the analysis of the perovskite layer, but are determined using a complete cell structure as introduced in section 3.2, figure 3.1, using only the Spiro-TTB variant, with a perovskite thickness of 200 nm, and an active area of 1.04 cm^2.

4.1.1 Efficiency decrease due to phase transition

The phase transition effect is visually apparent from figure 4.3. Here, the stabilised solar cell power exhibits a decrease of more than 10 mW/cm^2 in 3 hours of air-exposure, which is a 17% relative decrease. A change is visible in the J-V curve in figure 4.4; the degradation incurs a rise in series resistance, generating an s-shape in the J-V curve.

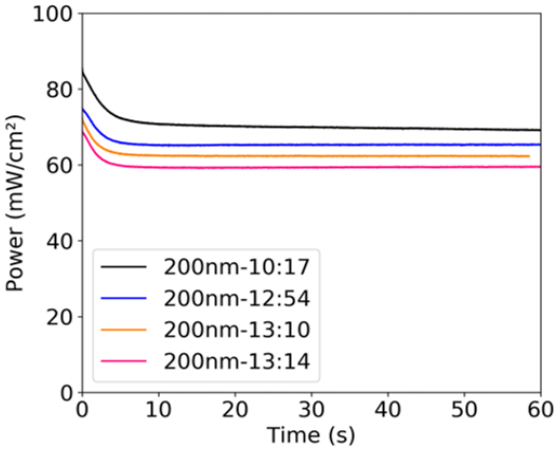

Figure 4.3:
P_{mpp} curve over time from first air exposure to 3 hours of exposure

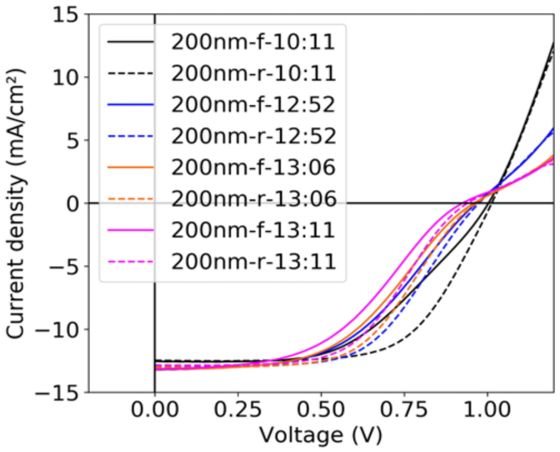

Figure 4.4:
J-V curves from first air exposure to 3 hours of exposure (f and r stand respectively for forward scan and reverse scan

The degradation of the interfaces and the change in the crystal structure of the perovskite are most evident in the behaviour of the FF and the V_{oc}, which are consequently reflected in the V_{mpp}. All of these values exhibit a decrease over time, as can be seen plotted in figure 4.5.

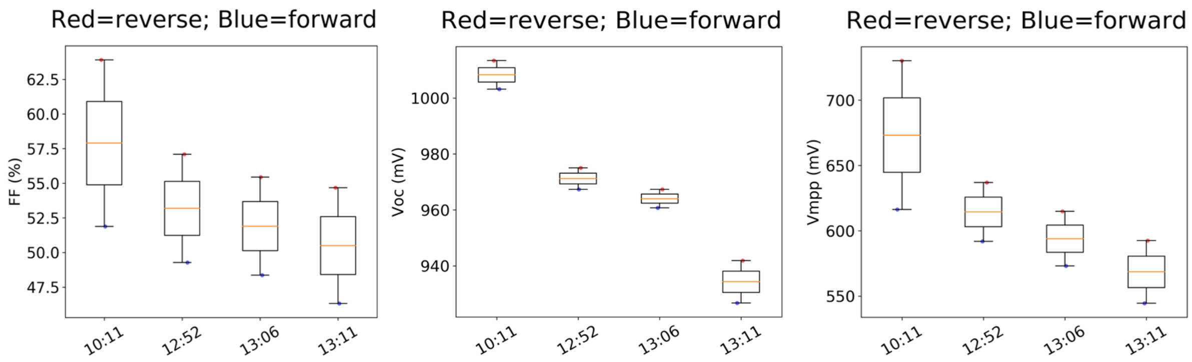

Figure 4.5: FF, V_{oc} and V_{mpp} values plotted at different points in time of a Spiro-TTB HTL cell

4.1.2 Macroscopic aspects of phase transition

To macroscopically investigate the influence of the thickness of the perovskite layer on the phase transition rate, a range of different layer thicknesses were evaporated on a substrate composed of glass, ITO and an HTL (NiO). For this experiment, it is important to take into account that the surface of an individual perovskite layer deposited on a substrate is significantly more influenced by humid conditions than a layer in a completed cell, because in the cell the perovskite is protected from the exterior conditions by layers placed on top of it. The results are visualised in figure 4.8. The thinnest analysed layer of 165 nm exhibits the quickest degradation, indicated in figure 4.8 by the red circle, and showed in a zoomed image in figure 4.7. The phase transition was already evident after two days of exposure to air. The degradation of a sample after long-term air-exposure is visually portrayed in Appendix A1, figure A1.1.

For thicknesses above 185 nm the phase transition is slower, and the perovskite layer was not visibly degraded after two days for these cases[i].

---

[i] In the image of the perovskite thickness of 250 nm the cell is scratched, but this was due to manipulation during measurement, the layer does not exhibit phase transition.

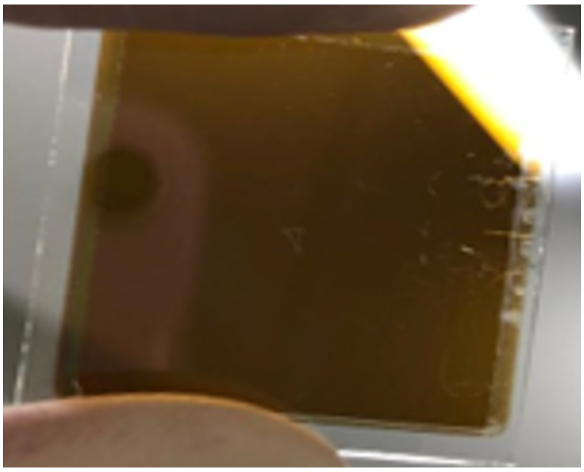

Figure 4.6:
A 165 nm perovskite sample just after initial air-exposure

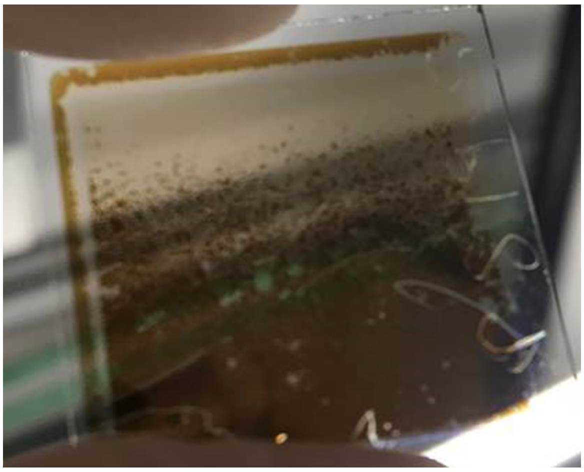

Figure 4.7:
A 165 nm perovskite sample after 2 days of air-exposure

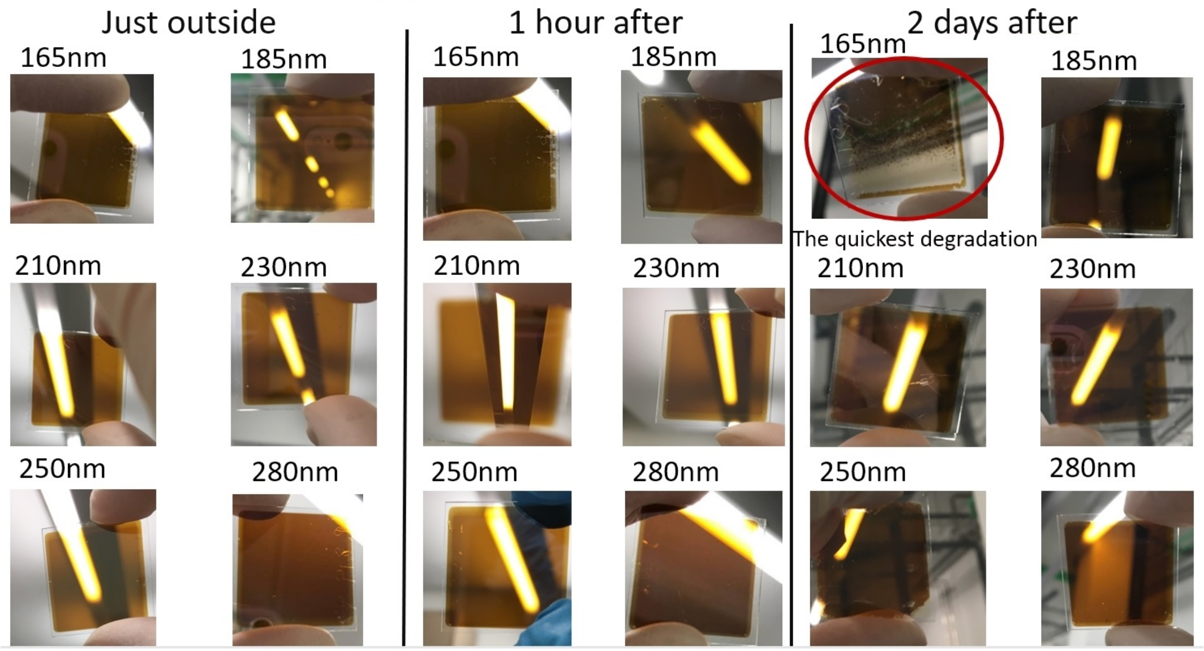

Figure 4.8: Macroscopic perovskite layer degradation for different thicknesses

4.2 Characterisation of the perovskite layer

4.2.1 SEM surface characterisation

SEM was used to analyse perovskite layers with different thicknesses (165 nm, 185 nm, 210 nm, 230 nm, 250 nm) deposited on NiO, the obtained images are shown in figure 4.9 are magnified by a factor of 40k. This illustrates that the crystal size is only a few tens nanometers, almost at the resolution limit of the microscope. Furthermore, the grains are relatively small because they crystallise in the evaporation phase instead of during high temperature annealing. The morphology is compact, flat and there is no evident presence of pinholes.

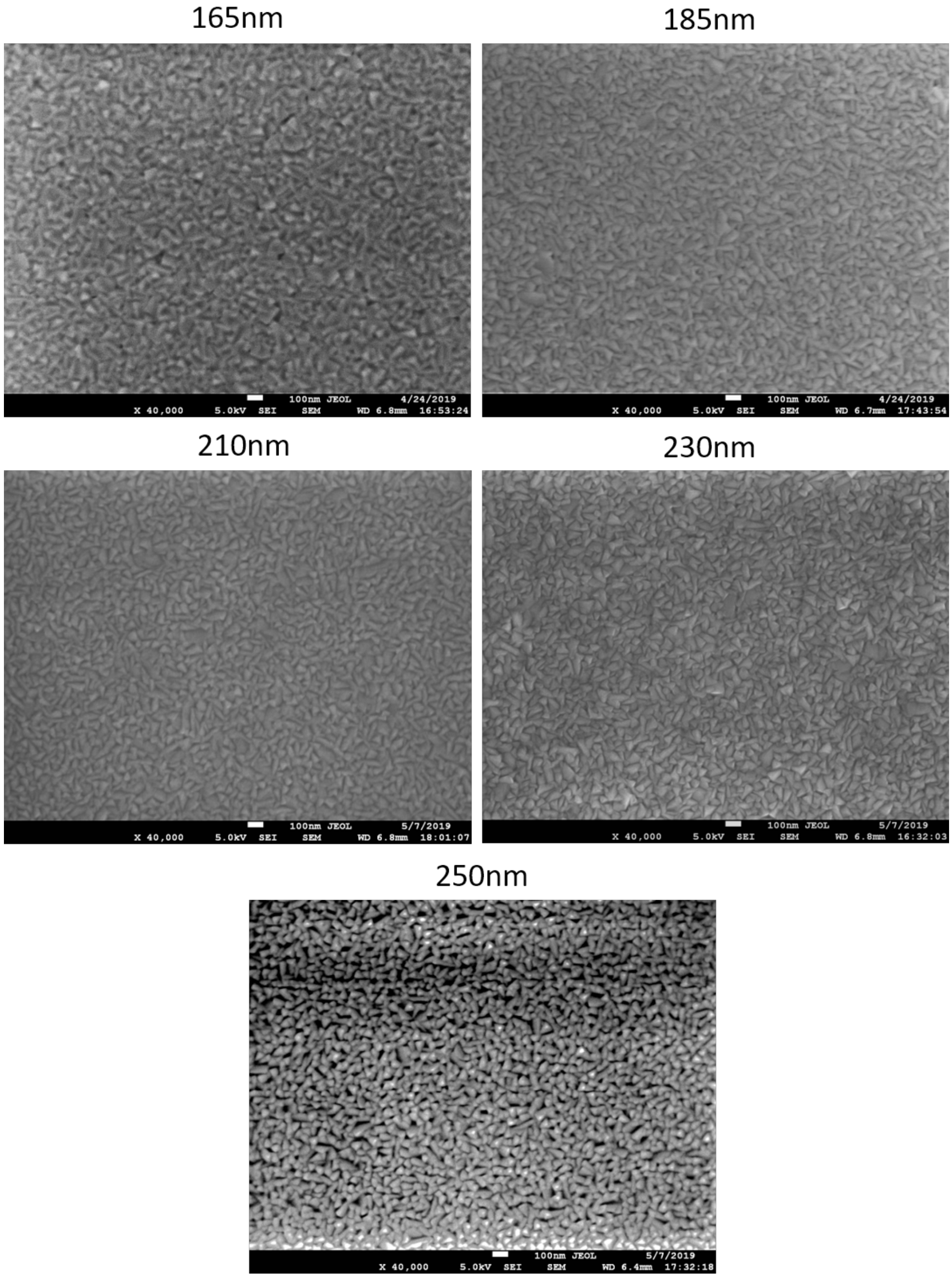

Figure 4.9: SEM top view of perovskite layers with different thicknesses

The five different layer thicknesses exhibit a similar grain size, suggesting a possible absence of strain in the lattice due to a varying thickness. This phenomenon will be further discussed in section 4.2.2.

4.2.2 XRD perovskite crystal structure analysis

An XRD analysis of a sample made of only glass, ITO and perovskite ($CsPbI_2Br$) was performed to determine the crystal structure of a bare perovskite layer. The perovskite XRD peaks should show the presence of characteristic alpha phase peaks at 14.6°, 20.8°, and 29.6°. These correspond to the (100), (110) and (200) plans of the α-phase of $CsPbI_2Br$ [54]. As seen in figure 4.10, the peaks of the $CsPbI_2Br$ under test are slightly shifted towards lower angles. A δ-phase peak is present at 10°. This suggests that the structure is not perfectly cubic and the perovskite obtained through the deposition crystallises in a γ-phase [55]. This will be further analysed through a TEM analysis in section 4.3.

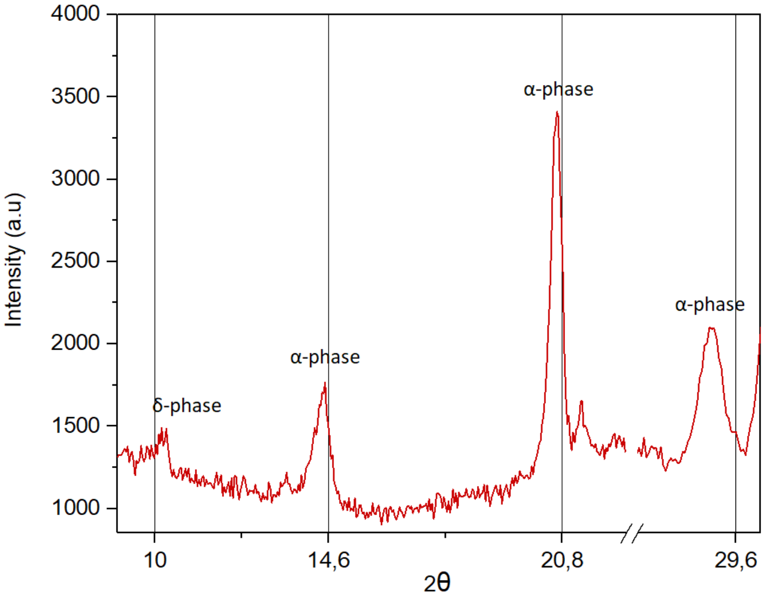

Figure 4.10: XRD analysis of a glass, ITO, and perovskite configuration

The following figures 4.11 and 4.12 present an XRD analysis of the cell configuration introduced in section 3.2, using the Spiro-TTB variant. The initial bump until 35° represents the signal of the amorphous material, glass. The only crystalline materials that give peaks in the XRD are ITO, perovskite and silver. The peaks of $CsPbI_2Br$ are slightly shifted compared to the baseline, because it concerns a high-bandgap perovskite in contrast to the medium-bandgap baseline. The shift indicates a lower packing of the atoms and an increased crystal plane spacing. The perovskite layer in figure 4.11 has a thickness of 280 nm, and in figure 4.12 it has a thickness of 165 nm. As hypothesised from the SEM top view, a change in layer thickness does not change lattice parameters. A comparison was performed by overlaying the consistent ITO peaks and observing if the perovskite peaks undergo a substantial shift. Through this method, the position of the perovskite peaks do not significantly depend on an instrument error. It was thus determined that the perovskite peaks are not shifted by a thickness change.

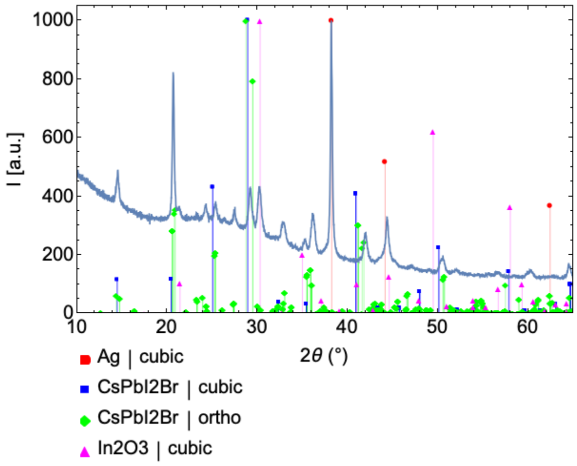

Figure 4.11:
XRD analysis of a cell using Spiro-TTB and a 280 nm perovskite layer

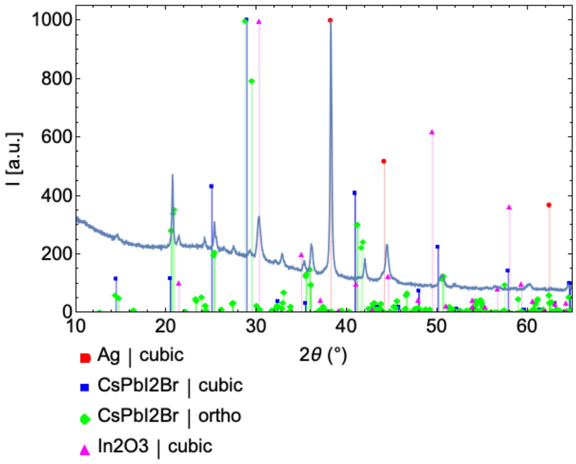

Figure 4.12:
XRD analysis of a complete cell using Spiro-TTB and a 165 nm perovskite layer

4.3 TEM analysis

The TEM analysis in this section is performed on the cell configuration introduced in this subsection 3.2, figure 3.1, using the Spiro-TTB variant.

4.3.1 Complete cell crystal structure

A TEM analysis confirmed the distorted cubic phase of the $CsPbI_2Br$, as introduced earlier in this section during the XRD analysis. Figure 4.13a portrays the results of a TEM analysis of the lattice parameters of $CsPbI_2Br$ as compared to a cubic and orthorhombic phase baseline. From comparison, the distorted cubic nature of the crystal structure becomes apparent. Figure 4.13b shows a baseline model of the ideal configuration of $CsPbI_2Br$ in a cubic structure. Figure 4.13c then shows the crystal structure of the analysed perovskite sample, which clearly has a distorted perovskite γ-phase.

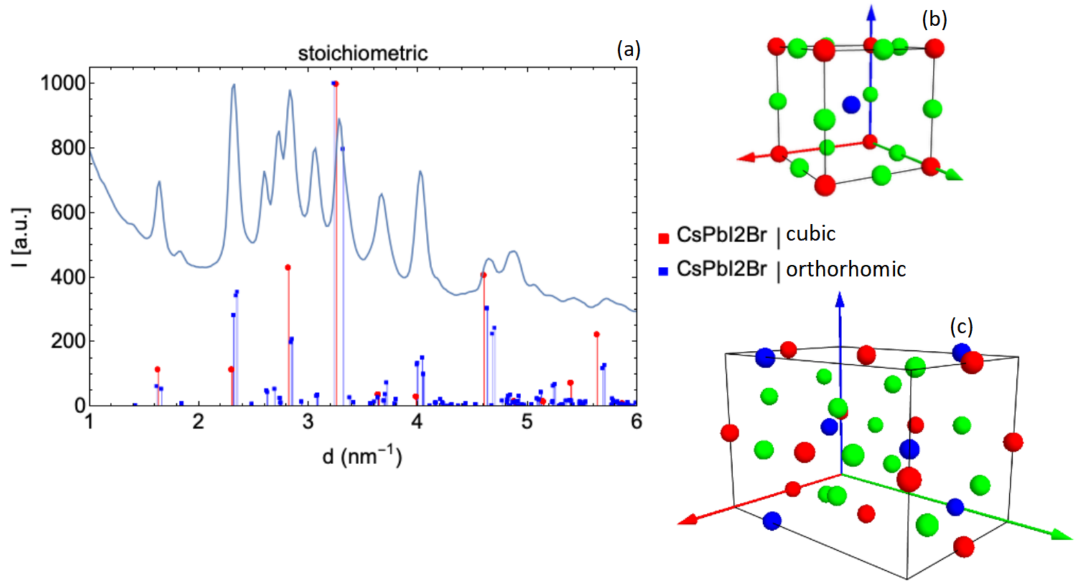

Figure 4.13: (a) TEM analysis of the perovskite lattice; (b) cubic structure of the perovskite; (c) distorted cubic structure of the perovskite.

4.3.2 Perovskite lattice variations

In order to determine the most effective composition for the co-evaporated $CsPbI_2Br$, and the necessary ratio of precursors, a TEM comparison is performed between a PbI_2-rich, a stoichiometric, and a CsBr-rich composition. The resulting structures are visualised in figure 4.14.

The PbI_2-rich perovskite at a TEM analysis exhibits an orthorhombic δ-phase (Pnma), which is not ideal for the purpose of a solar cell because of its poor photoactivity. The CsBr-rich perovskite is more stable than the stoichiometric composition. However, it has a lower short circuit current, possibly due to a higher number of trap levels in the energy gap. Furthermore, irregular large grains are generated among the background structure. Lastly, the stoichiometric and the CsBr-rich compositions generally results in distorted cubic structured grains. However, in addition to these distorted cubic grains they exhibit large irregular grains. These large grains are especially problematic because they have an orthorhombic crystal structure. The tolerance factor of $CsPbI_2Br$ is 0.855 [56], which does not fall in the desired range of $0.9 < t < 1.0$. Therefore, the γ-phase is explained by the lack of symmetry in the ion dimensions. Particularly the Cs^+ ion is of insufficient size. The different crystal structures that the perovskite can assume are modelled in figure 4.15.

Figure 4.16 further illustrates the existence of larger grains in the regular lattice of the stoichiometric perovskite, and figure 4.17 shows their average compositions. Additionally, the TEM analysis clearly portrays the generally stoichiometric nature of the $CsPbI_2Br$ lattice. The atomic composition of the general lattice is determined by STEM EDX and

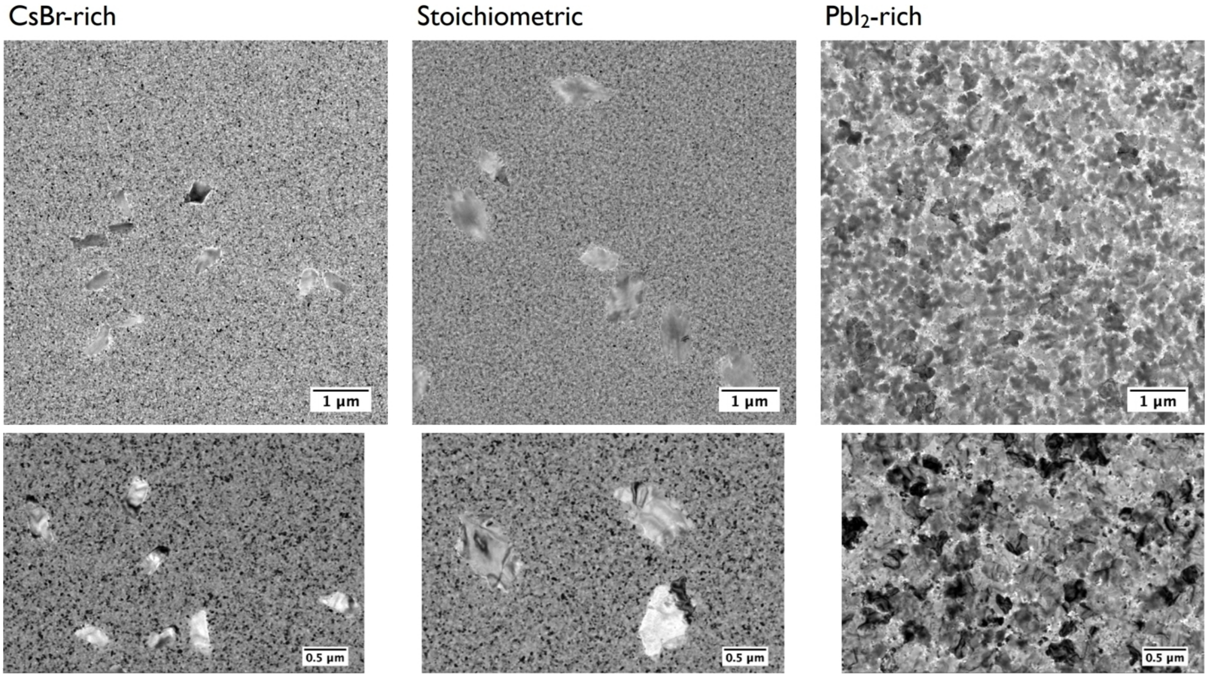

Figure 4.14: TEM top view of a CsBr-rich, a stoichiometric and a PbI_2-rich perovskite lattice

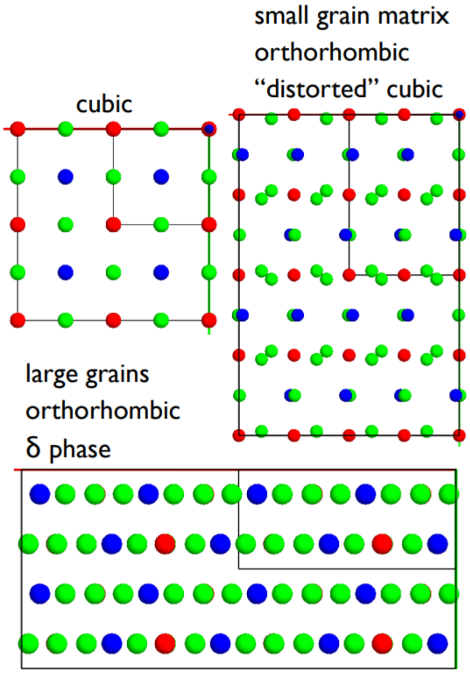

Figure 4.15: Modelled perovskite lattice structures

consists for 36.9 at% of I, and 22.4 at% of Br. In contrast, the atomic composition of the larger grains is 42.0 at% I, and 16.0 at% Br. The concentration of Iodine in the atomic composition of the larger grains is 5.1 at% more than in the general lattice, and the concentration of Br is 5.4 at% lower. This disrupted composition is the determinant factor of the delta phase property of the larger grain, as comparable to the behaviour of the PbI_2-rich perovskite. The chemical descriptor of the larger grain composition is $CsPbI_{2.17}Br_{0.83}$.

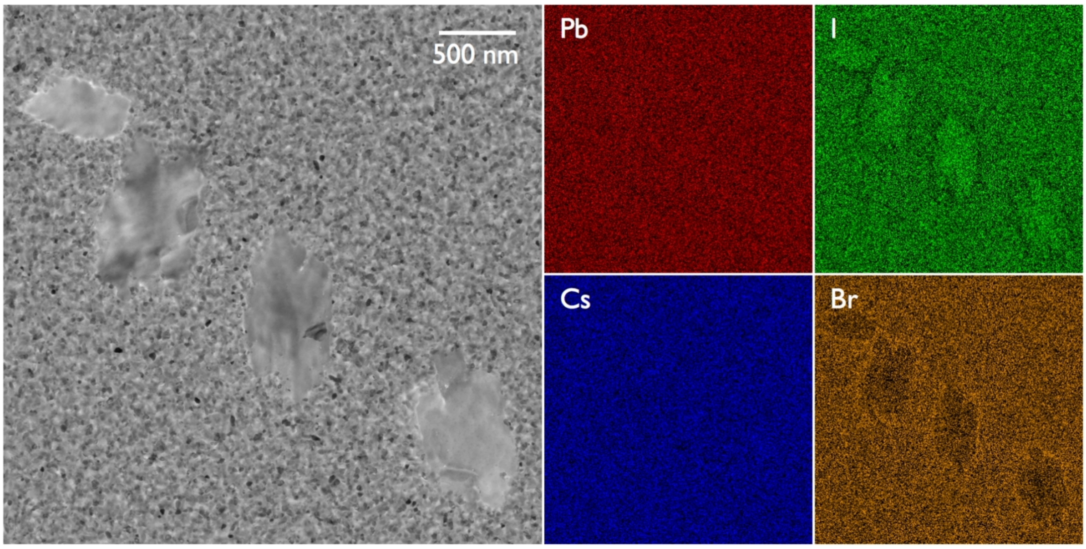

Figure 4.16: Zoomed TEM top view of stoichiometric perovskite showing qualitative material concentrations

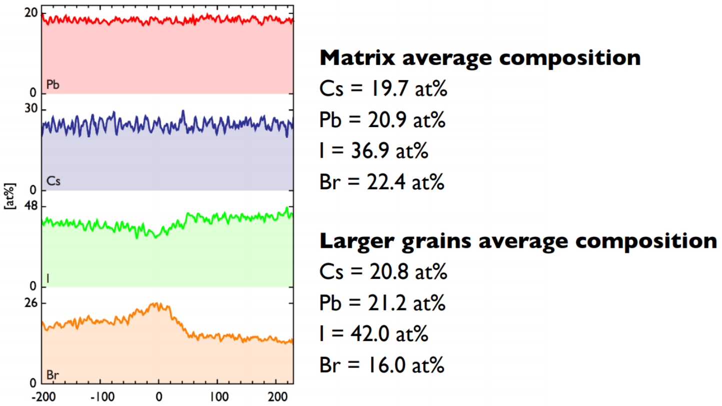

Matrix average composition
Cs = 19.7 at%
Pb = 20.9 at%
I = 36.9 at%
Br = 22.4 at%

Larger grains average composition
Cs = 20.8 at%
Pb = 21.2 at%
I = 42.0 at%
Br = 16.0 at%

Figure 4.17: Stoichiometric lattice and larger grains average composition

The effect of long-term air exposure on the perovskite crystal structure deposited on a substrate was analysed through TEM. In figure 4.18, a TEM top view of the fresh CsBr-rich perovskite sample is compared to a TEM top view of the same sample after six months of air exposure. The TEM top view of the fresh sample further confirms the composition of a distorted cubic lattice mixed with large orthorhombic grains after deposition. After six months of air-exposed storage of the sample, the larger δ-phase grains had expanded, and the sample had completely lost its γ-phase grains. Furthermore, a migration of the alkali halides is apparent. Figure 4.19 shows the concentrations of the different halides for the 6 months-old cell. The air-exposed sample exhibited an increase in bromide and a decrease in iodide in its grain boundaries, and a complementary phenomenon in its grain cores. In general, the chemical composition of the material can be described by $CsPb(I_X Br_{(1-X)})_3$. In this equation, X was determined to be approximately 0.733 for the grain cores, resulting in $CsPbI_{2.20}Br_{0.80}$ to describe their composition. Similarly, in the boundaries the composition was determined by $X \approx 0.174$, thus $CsPbI_{0.52}Br_{2.48}$.

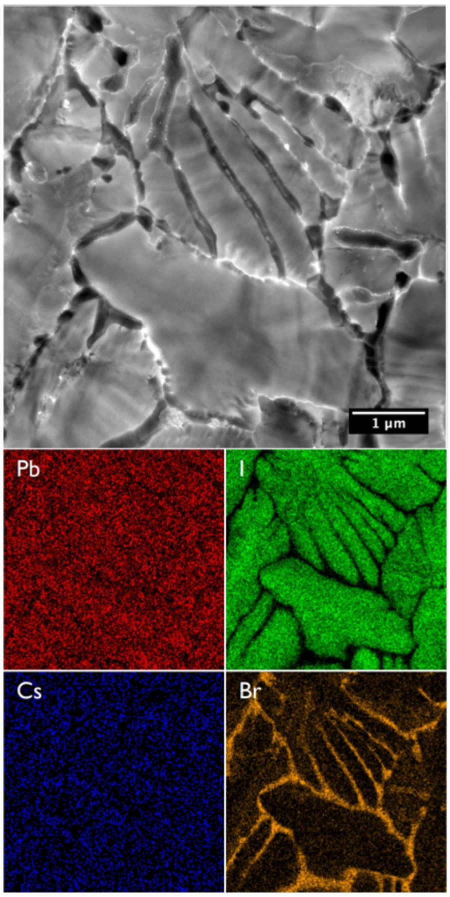

I-rich regions
Cs = 23.9 at%
Pb = 19.6 at%
I = 41.4 at%
Br = 15.1 at%

Br-rich regions
Cs = 27.0 at%
Pb = 13.4 at%
I = 10.0 at%
Br = 47.6 at%

Figure 4.18:
CsBr-rich perovskite lattice composition and TEM analysis after 6 months of air exposure

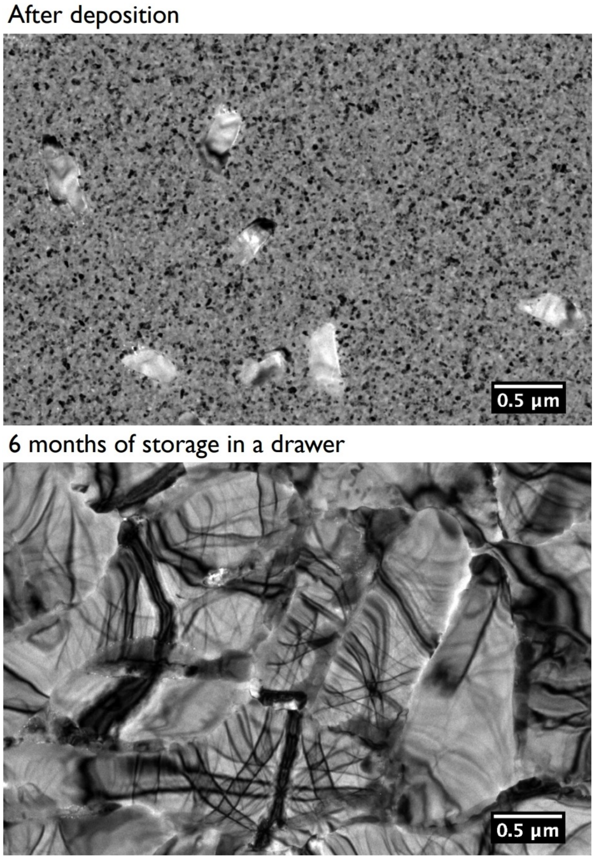
After deposition

6 months of storage in a drawer

Figure 4.19:
TEM top view comparison between a fresh CsBr-rich perovskite sample and after 6 months of air exposure

4.3.3 Uniformity of the perovskite layer

The following scanning TEM analysis is performed on two different solar cell configurations. The first of these configurations is comprised by glass, ITO, Spiro-TTB, perovskite ($CsPbI_2Br$), C_{60}, TmPyPb and silver. The other configuration is equal except for the replacement of the Spiro-TTB layer with NiO. These configurations were also described in section 3.2. The purpose of this section is to analyse the growth and crystallisation process of the perovskite layer on different HTLs. Cross sections of the two different cells, one with an HTL of Spiro-TTB and one with an HTL of NiO, are analysed through a TEM. The degree of mixture of CsBr and PbI_2 is investigated. This analysis returned a homogeneous perovskite layer with analogous characteristics across both cells. Furthermore, both cases exhibit a uniform lattice and an absence of pinholes. The figures 4.20 and 4.21 below clearly illustrate the uniformly distributed nature of the elements in both samples[ii], as indicated by the correct, uniform distribution of caesium, bromide, lead and iodine, exclusively in the perovskite layer.

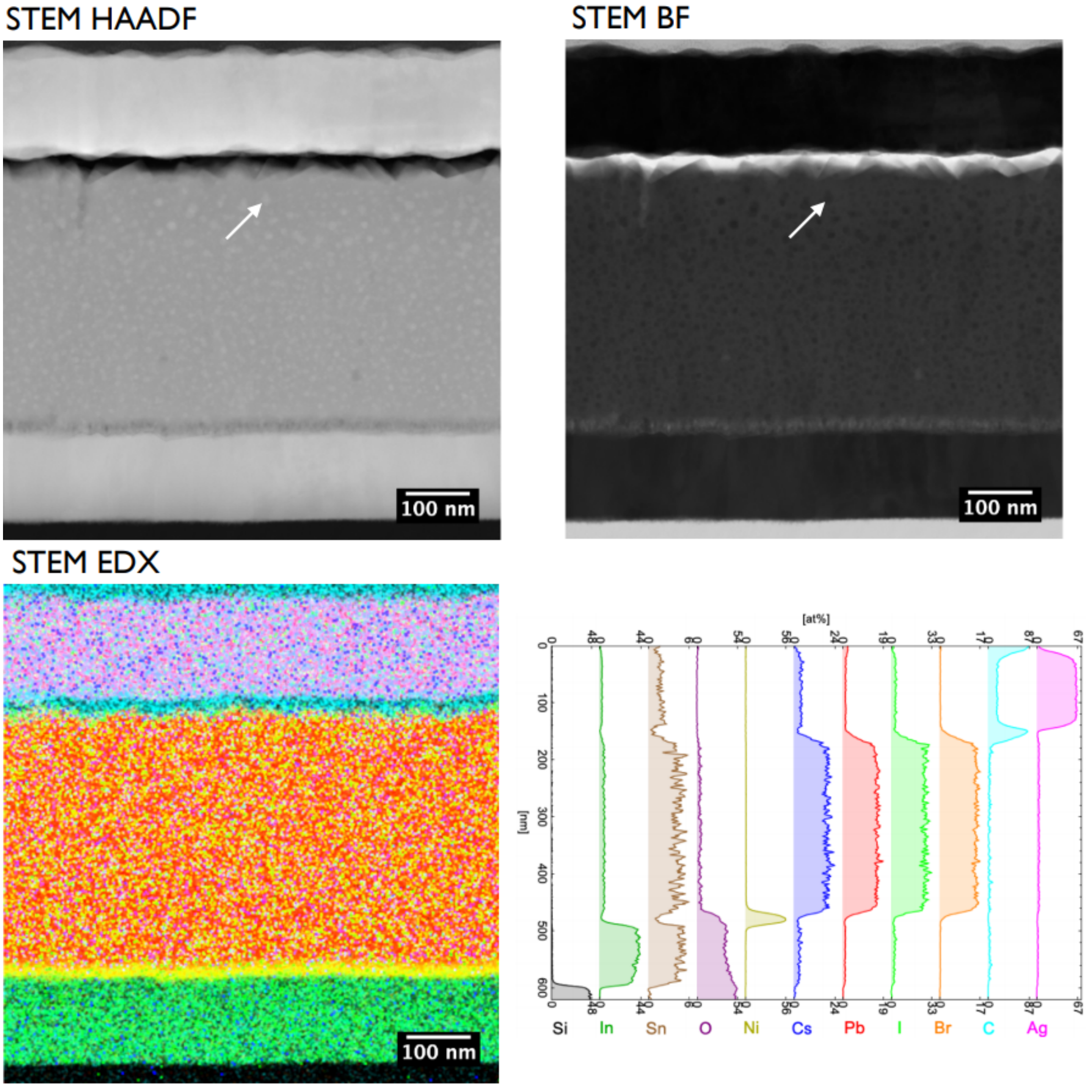

Figure 4.20: STEM high-angle annular dark-field, bright field, and energy-dispersive X-ray images, and local composition of a NiO HTL sample

---

[ii] The focused ion beam (FIB) sample preparation left Pb-rich regions as artefacts in the pictures, manifested as the dots indicated by the white arrows. These are not part of the general perovskite layer and can be disregarded in the analysis.

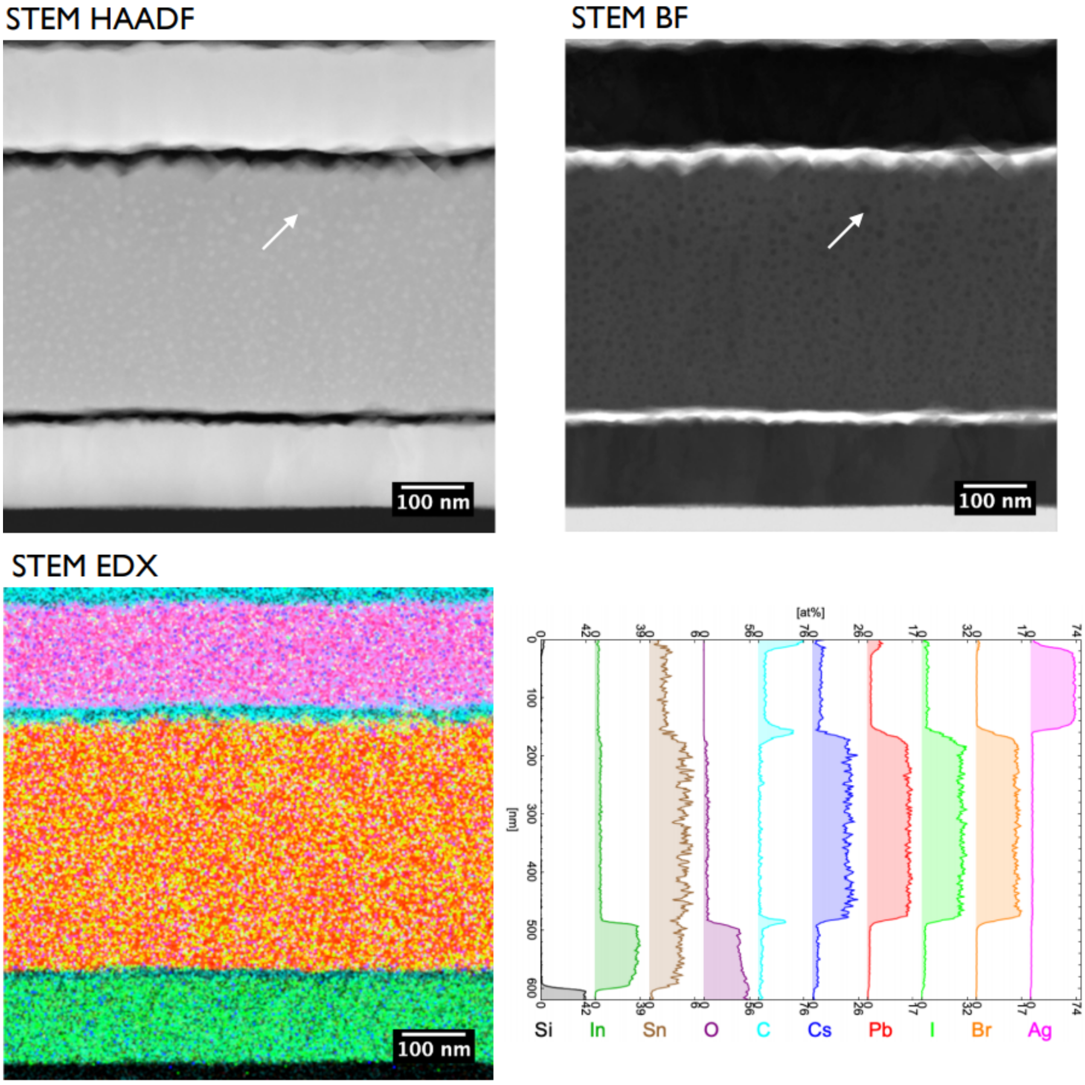

Figure 4.21: STEM high-angle annular dark-field, bright field, and energy-dispersive X-ray images, and local composition of a Spiro-TTB HTL sample

4.4 Phase segregation analysis

Phase segregation occurs in presence of mixed halides in the perovskite lattice structure. Under continuous light exposure, the two halides move in the crystal lattice, creating zones with higher concentration of one or the other. These zones have different bandgaps. This causes a red-shift in the bandgap peak in the PL measurements. Hoke et al. studied phase segregation through XRD measurements. The perovskite initially has a well defined XRD pattern, but after continuous light illumination it splits into two peaks. This symbolises the presence of two different lattices, with different lattice constants. In general, iodide-rich perovskite has a larger lattice constant than bromide-rich perovskite, opening the possibility of lattice zones rich in iodide and others rich in bromide that exhibit different properties [57]. Figure 4.22 illustrates what theoretically happens in the material under continuous light irradiation.

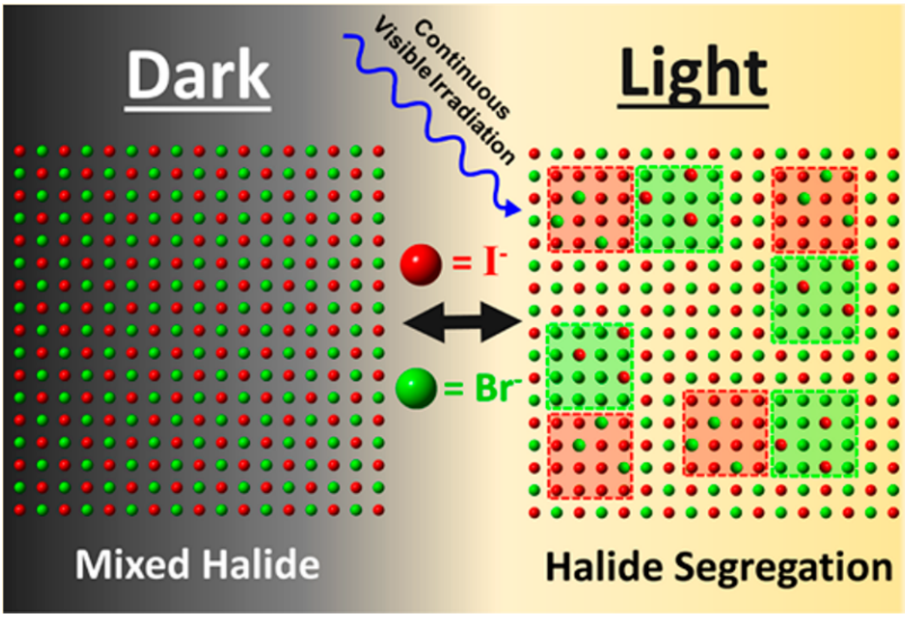

Figure 4.22: Halide segregation under continuous irradiation [66]

According to Hoke et al., the cell returned to the original XRD pattern after it was no longer exposed to light. This was further evident from a photoluminescence analysis. It can therefore be concluded that phase segregation is a reversible process [57]. To investigate if phase segregation was influenced by heating of the material during the illumination, measurements were performed on cooled substrates, where the same results were obtained. Bischak et al. explained the reversibility of the phenomenon with a polaronic model. It was hypothesised that the created carriers induce phase segregation through photon-electron coupling during light exposure. During this process, polarons are formed. The minimum Helmholtz free energy of the system is changed by these polarons, so that there is a different stable minimised free energy lattice for both the illuminated and the dark conditions [58]. Hoke et al. discussed the presence of an anisotropic strain that drives the ion to the pre-illumination configuration in dark conditions [57]. Furthermore, while the influence of the layer thickness on the phase segregation process was not taken into account by Hoke et al., Barker et al. observed an accelerated sub-bandgap growth and a higher final amplitude for thicker layers as compared to thinner layers, studying $MAPb(I_{1-X}Br_X)_3$, with $X = 0.85$ and perovskite layer thicknesses of 70 nm and 280 nm [59]. This phenomenon can be explained by the lower absorbance of 40% of the thin layer, compared to the 90% absorbance of the thick layer, having a thickness difference of 210 nm between the layers. According to Barker et al, the influences of the thickness, the illumination wavelength, and excitation geometry are caused by an internal gradient of halides, as formed by the generated carriers depending on the light intensity. Barker et al. further suggest the generation of a vertical gradient due to continuous illumination, driving the increased mobility of halides present on the surface [59]. Furthermore, phase segregation depends on vacancies and interstitial voids, because they result in a low energy migration configuration. Therefore, improving the homogeneity and the interface of the layer reduces the prevalence of phase segregation. However, the process of phase segregation is yet to be fully studied and understood. The main issue resulting from phase segregation is the bandgap change, causing a disruption in the electronic properties of the cell, particularly in the V_{oc} and the J_{sc}.

4.4.1 Effect on cell efficiency

Since phase segregation induces a change in bandgap, which implies a different absorbed photon energy, it indirectly influences the efficiency of the cell. The cell used for this investigation is the Spiro-TTB variant introduced in section 3.2, with a perovskite thickness of 200 nm, and an active area of 1.04 cm^2.

Figure 4.23 depicts the graphical analysis of the effects of increased phase segregation, including forward and reverse scan J-V graphs for the cell. The J_{sc} and the J_{mpp} both increase after two hours. This can be explained by the fact that an increased number of photons is absorbed at a lower energy gap, consequently increasing the current generated. A decrease over time in the V_{oc} is observed, and consequently in the fill factor in figure 4.24. This is caused by the deterioration of the interface under air exposure and by a decrease of the E_g. The efficiency of the cell thus decreases under influence of these phenomena. From the graphs, it is visible that the forward and reverse scans do not match. This is caused by mobile ions in one of the scanned materials, in this case in the $CsPbI_2Br$. This hysteretic behaviour which will be further investigated in section 5.4.

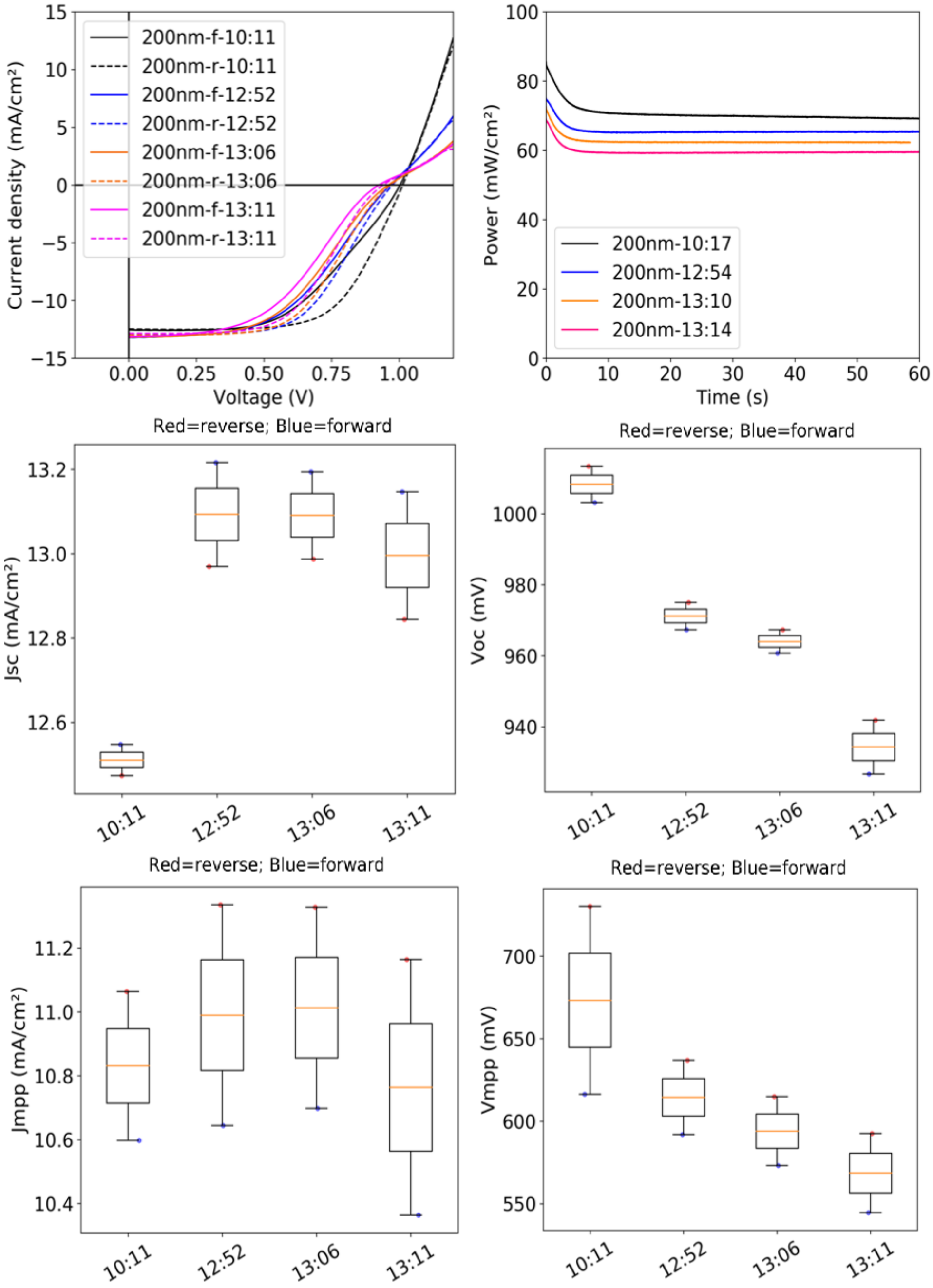

Figure 4.23: Effect of phase segregation over time on the properties of a Spiro-TTB HTL cell

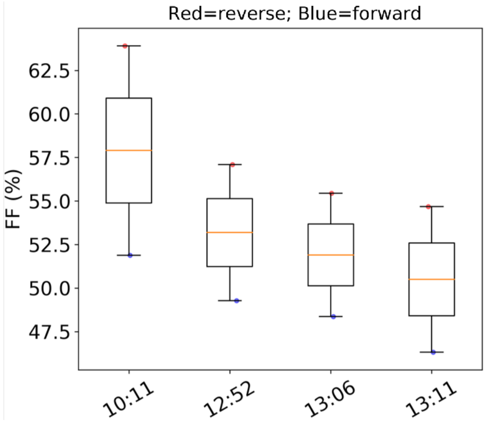

Figure 4.24: Effect of phase segregation over time on the fill factor of a Spiro-TTB HTL cell

4.4.2 Photoluminescence response analysis

The PL responses of the samples in this section were plotted using a bi-Gaussian where possible, and using LOWESS (Locally Weighted Scatterplot Smoothing) where necessary. Lastly, this section feature several measurements at 1 sun laser beam intensity. For these measurements, it was necessary to increase the integration time to 100 seconds, because the perovskite was not luminescent enough to show sufficient intensity counts for an analysis otherwise. The substrates that are used for the experiments in this section consist of glass, 125 nm of ITO, 15 nm of Spiro-TTB, and a varying perovskite layer thickness. The bandgap of $CsPbI_2Br$ is around 1.92 eV, which does generally not depend on the thickness of the perovskite layer. However, for particularly thin layers, the bandgap experiences a slight blue-shift. Figure 4.25 further illustrates this, notably the 70 nm layer blue-shift to 1.93 eV [iii].

[iii] The 70 nm sample was measured using 1 sun, while the others were measured using 10 suns. In order to make a visual comparison possible, the 10 sun measurements were divided by a factor of 90 for this graph. Furthermore, the detector causes a baseline peak for any 1 sun measurement at 2.03 eV, this should be disregarded.

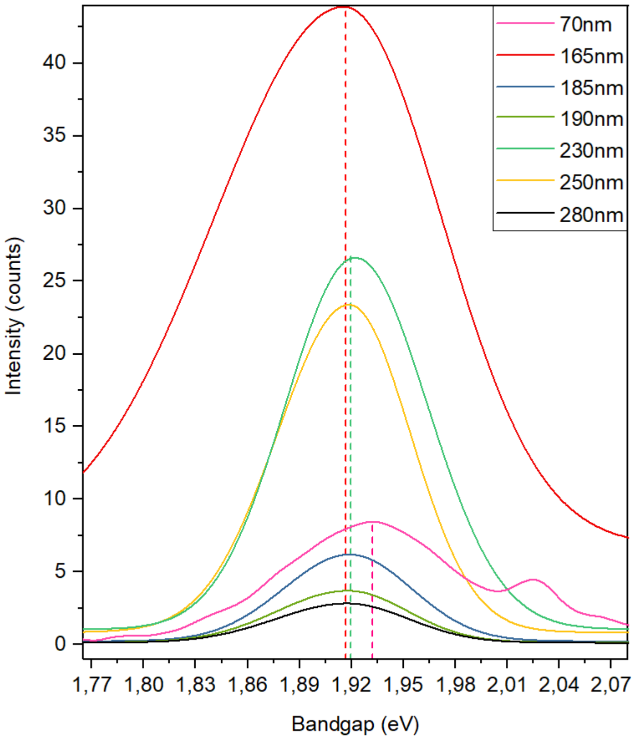

Figure 4.25: Initial PL response for different perovskite thicknesses

$MAPb(Br_XI_{1-X})_3$ perovskites segregate completely after being exposed for only a few seconds, as studied by Slotcavage et al [56]. Furthermore, Beal et al. and Zeng et al., in addition to Slotcavage et al., argued that the stoichiometric $CsPbI_2Br$ is stable and does not significantly exhibit phase segregation [60, 61, 56]. However, their results are based on short-term experiments and spin-coated perovskite. The long-term $CsPbI_2Br$ segregation process for a co-evaporated and stoichiometric compound mixture will be investigated in the analysis of this section. The most significant bandgap shift registered by the experiments was a red-shift from 1.92 eV to 1.82 eV.

For this analysis, PL responses were measured with a laser intensity of 10 suns. The measurement conditions are constant, with the substrates exposed to air, and all measurements performed on the same day. Figure 4.26 shows the PL responses of the investigated substrates, where they were tested at different points in time to investigate their stability. These measurements were done for 165 nm, 185 nm, 230 nm, and 280 nm perovskite layers. From the results, a bandgap red-shift is consistently visible. The quickest segregation happens for the 165 nm perovskite layer, taking only 50 min to reach a bandgap of 1.84 eV. In fact, a second peak in the PL graph appears after just one minute of exposure, signifying the presence of defect energy states with a lower bandgap. The slowest segregation is seen for the 185 nm perovskite substrate. The results are further tabulated in table 4.1.

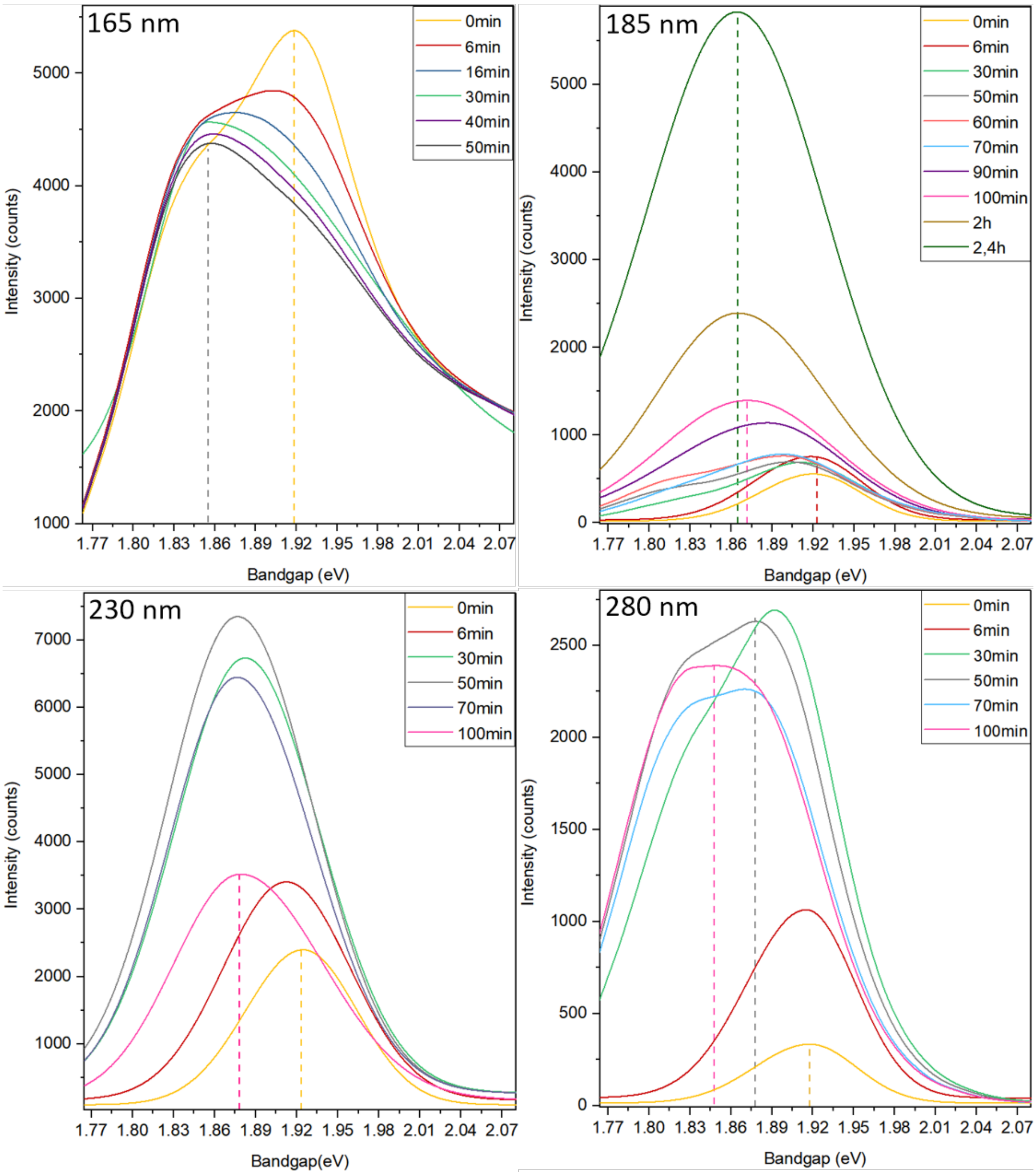

Figure 4.26: PL responses measured over time at 10 sun intensity for 165 nm, 185 nm, 230 nm, and 280 nm perovskite layers

	0 min	**6 min**	**30 min**	**50 min**	**70 min**	**100 min**
165 nm	1.919 eV	1.903 eV	1.859 eV	1.856 eV	-	-
185 nm	1.920 eV	1.920 eV	1.912 eV	1.903 eV	1.898 eV	1.872 eV
230 nm	1.924 eV	1.912 eV	1.882 eV	1.877 eV	1.877 eV	1.877 eV
280 nm	1.918 eV	1.916 eV	1.892 eV	1.881 eV	1.870 eV	1.848 eV

Table 4.1: PL response bandgap measurements at 10 sun intensity for different times of air exposure for substrates with varying perovskite layer thicknesses

To verify that the bandgap change does not only depend on the air exposure, the PL responses of two samples were compared: one exposed to air, in figure 4.27, and one under a dry, inert N_2 atmosphere, in figure 4.28. Both samples have an initial bandgap of 1.917 eV. After 3.4 hours, the substrate exposed to air reached a bandgap of 1.854 eV, while the one in the dry N_2 atmosphere reached 1.873 eV in the same time. This implies that the air exposure does have an adverse effect on the substrate photo-stability. The phase segregation is slightly faster in air.

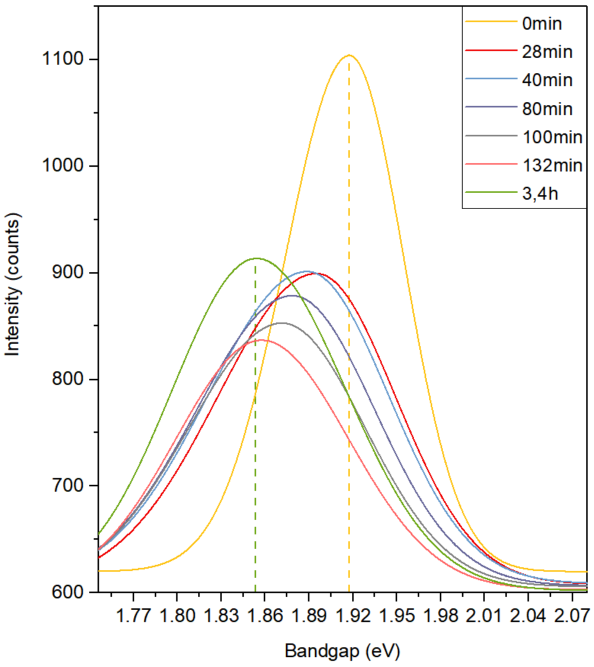

Figure 4.27:
PL response over time under continuous light-exposure of an air-exposed sample

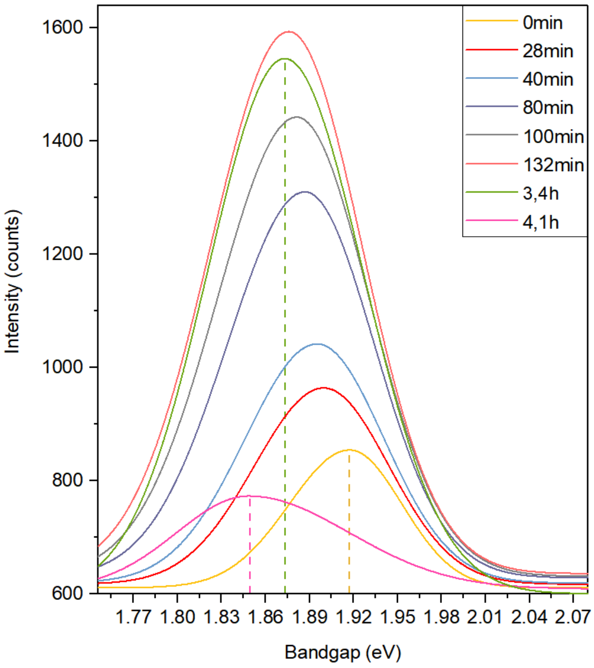

Figure 4.28:
PL response of a sample over time under continuous light-exposure under a dry N_2 atmosphere

After this comparison, the N_2-exposed substrate was first let to phase segregate to the same bandgap as the air exposed substrate, and then both substrates were subjected to a period of rest in a completely dark environment. For both cells to start at the same bandgap, the sample placed under an N_2 atmosphere had to be exposed to the light beam for 44 minutes longer. Figure 4.29 and figure 4.30 illustrate the progression of the bandgaps of the substrates left in the dark. Both bandgaps eventually blue-shifted back to a value of 1.907 eV. This further verifies that the red-shift observed under light exposure is mainly caused by the phase segregation process, which is reversible. After one hour in the dark environment, the N_2-exposed substrate had shifted back to a bandgap of 1.894 eV. In contrast, the air exposed sample reached a bandgap of 1.873 eV after an hour in the dark. From this data, it is concluded that the air exposed sample takes a longer time to return to its original crystal structure.

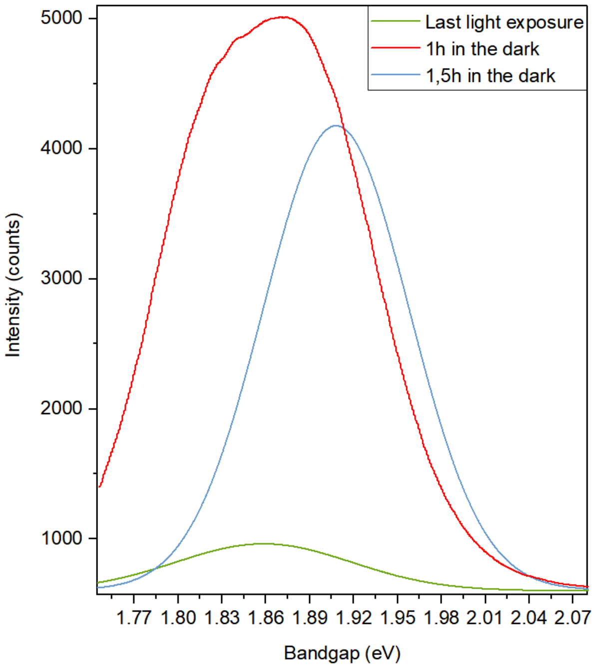

Figure 4.29:
PL response after periods of darkness of an air-exposed sample

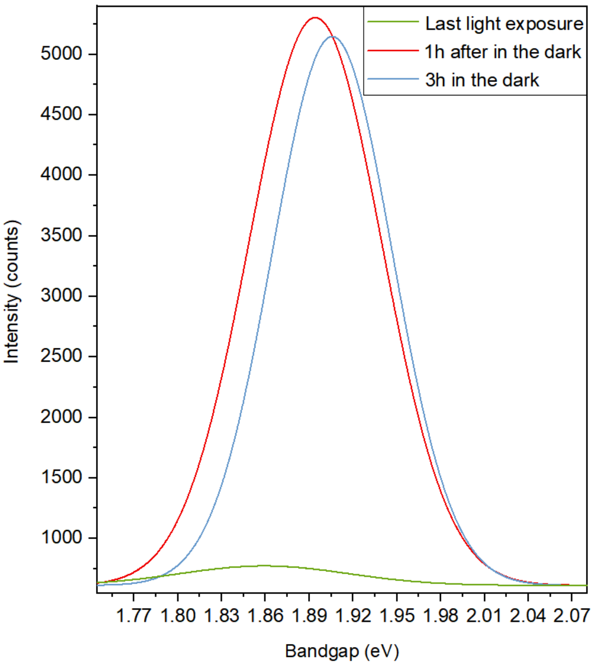

Figure 4.30:
PL response after periods of darkness of an sample under a dry N_2 atmosphere

After this period in the dark, the samples were re-exposed to a laser beam of 10 suns intensity, in order to test their stability after the reversed phase segregation. At this second exposure, the air-exposed sample was already completely phase segregated to a bandgap of 1.825 eV after 80 min, as portrayed in figure 4.31. This is in contrast to the first exposure, where the bandgap had only shifted to 1.854 eV after 3.4 hours. In figure 4.32, the sample in N_2 atmosphere exhibits a bandgap shift to 1.845 eV in 80 minutes. These results show that the phase segregation is significantly accelerated during the second exposure, implying that the precedent exposure weakened or modified the original crystal structure of the perovskite. Furthermore, during the second exposure, the influence of air-exposure became more evident.

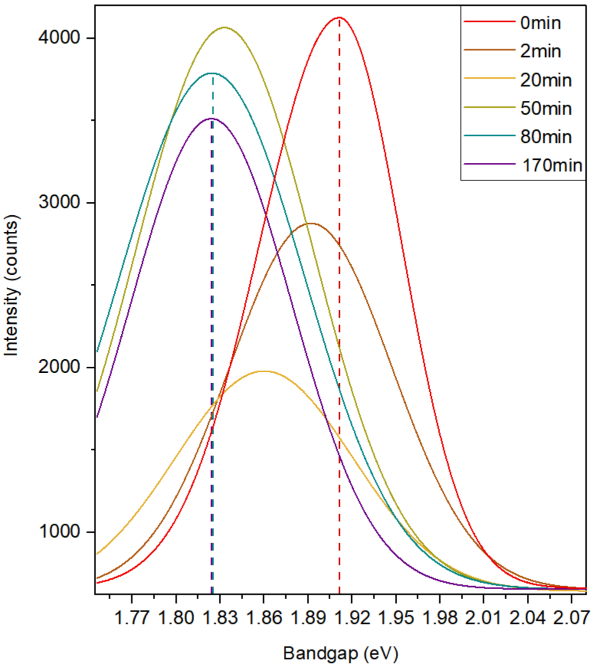

Figure 4.31:
PL response over time under continuous light-exposure of an air-exposed sample at second exposure

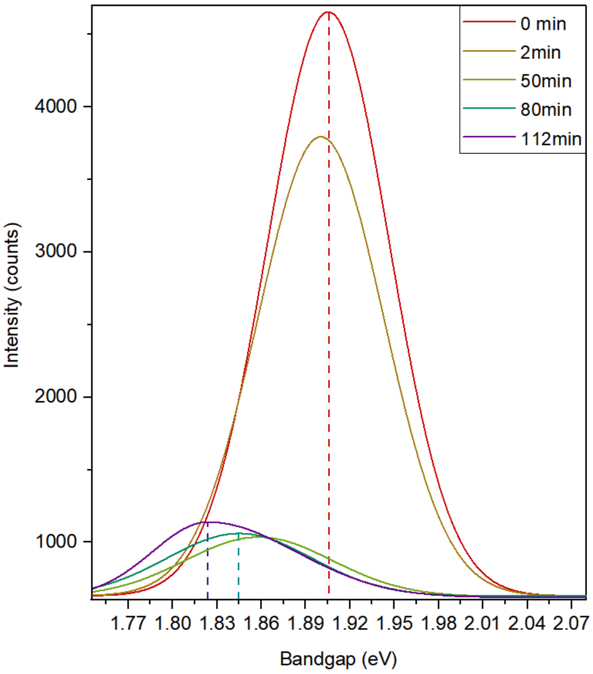

Figure 4.32:
PL response of a sample over time under continuous light-exposure under a dry N_2 atmosphere at second exposure

To prove that the observed red-shift phenomenon is due to phase segregation and not to degradation, the air-exposed substrate was left to rest in the air-exposed environment for 48 hours, and measured at several points in time to register its degradation. Evaporated layers exhibit conformality issues at the edges of the deposition plate, i.e. a thickness difference is found between the core and edges of the layer. This is attributed to the deposition plate slightly screening the cell from the evaporated material, so that the edges close to it are thinner than the main part of the layer. Consequently, (co-)evaporated perovskite layers usually degrade from the edges of the layer inward, since the edge of the perovskite layer is thinner and thin layers degrade more rapidly, as discussed in section 4.1.2. The edges of the substrate were therefore measured to obtain the most significant degradation results.

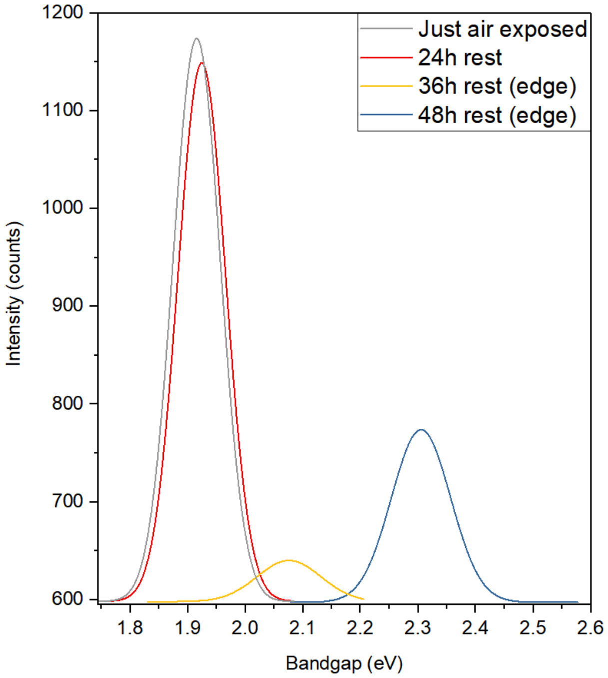

Figure 4.33: PL response of a sample after varying periods of air-exposure in darkness

As portrayed in figure 4.33, after 24 hours the core of the substrate was measured to already observe a slight degradation. From that point, the other measurements were performed at various spots along the edges of the sample. From these measurements, it is evident how the bandgap energy increases due to degradation. This is explained by the fact that the perovskite degrades into its orthorhombic δ-phase, which has a bandgap of 2.85 eV [48], causing a blue-shift in the overall material.

In order to investigate the influence of light intensity of the rate of phase segregation, a sample subjected to a laser beam of 10 suns intensity is compared to a sample subjected to 1 sun intensity. Both samples employ a 190 nm perovskite layer thickness. After 245 minutes, the sample subjected to the 10 suns laser beam attained a bandgap of 1.85 eV, as shown in figure 4.34, while the sample subjected to 1 sun still had a bandgap of 1.89 eV after 245 minutes, though with a second peak starts to appear at a lower bandgap, as shown in figure 4.35 [iv]. However, after 291 minutes, the bandgap change is insignificant and the main bandgap is still at 1.88 eV. It is therefore concluded that the phase segregation happens at a higher rate under the 10 sun light beam. Consequently, this data suggests that the rate of phase transition under light exposure depends on light intensity.

[iv] The detector causes a baseline peak in the LOWESS plot for any 1 sun measurement at 2.03 eV, this should be disregarded.

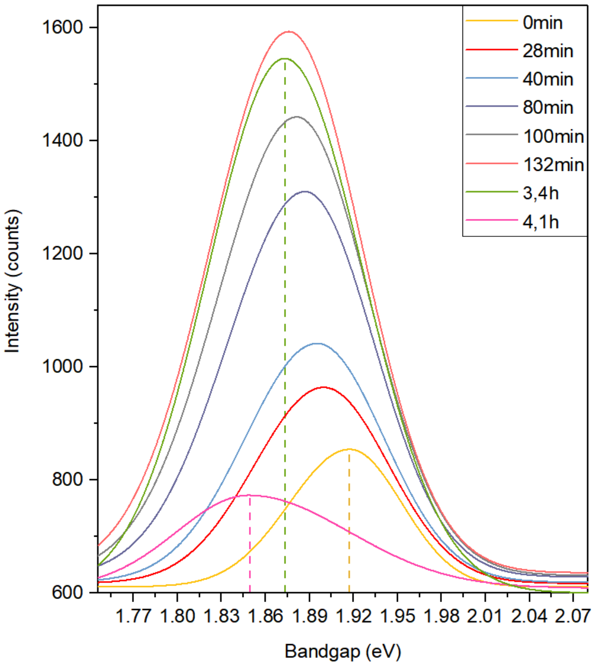

Figure 4.34:
PL response over time of a sample under continuous light-exposure measured at 10 suns

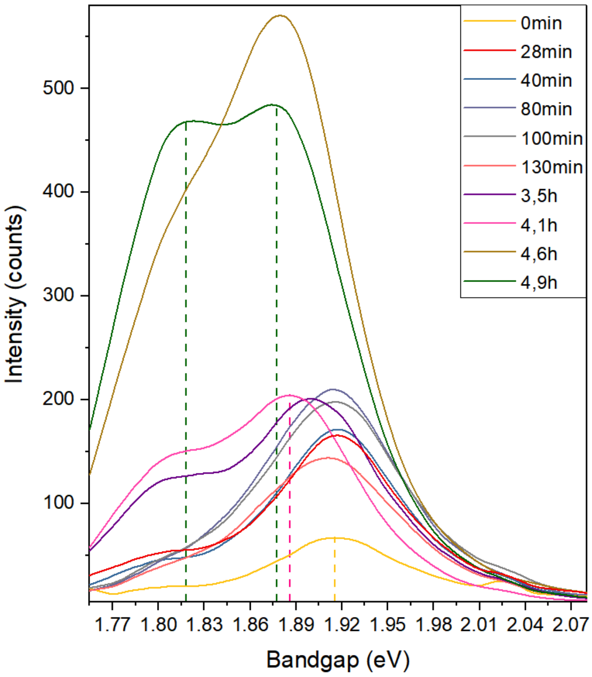

Figure 4.35:
PL response over time of a sample under continuous light-exposure measured at 1 sun

Also for 1 sun illumination, analysing perovskite thicknesses of 70 nm, 190 nm and 280 nm, it is clear that the time for having phase segregation increases at the increasing of the thickness of the perovskite layer.

The influence of the perovskite layer thickness was further investigated through PL measurements with a laser intensity of one sun. Three samples with different perovskite thicknesses were measured over time, one of 70 nm, one of 190 nm, and one of 280 nm. For this comparison, the thickness of 70 nm was specifically chosen to verify that the phase segregation occurs more rapidly for thin perovskite layers, in contrast with organic perovskiten [59]. The PL responses are graphed in figure 4.36. As hypothesised, the thin 70 nm perovskite layer exhibits the highest rate of phase segregation, and this rate decreases as the perovskite layer thickness increases. Furthermore, the significant results are tabulated in table 4.2.

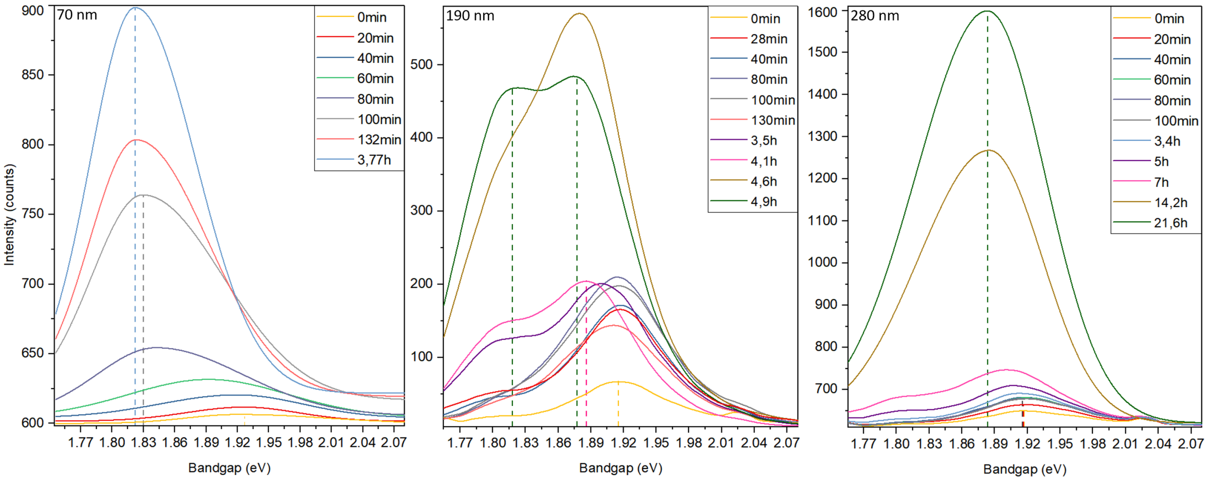

Figure 4.36: PL responses measured over time at 1 sun intensity for 70 nm, 190 nm, and 280 nm perovskite layers

	0 min	**40 min**	**80 min**	**100 min**	**4 hours**	**5 hours**
70 nm	1.927 eV	1.918 eV	1.841 eV	1.830 eV	1.822 eV	-
190 nm	1.916 eV	1.916 eV	1.915 eV	1.915 eV	1.886 eV	1.877 eV
280 nm	1.916 eV	1.916 eV	1.916 eV	1.916 eV	-	1.907 eV

Table 4.2: PL response bandgap measurements at 1 sun intensity for different times of air exposure for substrates with varying perovskite layer thicknesses

During this analysis, the difference in absorbance between 70 nm and 280 nm perovskite samples was additionally observed. The 70 nm layer absorbs considerably less than the 280 nm layer. This is illustrated by figure 4.37. Furthermore, the difference in reflectivity can be visually confirmed by the appearance of the cells, as the 280 nm sample appears more opaque than the 70 nm sample, which is shown in figure 4.38.

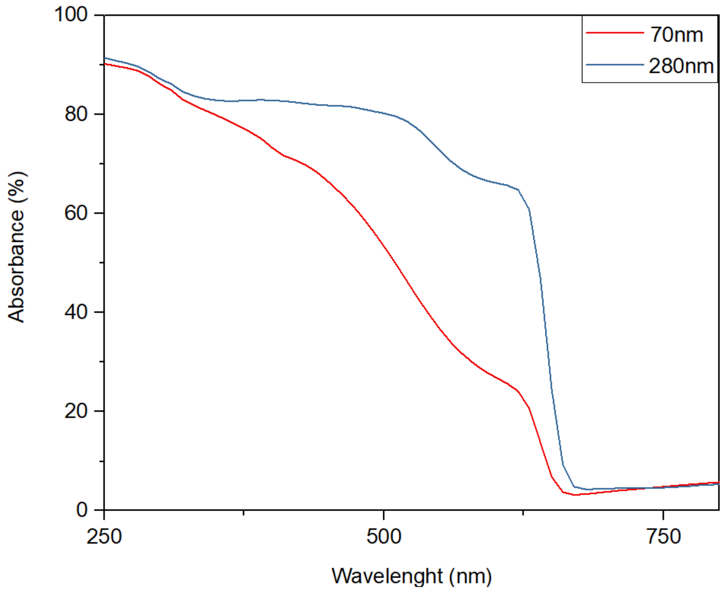

Figure 4.37: Absorbance comparison of samples of varying perovskite thickness on Spiro-TTB

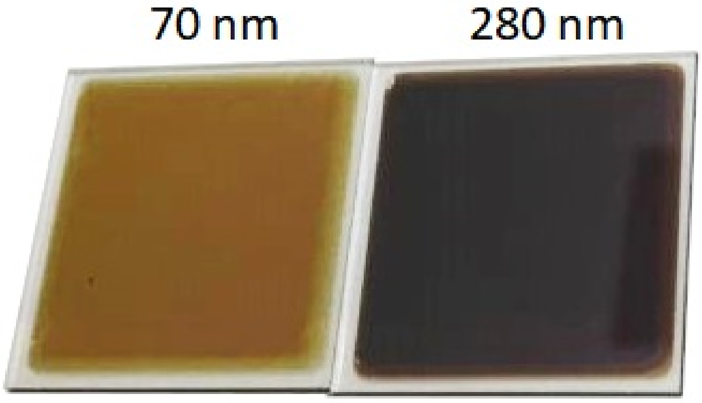

Figure 4.38: Visual difference in opacity between a 70 nm and a 280 nm perovskite samples

To determine how the phase segregation is influenced by the crystallographic change developed in the perovskite atomic-structure through annealing, three samples were compared after being subjected to varying annealing temperatures. All these samples have a perovskite layer thickness of 190 nm. The first sample is not annealed and it has an initial bandgap of 1.916 eV, the second sample is annealed at 80°C and starts with a bandgap of 1.909 eV, and the last sample is annealed at 100°C and starts with a bandgap of 1.918 eV. Both annealing processes lasted for 10 minutes. These initial bandgaps are graphed in figure 4.39. These initial differences in bandgap might be explained by a crystal structure change that comes with the process of annealing, which will be further investigated by section 4.5.

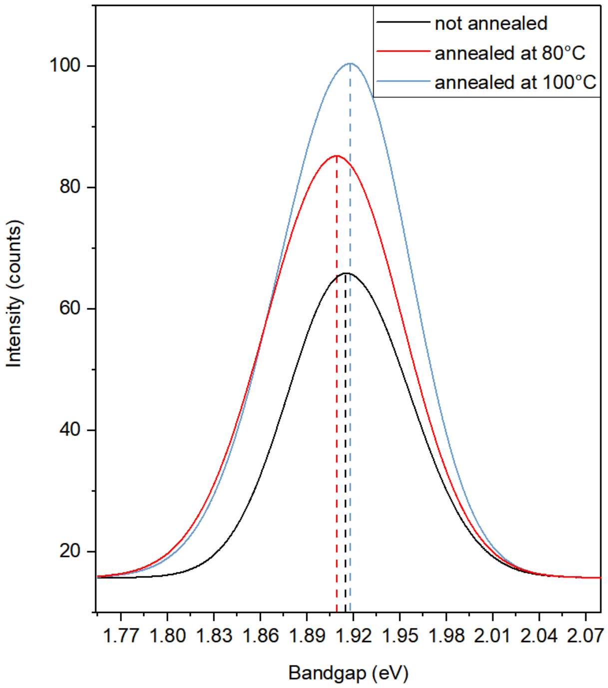

Figure 4.39: Initial PL responses for samples after varying annealing steps

The PL responses of the not annealed, 80°C annealed, and 100°C annealed samples are pictured in figure 4.40 [v]. As visible from these plots, only the 100°C annealed sample exhibits a bandgap shift at 72 minutes, the other samples remain insignificantly changed. From this it can be concluded that annealing at this temperature modifies the perovskite crystal structure in a way that induces a higher rate of phase segregation as compared to annealing at other temperatures, or no annealing at all.

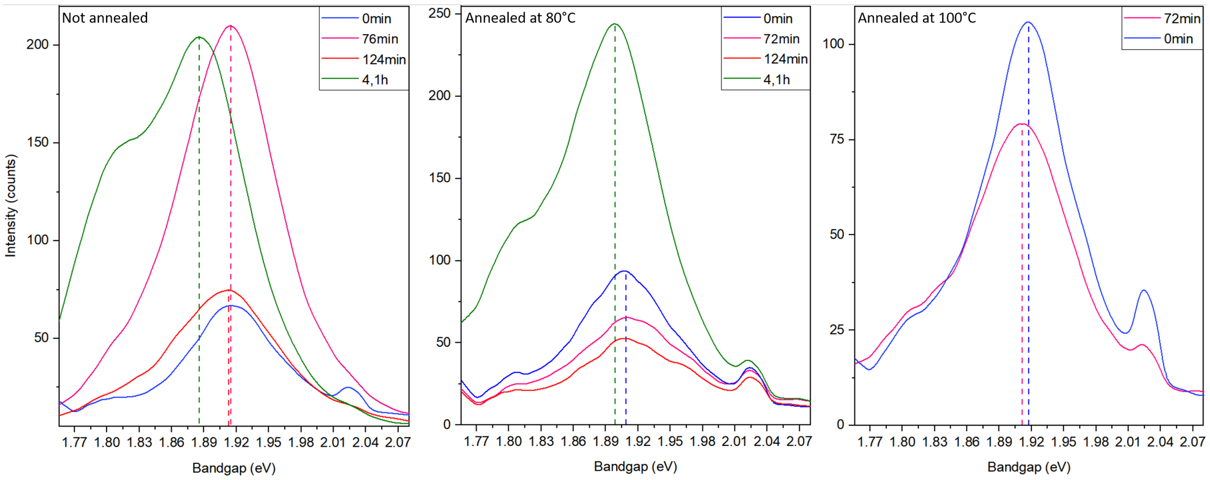

Figure 4.40: PL responses of annealed samples measured over time at 1 sun intensity

A closer comparison is made between the not annealed and the 80°C annealed sample.

---

[v] The detector causes a baseline peak in the LOWESS plot for any 1 sun measurement at 2.03 eV, this should be disregarded.

The results are graphed in figure 4.41. As described before, the 80°C annealed sample has a 0.007 eV lower bandgap. After 124 minutes, the not annealed sample has caught up and overpassed the 80°C annealed sample in a red-shift. After 246 min, the bandgap of the not annealed sample has shifted from 1.916 eV to 1.886 eV with a pronounced additional peak, and the 80°C annealed sample only experienced a bandgap shift from 1.909 eV to 1.899 eV. Thus, the annealed sample reveals to be more resistant to phase segregation.

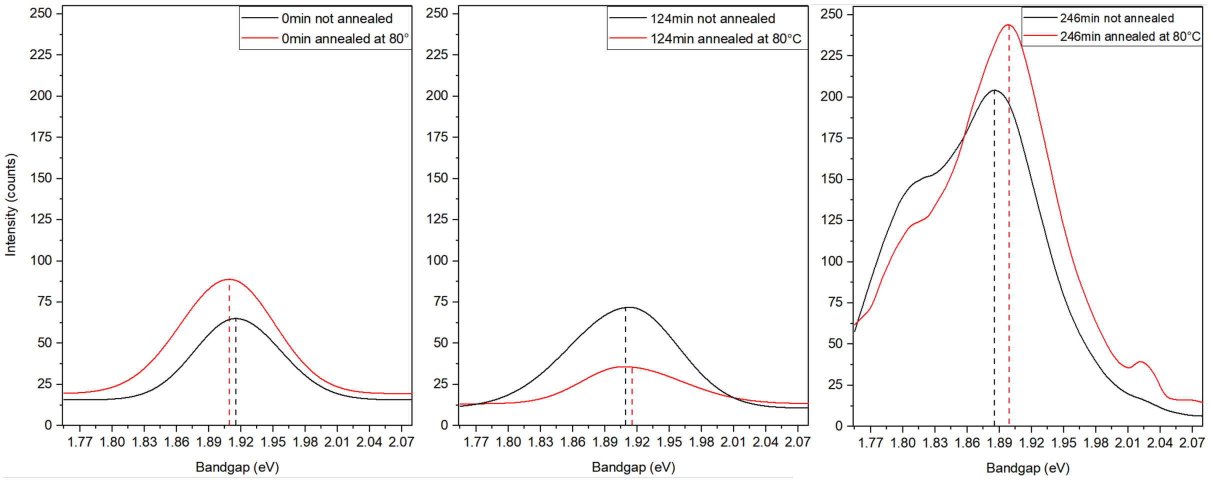

Figure 4.41: Phase segregation comparison between an 80°C annealed and a not annealed sample

4.5 XRD and absorptance of annealed samples

An XRD measurement confirms the presence of different crystal structures in the not annealed compared to the annealed samples. These are part of the cause of the varying initial bandgaps as found in the previous comparison. The alpha peaks of cubic phase $CsPbI_2Br$ are at 14.6°, 20.8°, and 29.6° [50], as indicated in figure 4.42. The investigated samples are seen to have a γ-phase, since the peaks do not entirely coincide with these. Most notably, the peak that should be at 29.6° is shifted significantly. Furthermore, an orthorhombic phase peak can be observed in the XRD measurement of the not annealed sample, around 10°. This peak is absent in the annealed samples.

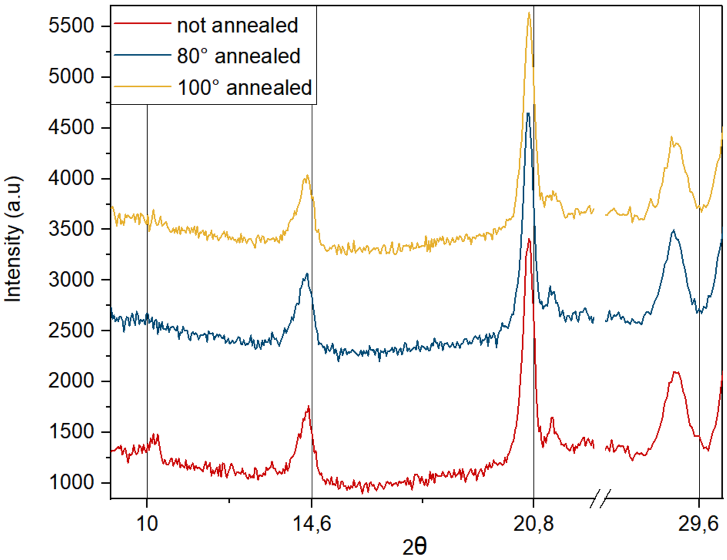

Figure 4.42: XRD analysis of samples after varying annealing steps

The other part of the cause of the varying initial bandgaps can be the varying presence of defects in the respective lattices. The presence of a higher quantity of defects for the 100°C annealed sample is confirmed by an analysis of the absorption coefficients, as portrayed in figure 4.43. Analysing the logarithm of the absorption coefficient from 1.2 eV to 1.8 eV, the not annealed cell has the lowest absorption coefficient, and this coefficient increases for higher annealing temperatures. For 80°C this increase can be said to be negligible, but for 100°C the defect concentration has rapidly increased, showing a clear rise in the absorption coefficient. Annealing allows a better inter-diffusion of the species, a better perovskite crystallisation, a higher absorption coefficient. However at the increasing of the annealing temperature a higher concentration of defects is present in the layer, especially for the annealing temperature of 100°C. The Urbach energies calculated are 31.17 meV, 32.66 meV and 33.96 meV respectively for the not annealed sample, the sample annealed at 80°C and the sample annealed at 100°C. This shows that more tails of localized states are present in the bandgap at the increasing of the annealing temperature. Furthermore at high temperature loosely bounded I^- or Br^- might leave the perovskite layer. Consequently, more pathways that allows ionic migration are present in the perovskite layer at 100°C.

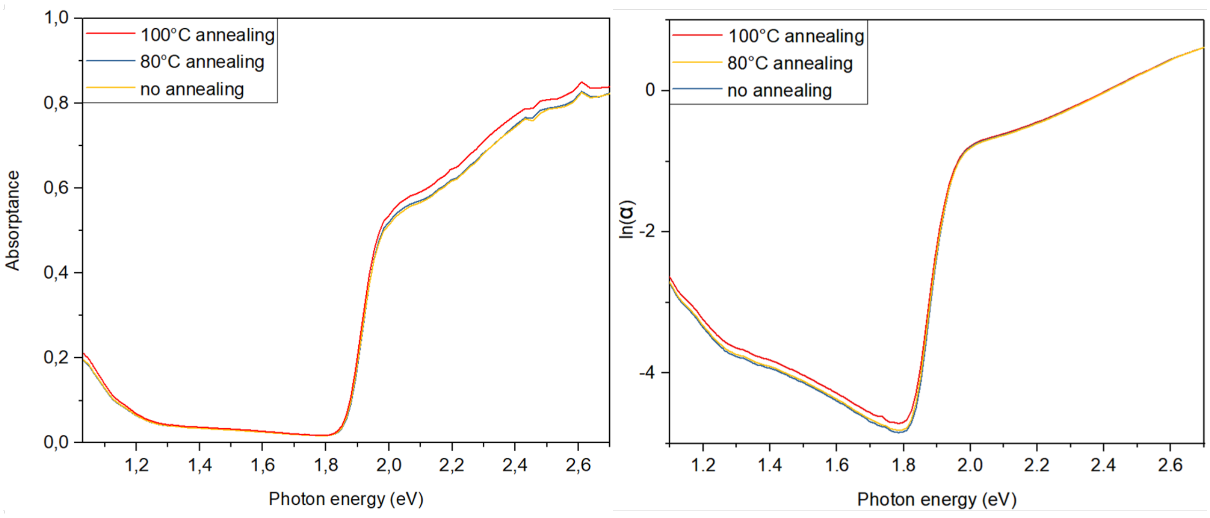

Figure 4.43: Absorptance and logarithm of the absorption coefficient of samples after varying annealing steps

4.6 Uniformity of J_{sc} distribution

The uniformity of the short circuit density of current was investigated using cells with an active area of 1.04 cm^2. The active area was virtually divided into six parts, where figure 4.44 includes an illustration of this division, and the J_{sc} in each of the parts was determined from an EQE response. The results of these measurements are then also portrayed in figure. From these, it is visible that the J_{sc} does not exhibit significant alterations across the six areas. It is concluded from this analysis that the J_{sc} of a cell can be considered uniform across its active area.

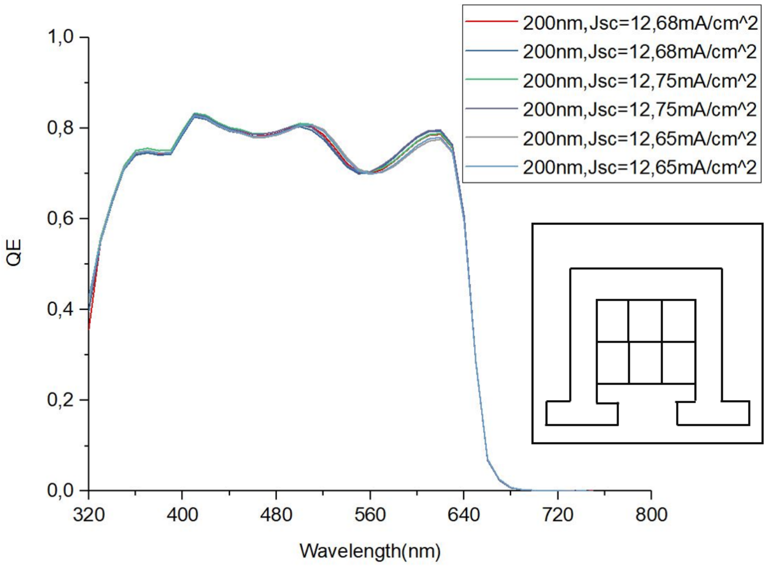

Figure 4.44: EQE response of six different sections on the active area of a sample, and the schematised division of these sections

5 Device Engineering

5.1 Thickness of the perovskite layer

This chapter will investigate the device properties of perovskite layer thicknesses using NiO or Spiro-TTB as an HTL. To compare different perovskite layer thicknesses in this section, the NiO and Spiro-TTB variants of the cell compositions introduced in section 3.2 were both utilised. An analysis was performed to quantify the influence of the thickness of the photoactive perovskite layer and to optimise the thickness for the two main hole transport layer materials. The resulting variations in the efficiency and stabilised PCE of both configurations are given in figure 5.1, and the variations in the J_{sc}, FF, and V_{oc} are graphed in figure 5.2.

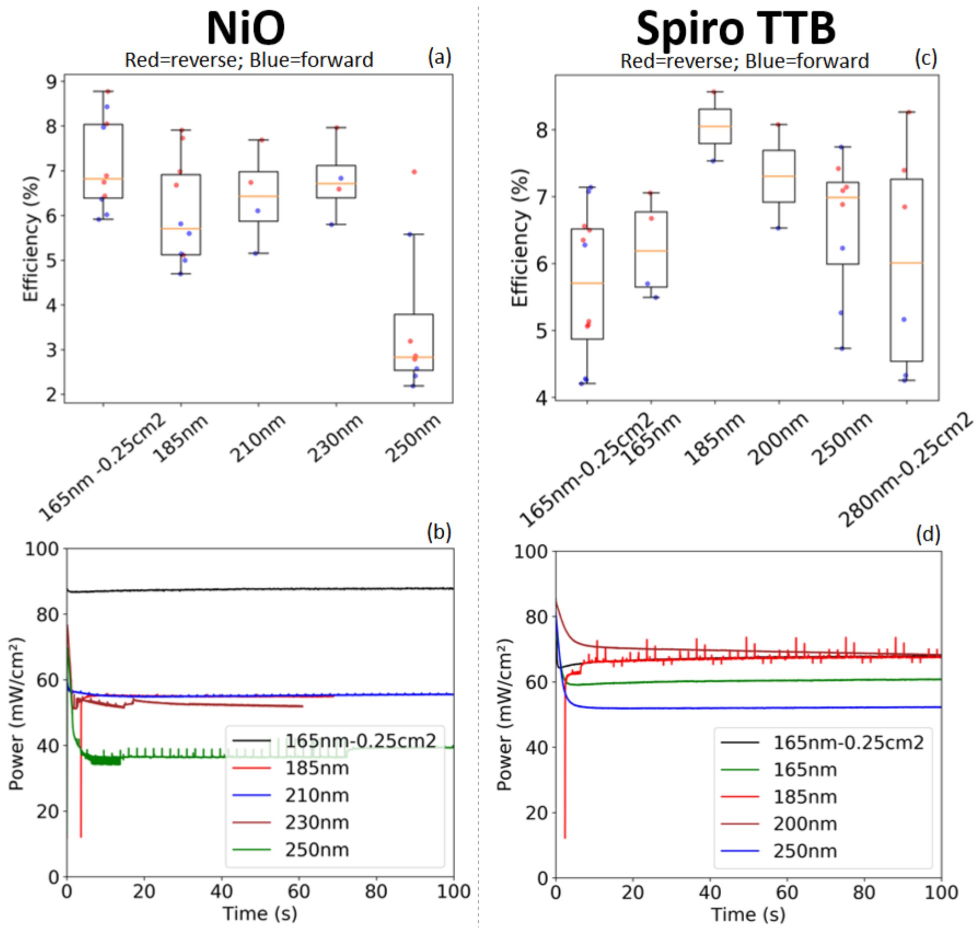

Figure 5.1: Efficiency and P_{mpp} comparison between samples with a NiO or a Spiro-TTB HTL for varying perovskite thicknesses

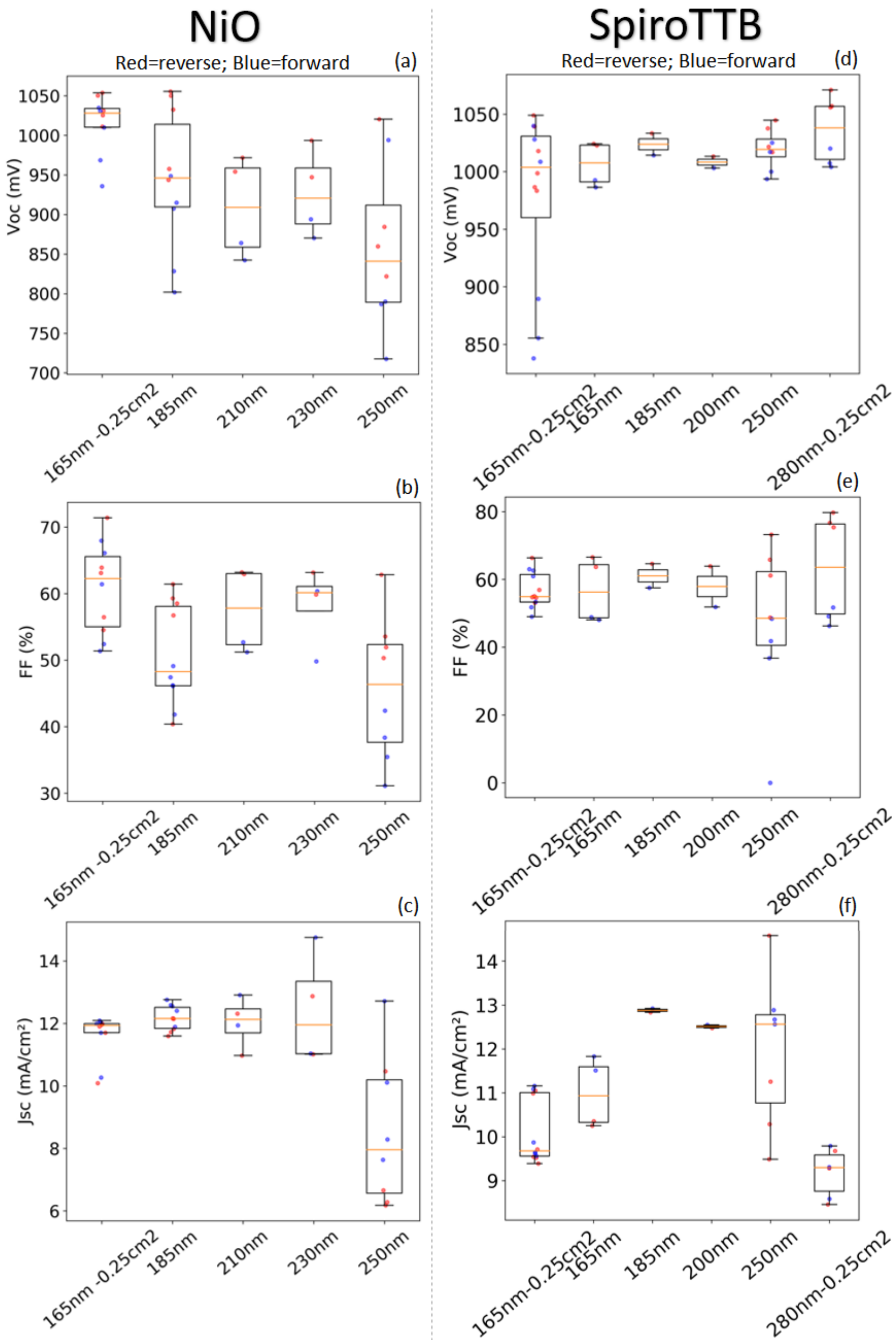

Figure 5.2: J_{sc}, FF, and V_{oc} comparison between samples with a NiO or a Spiro-TTB HTL for varying perovskite thicknesses

For the NiO HTL cells, the active area of the investigated cells is 1.04 cm^2, with the exception of one 0.25 cm^2 cell with a 165 nm perovskite layer for comparison. Similarly, the Spiro-TTB cells have an active area of 1.04 cm^2, with the exceptions of one 165 nm and one 280 nm perovskite layer cell, both of which use 0.25 cm^2.

5.1.1 Analysis of NiO cells

Looking at the graph in figure 5.1a, it is evident that the layer thicknesses until 250 nm exhibit favourable efficiency behaviour, but for thicker layers there is a sudden decrease of efficiency. Figure 5.1b presents the best measured mpp tracking result of the efficiency of the cells. From 165 nm to 210 nm it is possible to obtain good mpp trackings, at 230 nm it start to become less favourable, and it has dropped off significantly at 250 nm. From this result, the carrier lifetimes are too short to allow for diffusion lengths over 230 nm, as showed by the mpp tracking.

The open circuit voltage depends on the band alignment of the cell materials, and can be improved by optimising the interfaces. It is graphed in figure 5.2a Furthermore, the fill factor (FF) is plotted in figure 5.2b. It visibly decreases before 250 nm, as it depends on the J_{sc} and on the V_{oc}. Lastly, the established drop off in performance before 250 nm can also be illustrated by the sudden decrease of the short circuit current in figure 5.2c.

In conclusion, the highest short circuit current is obtained from 185 nm to 230 nm. Furthermore, the best V_{oc} can be obtained between 165-185 nm. The best cell obtained using the NiO HTL configuration reached an efficiency of 8.9% in mpp tracking. The size of this cell was 0.25 cm^2, the FF 71.4%, the V_{oc} 1.05 V, and the J_{sc} 11.7 A/m^2. In the forward scan the efficiency was 8.3%, in the reverse scan it was 8.8%. Lastly, it can be noted that the cell was tested to be fully stable overnight. These results were obtained while the cell was exposed to air.

5.1.2 Analysis of Spiro-TTB cells

Similar to the case with NiO, using Spiro-TTB a trend is observed that confirms the best perovskite thickness to be from 185 nm to 200 nm. However, in contrast to the case of NiO where 165 nm was a valid thickness, for Spiro-TTB 165 nm is below the lower limit, possibly explained by a deficiency of number of carriers for a low thickness in combination with the Spiro-TTB-perovskite band alignment. Figures 5.1c and 5.1d illustrate this further, clearly showing problematic behaviour for the 165 nm and the 250 nm samples. Furthermore, the best efficiency is found around a perovskite thickness of 185-200 nm. This is observable from the mpp tracking.

Spiro-TTB theoretically has a better band alignment with high-bandgap perovskite as compared to NiO, which translates into a higher V_{oc} value. Similar to the trend seen for the efficiency, the investigated Spiro-TTB cells exhibit the best J_{sc} and V_{oc} values around 185 nm. This is depicted in figures 5.2d and 5.1f. Figure 5.2e is included as a comparison to figure 5.2b. Lastly, the tested cells had a low hysteresis at 185 nm and 200 nm.

The best cell obtained using the Spiro-TTB variant of the configuration introduced in section 3.2 reached an efficiency of 7.2% in the mpp tracking. The size of this cell was 1.04 cm^2, the FF 71.4%, the V_{oc} 1.01 V, and the J_{sc} 12.7A/m^2. In the forward scan the efficiency was 6.5%, and in the reverse scan it was 8.1%, in which a hysteresis effect is seen.

5.1.3 EQE comparison

Figure 5.3 presents a set of EQE graphs, where cells of different thickness are compared. As stated in the figure, one compares the cells using a NiO HTL and one using a Spiro-TTB HTL. Across the two graphs, the cells with the same thickness (i.e. 165 nm, 185 nm, and 250 nm) were produced in the same batch, under the same conditions. It is apparent from the data that the J_{sc} attains the best values for perovskite thicknesses below 250 nm. It can be concluded that carrier extraction problems occurs at thicknesses higher than 230 nm. The recombination limit at this thickness would arise mainly because travel time across the thickness for the carriers exceeds their lifetime. Specifically, a thicker layer necessitates a longer carrier lifetime [2].

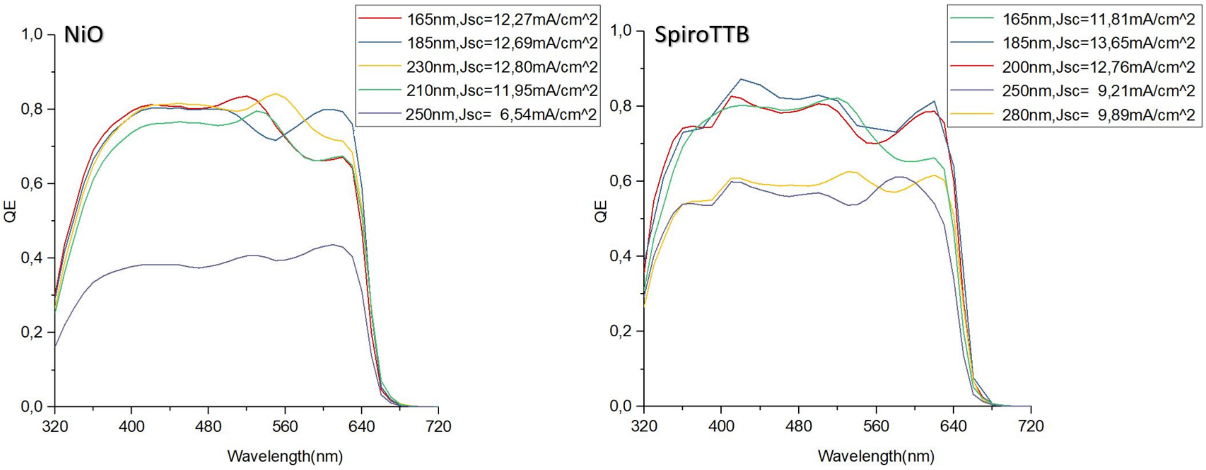

Figure 5.3: EQE comparison between samples with a NiO or a Spiro-TTB HTL for varying perovskite thicknesses

The EQE shape of the curves and the absorption of the perovskite layer can be juxtaposed to narrow down the location at which losses appear in the spectrum. These losses can derive from reflection or from a low absorbance of the layer at specific wavelengths. The absorbance of the NiO-perovskite substrates was plotted to investigate this further. Figure 5.4 portrays how the photon absorption increases with the thickness of the perovskite layer, especially for wavelengths between 480 nm and 650 nm.

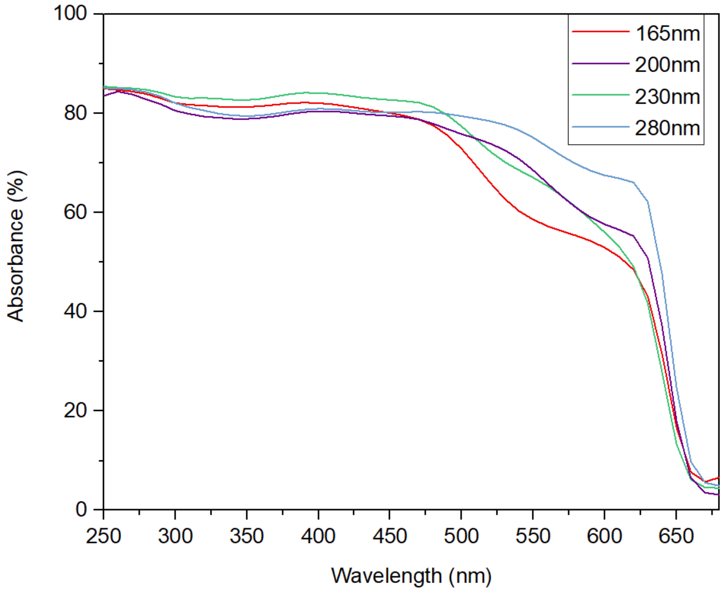

Figure 5.4: Absorbance comparison for varying perovskite thicknesses on NiO

The light beam generated by the EQE has to pass through the glass substrate and the HTL to excite the carriers in the active area. Therefore, it should be taken into account that the reflectivity of the glass slightly lowers the obtained current. This effect will be further analysed in section 5.2.

5.2 Anti-reflection coating

A comparison was made between the Spiro-TTB variant of the configurations introduced in section 3.2, and the same configuration but with an anti-reflection coating on the glass substrate. The results of this comparison are portrayed in figure 5.5. The quality of the anti-reflection coating was not specifically fit for application on the irradiance spectrum of this cell, as visible from the decreased QE for the shorter wavelengths (up to ≈400 nm). However, it is seen to counteract the reflection effect of the glass, normally most prominent between 400 nm and 650 nm on the spectrum. The combination of these effects results in a slightly improved short circuit current measurement by the EQE. This positive result can be further improved by fitting the anti-reflection coating to the applied spectrum.

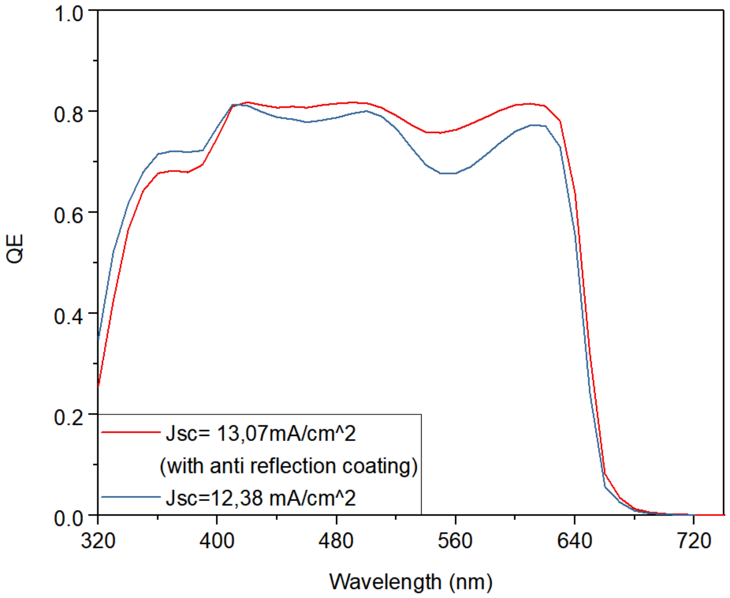

Figure 5.5: Comparison of EQE responses with or without anti-reflection coating

In addition to the reflectivity of the glass, the thickness of the HTL has an influence on the obtainable current. As the HTL absorption spectrum overlaps a part of the spectrum of perovskite, it absorbs part of the photons of certain wavelengths before they can reach the perovskite [62]. The thicker the HTL layer, the more prominent this effect becomes.

5.3 Scalability of the cell active area

The cell configuration employed for this section is the Spiro-TTB variant of the configurations introduced in section 3.2. The solar cells should be able to be scaled up in active area. Small active area have less resistance losses. Disadvantages of a small cell include that it is difficult to contact them in a module, and more contacts result in higher contact absorption losses. It can be hypothesised that the cell efficiency is not limited by the size of the solar cell active area if thermal co-evaporation is used, which can be investigated from the compared differences in active area.

The efficiencies of the scaled samples are similar, as illustrated by the forward and reverse scans. The largest difference is seen in the J_{sc}, but this can be attributed to the non-uniformity in thickness of the perovskite layer at the edges of the substrate. However, as seen in the mpp tracking in figure 5.1d of section 5.1, the larger cell has a significantly lower power, and therefore the small active cell area (165 nm/0.25 cm^2) almost has a 1% higher efficiency than the large active cell area (165 nm/1.04 cm^2). As discussed in section 4.4.2, the cell degrades the quickest at its edges due to the lower local thickness, and a larger cell will be more susceptible to these unless a deposition mask of sufficient size is used. Furthermore, larger active areas contain a larger quantity of defects, in addition to problems linked to the edges of the mask.

However, considering that the efficiency losses are not critical and seem to mainly scale linearly with the edge length, as opposed to the quadratic scaling of the active area, it is possible to roughly confirm the scalability of cells made through PVD. Furthermore, the edge issues could be simply negated through use of a larger deposition plate, so that the cells are not screened by it.

5.4 Engineering of electron transport layer

This section involves both configurations as introduced in section 3.2, where the ITO thickness is 120 nm, the respective Spiro-TTB or NiO thicknesses are 15 nm or 20 nm, C_{60} thickness is 20 nm, the TmPyPb thickness is 3 nm, and the silver thickness is 120 nm.

It is important that the perovskite layer is only in contact with the HTL and ETL, and not with e.g. the silver on top, as silver iodide is formed when the perovskite is in contact with the silver, which can be detrimental to the functionality of a cell [63]. Therefore, it is crucial that the ETL is homogeneous and protective between the perovskite and the silver to resist the diffusion of the Ag^+ towards the perovskite, and the I^- in the perovskite towards the silver [64]. Furthermore, Wojciechowksi et al. demonstrated that the hysteretic effect in a device is highly dependent on this interface, and appears to be caused by a charge accumulation and polarisation [65]. The correct engineering of the C_{60}-perovskite interface can significantly decrease issues of hysteresis, as it is crucial for consistent extraction of the carriers, which would imply an increase in stable PCE. Figure 5.6 presents local top views made with SEM of a sample configuration that includes the HTL, perovskite, ETL, HBL: [Glass, ITO, NiO, $CsPbI_2Br$, C_{60} and TmPyPb]. Figure 5.6 uses a magnification factor of 40k for the 165 nm and 80k for the 280 nm perovskite layer, in order to show the holes from both perspectives. Since C_{60} and TmPyPb are amorphous materials that follow the perovskite crystal structure, mainly the perovskite structure is visible in the top view. This top view analysis reveals by comparison that holes in the viewed layer are present independent of the perovskite thickness. Besides the presence of holes, it is impossible to measure the depth of the hole through SEM.

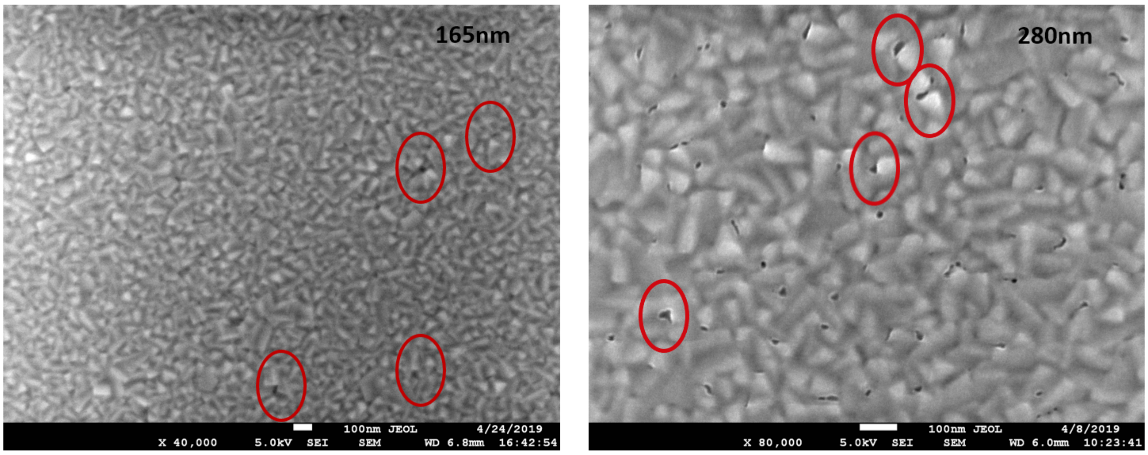

Figure 5.6: SEM top views of two samples with a varying perovskite thickness and C_{60}+TmTyPb

Figure 5.7 presents local top views of samples consisting only of the layers until the perovskite: [Glass, ITO, NiO, $CsPbI_2Br$]. The figure reveals an absence of holes in the layer for both cases. Comparing these results to Figure 5.6, it can be concluded that the C_{60} and TmPyPb are responsible for the non-uniform coverage of the perovskite layer. Furthermore, this implies that the holes found in Figure 5.6 do not originate from pinholes in the perovskite layers.

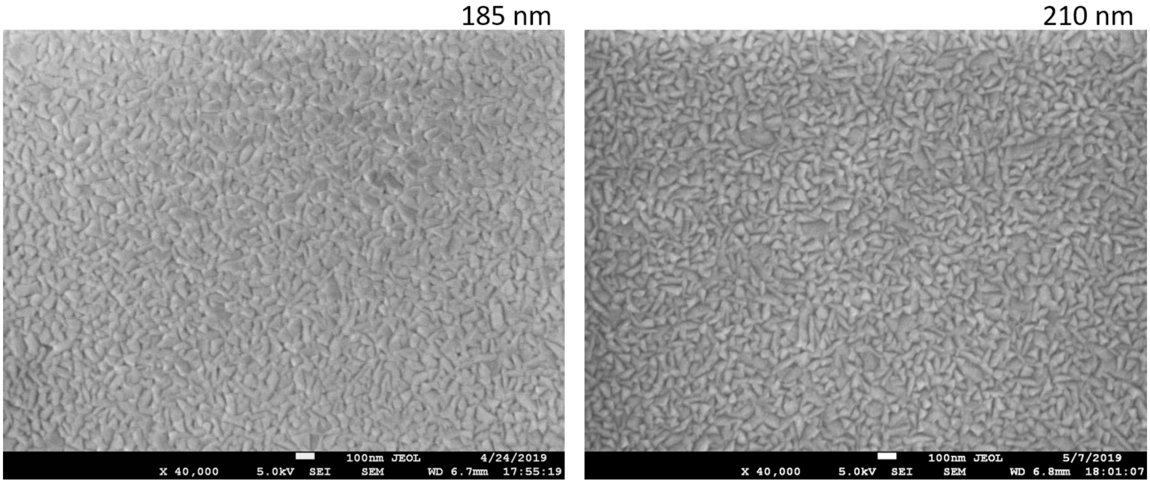

Figure 5.7: SEM top views of two samples with a varying perovskite thickness without C_{60}+TmTyPb

This hypothesis is confirmed by a TEM cross section of a sample configuration consisting of : [Glass, ITO, Spiro TTB, $CsPbI_2Br$ (20 nm), C_{60}, TmPyPb, and silver]. This cross section is presented in figure 5.8. The figure reveals the presence of silver in the C_{60} layer, as indicated by the white arrow. The cell was not subjected to any electric bias before the TEM analysis. Ag normally only diffuses through perovskite under a bias, as during operation conditions. Therefore, it can be concluded that the inclusion of silver in the C_{60} is induced by the initial presence of pinholes in the C_{60} layer [63].

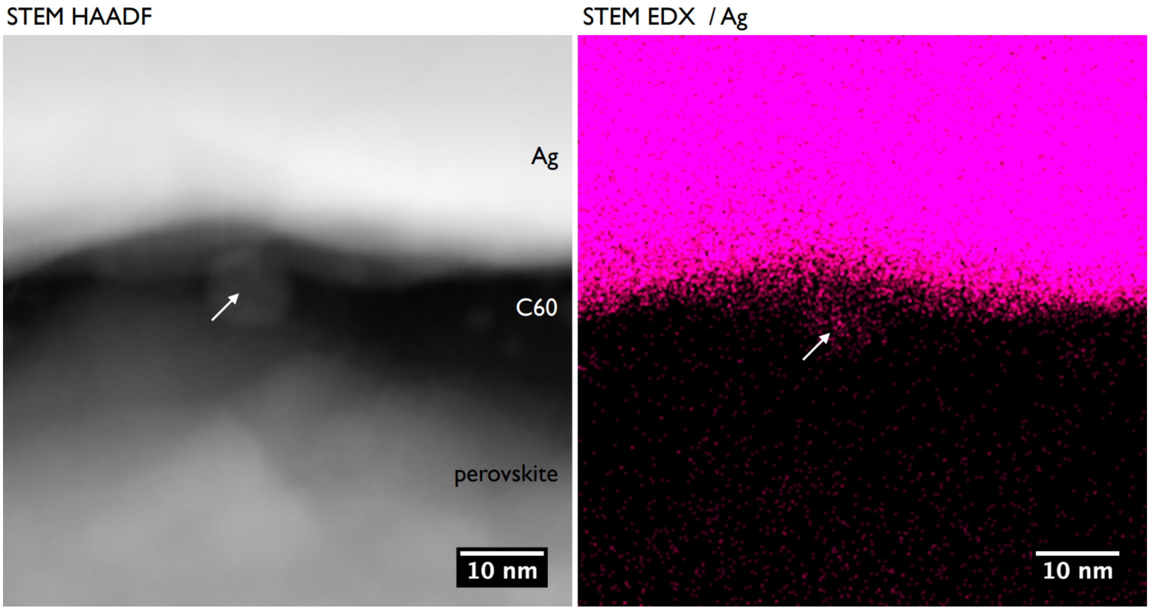

Figure 5.8: STEM high-angle annular dark-field and energy-dispersive X-ray imaging of Ag infiltration in C_{60}

In conclusion from these characterisations and observations, it is recommended to increase the thickness of the C_{60} layer from 20 nm to 30 nm to completely cover the perovskite layer. C_{60} layer engineering should result in a better fill factor. In order to test this recommendation, two similar batches were analysed, with the only difference between them being the varying thickness of the C_{60} layer from 20 nm to 30 nm. As seen in the results portrayed in figure 5.9, the cells with 30 nm of C_{60} not only attain an improved V_{oc} and FF, but also a slightly better J_{sc}. However, the collected data did not return a record V_{oc}, which can be attributed to issues with the sputtering of NiO across both batches, but the positive trend caused by the increase in C_{60} thickness remains evident.

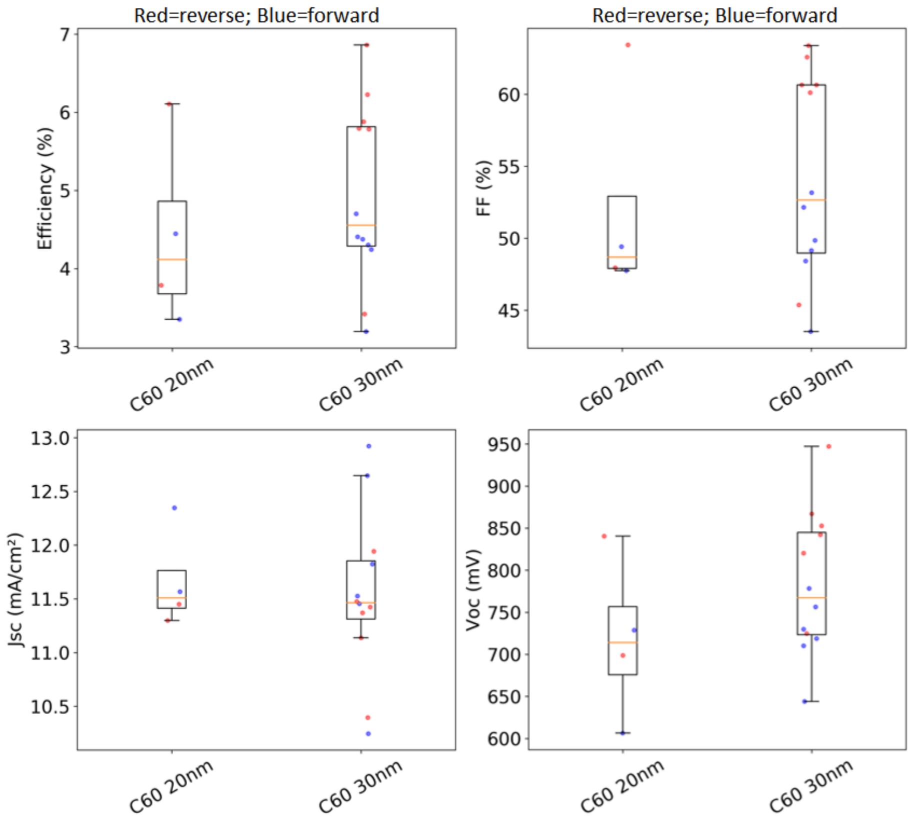

Figure 5.9: J_{sc}, FF, V_{oc}, and efficiency comparison for samples with 20 nm or 30 nm C_{60} layers

Finally, an SEM top view was made of the investigated cells with 20 nm and 30 nm of C_{60}, in order to compare the uniformity of their layers. Figure 5.10 depicts this comparison, from which it becomes clear that the configuration with 30 nm results in a more uniform layer.

An SEM top view of the cell with 30 nm of C_{60}, shows a more uniform layer, compared to the cell with 20 nm of C_{60}[vi].

[vi] The comparison also shows a difference in contrast/brightness; however, this can simply be linked to the settings of the SEM rather than to the layer itself.

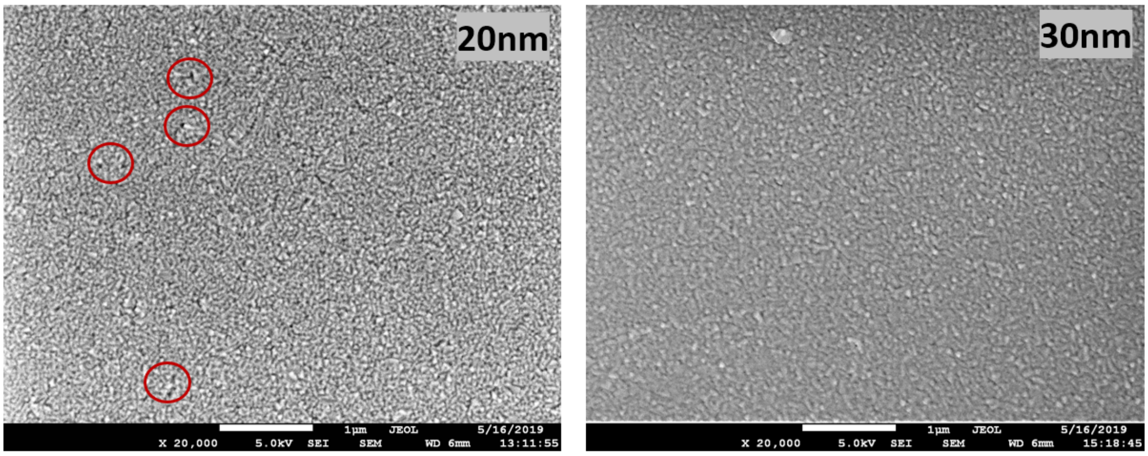

Figure 5.10: SEM top views of samples with a 20 nm or 30 nm C_{60} layer

The increased C_{60} thickness of 30 nm is maintained for the following sections, further allowing for higher and more stable V_{oc} and FF values.

5.5 Engineering of the hole transport layer

5.5.1 Optimising the thickness of the Spiro-TTB HTL

In this section, the thickness of the used Spiro-TTB layer is varied. As the absorption spectrum of Spiro-TTB has an overlap with the perovskite spectrum. The photon absorption by the photoactive layer can be improved by decreasing the covering influence of the Spiro-TTB through a decrease of thickness [62]. This hypothesis was tested by comparison of samples with 15 nm Spiro-TTB, as has been used before in this thesis, and samples with 10 nm of Spiro-TTB. The results of this comparison are graphed in figure 5.11. From this figure, it can be observed that there is a substantial increase in short circuit current density for the thinner Spiro-TTB, but the V_{oc} seems to slightly decrease with that. However, the fill factor and efficiency are generally similar, but the absolute highest efficiency was reached by a sample with 10 nm of Spiro-TTB. This cell is further described in section 5.7, as it attained the highest efficiency in a forward/reverse scan of this thesis. This high efficiency is confirmed by the highest mpp tracking obtained for solar cells on Spiro-TTB. Finally, it can be concluded that it is possible to obtain better PCE results for cells with a slightly reduced Spiro-TTB thickness.

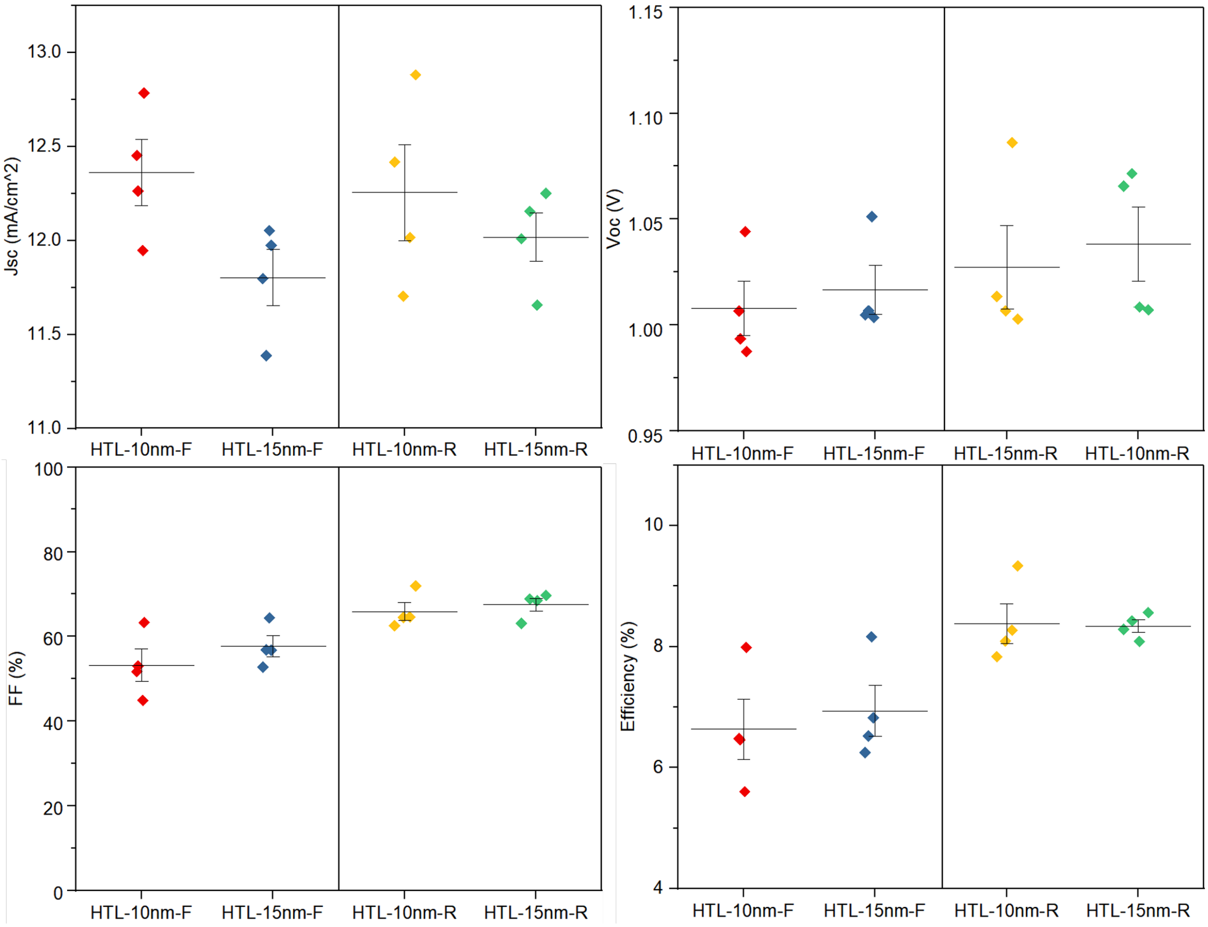

Figure 5.11: Forward- and reverse scan J_{sc}, FF, V_{oc}, and efficiency comparison for samples with a 10 nm or 15 nm Spiro-TTB layer

5.5.2 Spiro-MeOTAD or BF-DPB as HTLs

The bandgap of the investigated $CsPbI_2Br$ is around 1.92 eV, as discussed in section 4.4.2. Between samples with Spiro-TTB and with NiO, the best V_{oc} results were obtained using a Spiro-TTB HTL (of 1.1 V), as it presents a better band alignment. Encouraged by this increase in V_{oc} from NiO, experiments were done to investigate the application of two additional HTL materials, namely Spiro-MeOTAD and BF-DPB. The 'highest occupied molecular orbital'(HOMO) values of Spiro-MeOTAD and BF-DPB are respectively 5.2 eV and 5.25 eV [35, 66]. Theoretically, a different band-alignment between one of these and the perovskite could imply another increase in V_{oc}, and consequently a higher obtainable efficiency. However, the higher 'lowest unoccupied molecular orbital'(LUMO) values compared to perovskite bands could make them less well band-aligned.

Spiro-MeOTAD is used mainly for medium bandgap perovskite, but in the investigated cell its alignment with high-bandgap perovskite is tested. In this measurement, an open circuit voltage of 0.9 V was determined. Furthermore, the short circuit density current was lower than the cells based on Spiro TTB. In similar experiments, BF-DPB also showed an open circuit voltage of 0.9 V. However, it produced a short circuit current comparable to those seen in Spiro-TTB HTL samples. These findings are further illustrated by the EQE measurement portrayed in figure 5.12.

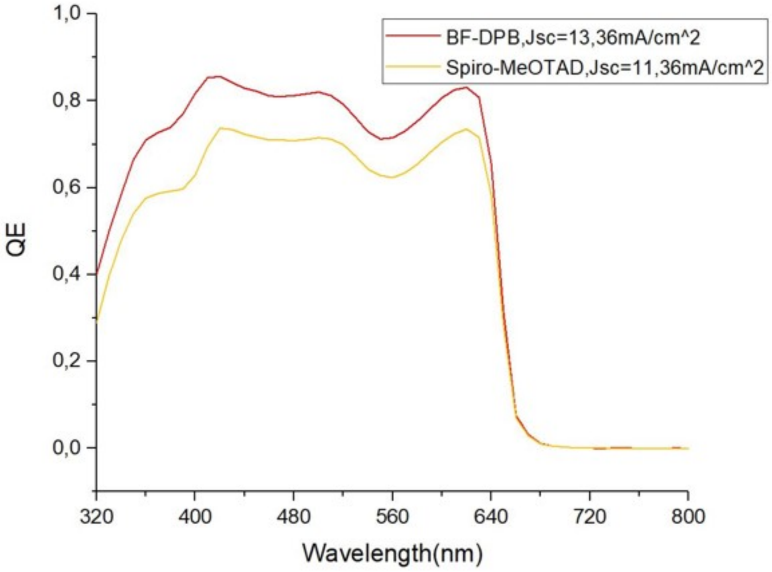

Figure 5.12: EQE comparison of a sample using a BF-DPB HTL and a sample using a Spiro-MeOTAD HTL

Another issue that both the Spiro-MeOTAD and the BF-DPB cell exhibit, is the remarkably rapid phase transition of the all-inorganic high-bandgap perovskite layer in exposure to air. The cells can be visibly degraded in less than 6 minutes. This degradation implies a critical decrease in cell conductivity. Figure 5.13 illustrates the visible degradation over time using samples with a 200 nm perovskite thickness.

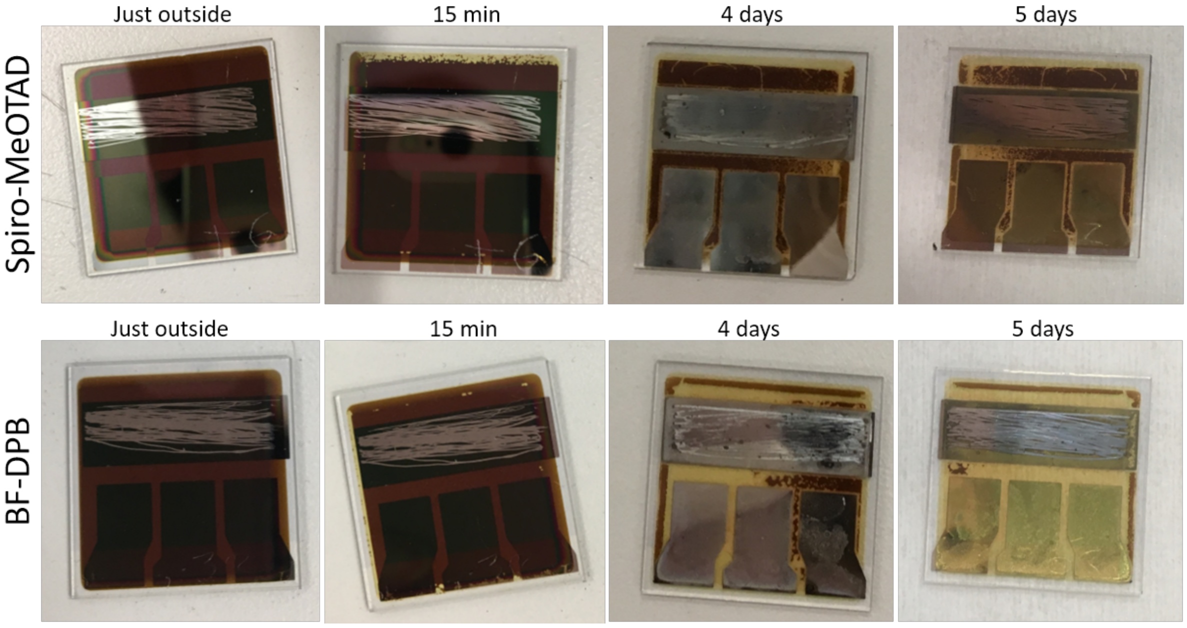

Figure 5.13: Macroscopic degradation at different points in time of samples using Spiro-MeOTAD or BF-DPB as HTL

The degradation of the bare BF-DPB+perovskite (200 nm) configuration is quicker than that of a complete cell, because the other layers on top of the perovskite protects it slightly from humidity. In figure 5.14 a side-by-side comparison illustrates the fact that a cell on Spiro-TTB is visibly less degraded than a cell on BP-DFB after 24 hours.

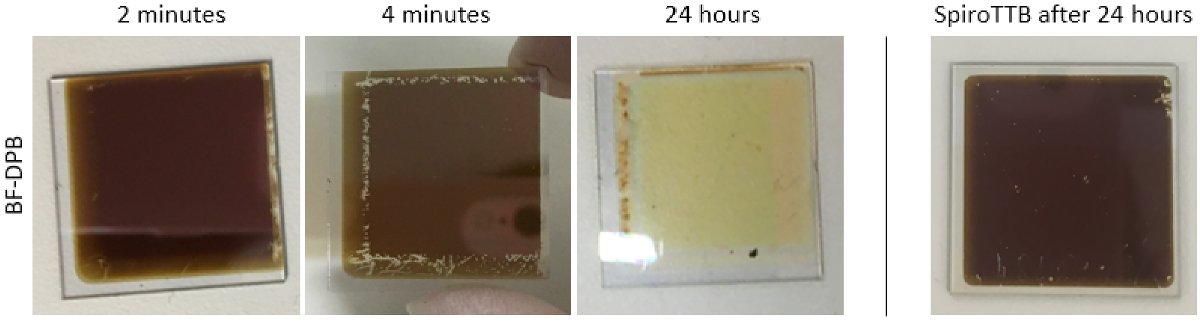

Figure 5.14: Macroscopic degradation of a BF-DPB+perovskite substrate compared to a Spiro-TTB+perovskite substrate

Different batches of BF-DPB confirmed the quick degradation of the perovskite layer, evidently influenced by the HTL.

5.6 Influence of annealing

5.6.1 Effect on efficiency

The cell configuration used for this section is as introduced in section 3.2, considering the Spiro-TTB as HTL. In this section, the layer thicknesses are: 10 nm for Spiro TTB, 190 nm for perovskite, 30 nm for C_{60}, 30 nm for TmPyPb, and 130 nm for silver. To investigate the effects of the annealing introduced in section 4.4.2 on the photovoltaic performance of a complete cell, the annealing steps at 80°C or 100°C for 10 minutes were integrated in the cell manufacturing process after the co-evaporation of the perovskite layer.

The V_{oc}, J_{sc}, FF, and efficiency of different cells were measured, as graphed in figure 5.15. The open circuit voltage of annealed cells appears to be more stable under air exposure. As discussed before, this should be due to the increased phase transition stability observed in section 4.1.1, since a slower degradation of the perovskite/ETL interface allows for a more stable V_{oc}. A negative effect of annealing seems to be a loss in the J_{sc}. This loss is already evident for the cells annealed at 80°C, and it increases for the cells annealed at 100°C. This is likely caused by the increased number of defects introduced in the perovskite layer during the annealing, as discussed in section 4.5. The efficiency values are higher for not annealed perovskite, meaning that the loss in J_{sc} is more significant than the small gain in V_{oc}. Finally, the FF shows the best values for not annealed cells and 80°C annealed cells alike.

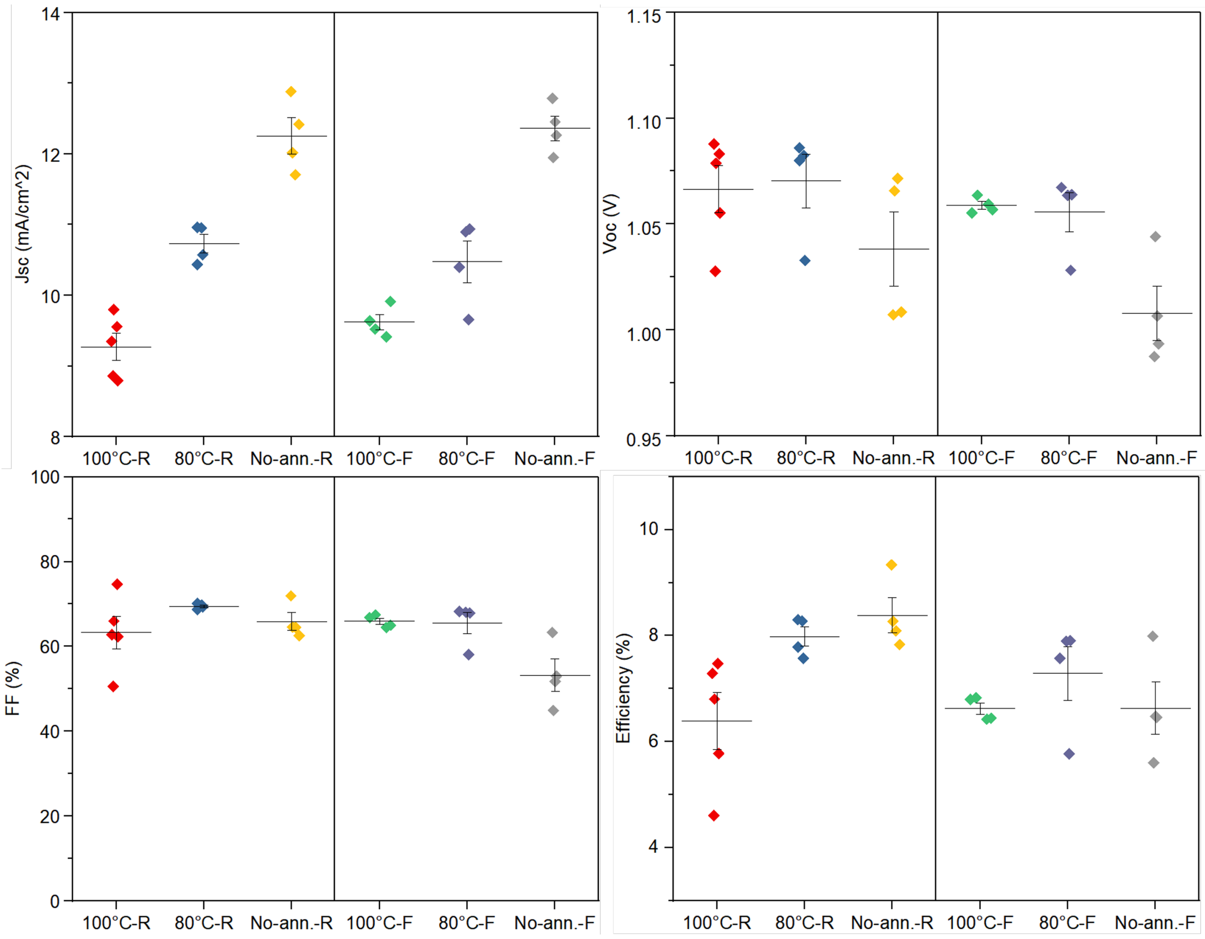

Figure 5.15: J_{sc}, FF, V_{oc}, and efficiency comparison for samples after varying annealing steps

Lastly, an EQE measurement confirms the negative effects on J_{sc} of the applied annealing, as portrayed in figure 5.16. In this figure, the EQE response of the not annealed cell, the 80°C annealed cell, and the 100°C annealed cell are depicted, from which it is visible that there is a decreased quantum efficiency with an increase in the annealing temperature.

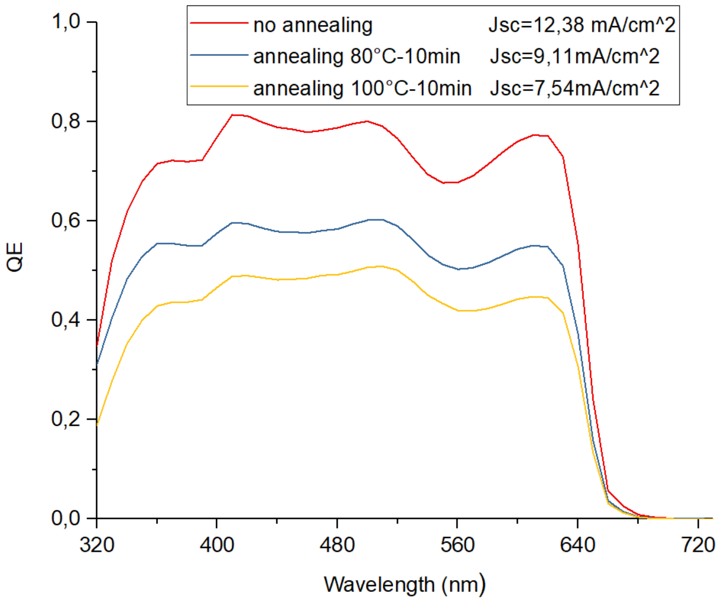

Figure 5.16: Comparison of EQE responses of samples with varying annealing steps

Although the experiment of this section only takes two different annealing temperature into account, the observed results can be put into perspective by literature. Zhang et al. noted that the annealing time of spin-coated all-inorganic CsPbI2Br was a key variable for variations in the J_{sc}, FF and V_{oc} of a cell [67]. These variables are negatively dependent on the annealing time, which was explained by the incorporation of O_2/H_2O traces in the perovskite grains during an annealing step, which causes extraction issues. This can be applied to the experiments of this section, hypothesising that the incorporation of these traces leads to traps in the material that decrease its electronic properties, starting from the J_{sc}. Therefore, as verified in section 4.5 and discussed by Zhang et al., no delta peaks appear in the XRD analysis of annealed samples, indicating an improved stability as compared to a not annealed cell, due to the absence of $\delta-$phase peak at 10°. However, there is also a lowered overall efficiency due to the increased number of traps. Furthermore, Chen et al. annealed samples of co-evaporated inorganic perovskite at 260°C for 10, 20, 40, 60, and 80 seconds, and obtained the best results for 60 seconds of annealing [54]. The PCE clearly depends on the time of exposure as shown by Chen et al., and on the temperature of annealing as observed from the analysis in this section.

5.6.2 Effect on phase transition

In order to avoid the phase transition n and allow for the realisation of high-performance devices, the most important factor to consider is the crystallisation of the perovskite. The formation of a crystalline perovskite structure is significantly influenced by an annealing process, such that different annealing processes can be applied to modulate the phase transition effects on a perovskite layer during air exposure. Through the right approach, a much slower degradation can be achieved [5]. Although co-evaporated perovskite does not strictly necessitate an annealing step due to the absence of a solvent in the material, the effects of an added annealing step on the perovskite grain structure are investigated in this section. Zhang et al. studied the effects of annealing on spin coated all-inorganic perovskite, and observed that the degradation rate did not seem to change significantly and no delta peaks are added in the XRD, but an increased number of traps were discovered in the material. Furthermore, Zhang et al. found a correlation between the number of traps in the material and the presence of traces of oxygen and humidity in the used glove box [67]. The latter was also independently observed by Lin et al., who noted that halide vacancies increase as cells are exposed to humid atmospheres [68]. This is explained by the high solvation enthalpy of the halides, thus a low energy is necessary for the creation of vacancies under influence of a solvent like H2O. The vacancy density in the affected material depends on the relative humidity. An AP-XPS analysis on spin coated inorganic perovskite showed that, after exposure to steam, the oxygen concentration at the surface of the cell is increased, but the effect did not penetrate throughout the depth of the cell[30].

In this section, the effects of annealing on samples with perovskite layers of 190 nm are analysed. The annealing investigated in this section was performed in a closed N2 atmosphere glove box, at 80°C and 100°C. Higher temperatures were chosen to be ignored, because they render the fully evaporated cell unsuitable for triple-junction purposes, as underlying layers could be damaged. Particularly temperatures above 140°C are strongly discouraged for the investigated cell composition, as the glass transition temperature of Spiro-TTB is at 146°C [69].

To investigate the effects of the performed annealing on the perovskite crystal structure in the samples, SEM top views were taken of a not annealed sample, a sample annealed at 80°C, and a sample annealed at 100°. The resulting pictures are shown in figure 5.17 at 40k magnification.

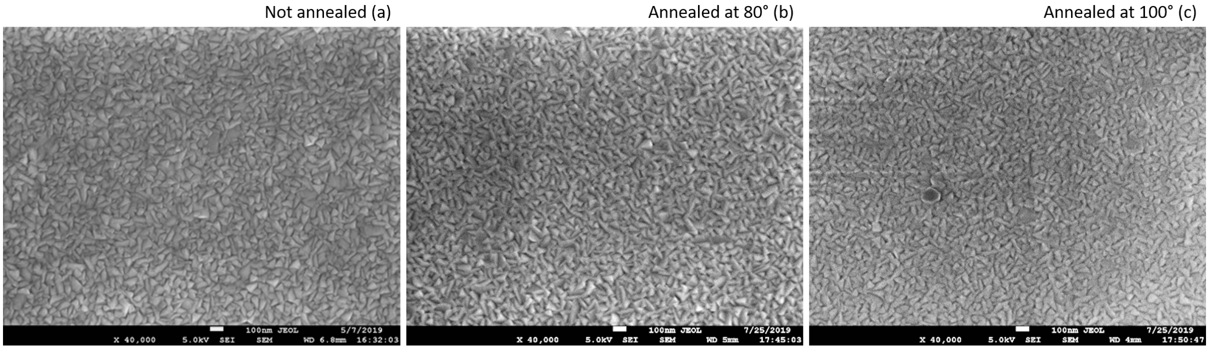
Not annealed (a)
Annealed at 80° (b)
Annealed at 100° (c)

Figure 5.17: SEM top views of samples after varying annealing steps

As seen in figure 5.17c, the sample that was annealed at 100°C exhibits an increased number of large individual grains. These grains could be delta phase grains, which would imply a reduction in the short circuit current density of the sample. The XRD analysis, as observed in section 4.5, confirmed the existence of variations in crystal structure among the samples subjected to different annealing processes. This change in crystal structure is macroscopically evident through the rate of degradation of the samples. Photographs of these visuals can be found in appendix A2, figure A2.1. The not annealed sample degrades visibly quicker than the annealed ones, and the phase transition is the slowest for the 100°C annealed samples.

5.7 Record cell results and analysis

The work done for this thesis, on fully evaporated solar cells with high bandgap $CsPbI_2Br$, yielded a record solar cell for three different configurations, one for each configuration introduced in 3.2, and one trial for a EBL+bi-HTL configuration designed to tackle the issues with BF-DPB described in section 5.5.2 above. These results are tabulated in table 5.1, and figures 5.18, 5.19, and 5.20 portray the J-V and the mpp tracking curves of respectively the NiO/perovskite based cell, the Spiro-TTB/perovskite based cell, and the EBL+bi-HTL trial cell. The latter has a precise configuration as follows: glass, ITO, MoO_3 3 nm, BF-DPB 4.7 nm, Spiro-TTB 4 nm, perovskite 190 nm, C_{60} 30 nm, TmPyPb 3 nm, silver 130 nm. For this cell, the MoO_3 was adopted as an electron blocking layer to improve the selectivity of the carrier extraction, in order to raise the J_{sc} and the V_{oc} values of the analysed cells. Furthermore, the BF-DPB HTL was used in combination with a Spiro-TTB cover, to avoid the degradation of the perovskite through the direct interface between it and the BF-DPB, as described in section 5.5.2. This configuration yielded notably positive results.

HTL material / Perovskite thickness	J_{sc} (mA/cm^2)	V_{oc} (V)	FF (%)	PCE (%) Fw / Rv	Stabilised PCE (%)
NiO / 165 nm	11.7	1.05	71.4	8.3 / 8.8	8.9
Spiro-TTB / 190 nm	12.88	1.01	71.7	8.0 / 9.3	8.82
bi-HTL* /190 nm	11.58	1.04	72.3	7.5 / 8.7	8.5

Table 5.1: Solar cell parameters of the best cells obtained during the analyses for this thesis (*BF-DPB and Spiro-TTB)

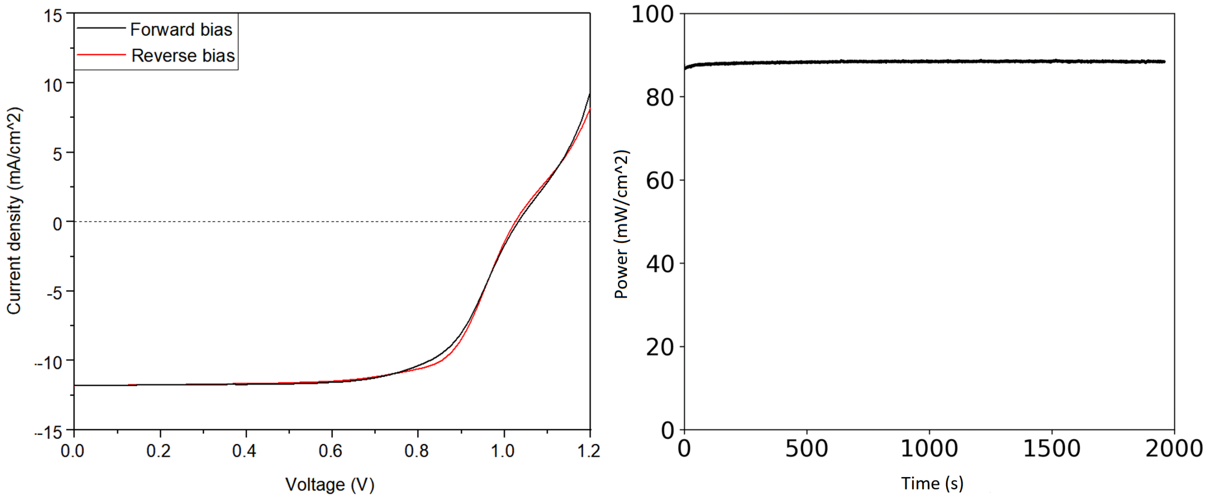

Figure 5.18: J-V and P_{mpp} curves of the best cell obtained using NiO as HTL

In figure 5.18, representing the NiO-HTL based cell, an S-shaped J-V curve is observed. This implies that there is a high series resistance, thus there are issues with the carrier extraction in the cell. This is a factor that has yet to be fully optimised.

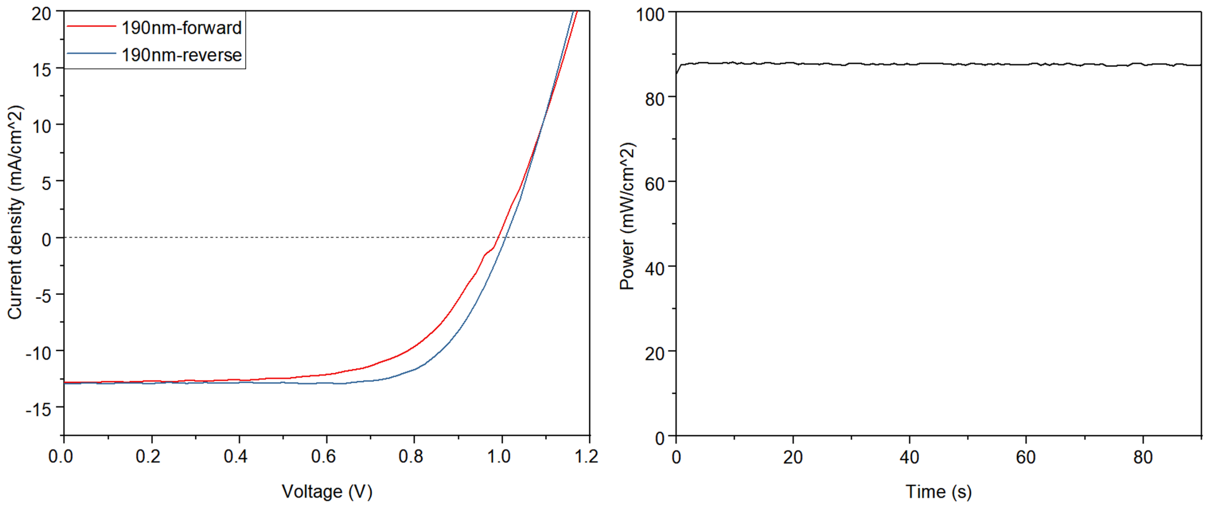

Figure 5.19: J-V and P_{mpp} curves of the best cell obtained using 10 nm Spiro-TTB as HTL

Figure 5.19, where the Spiro-TTB based cell is portrayed, shows low series resistance by the absence of an S-shape in the J-V curve. However, hysteretic effects are observed, as the forward and reverse J-V scans do not coincide. A theoretical method to improve this behaviour, based on the findings in this thesis, would be to improve the band alignments within the cell.

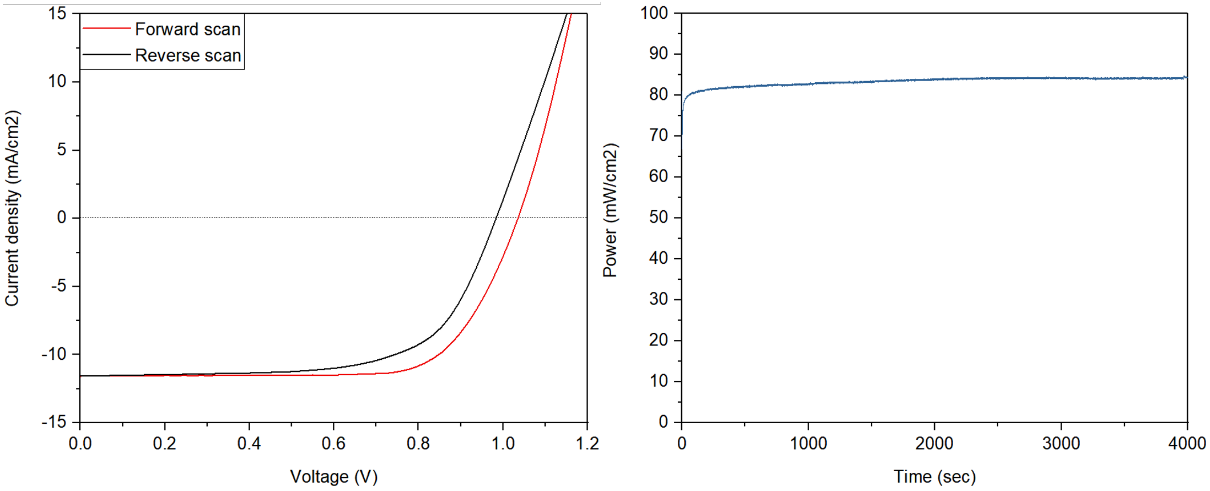

Figure 5.20: J-V and P_{mpp} curves of the best cell obtained using 3 nm of MoO_3 and a bi-HTL of 8.7 nm

Lastly, figure 5.20 represents the results of the trial cell using MoO_3, BF-DPB, and Spiro-TTB for a total thickness of 11.7 nm of EBL/HTL. The cell exhibits some hysteresis, but there is not S-shape in the curve. From the mpp tracking the positive influence of the MoO_3 on the stability of the cell can be observed, as it still shows a stable PCE after almost two hours. Furthermore, in contrast to the two cells above, the mpp tracking of this cell shows an initial drop of efficiency, as more clearly seen in the zoomed figure 5.21. This means that there is room for improvement by engineering the used layer thicknesses, after which an efficiency of 9% could theoretically be reached. This process, however, is beyond the scope of this thesis.

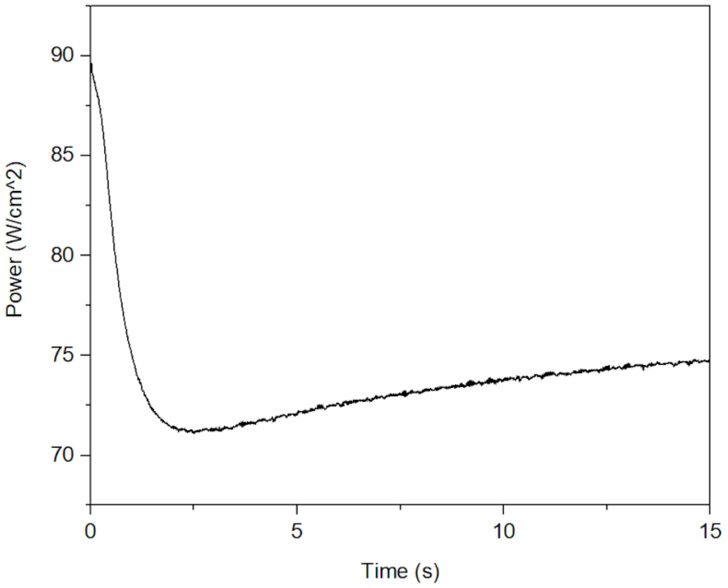

Figure 5.21: P_{mpp} curve of the first 15 seconds of measurement for the best cell obtained using 3 nm of MoO_3 and a bi-HTL of 8.7 nm

6 Conclusions and Discussion

6.1 Phase transition

Perovskite samples in an N_2-atmosphere do not degrade. Degradation occurs when the samples are exposed to air. Phase transition depends on the crystal structure of the $CsPbI_2Br$, and is driven by its hygroscopic nature. The thickness of the $CsPbI_2Br$ layer, an optional annealing process, and any neighbouring layers to the perovskite all have influence of the occurrence or rate of the phase transition. Increasing the thickness of the perovskite layer reduces the rate of its phase transition, as determined in section 5.1. This is possibly due to the lower surface area as relative to its volume, as the effects of air-exposure and humidity do not diffuse deeply in the layer and are rather confined to the surface. However, the use of perovskite does not allow for unlimited layer thickness, as the overpassing of the recombination limit can incur significant reductions in short circuit current density and power conversion efficiency. From section 5.6.2, it was determined that a possible improvement regarding phase transition seems to be an added annealing step to the manufacturing of the cell, although a final solution has not yet been found through this method. Therefore, it is recommended to conduct further investigations on this effect. Layers in direct contact with the perovskite layer can highly influence its rate of phase transition, as seen in section 5.5.2. A thorough investigation regarding the interactions between the perovskite and different interface materials can therefore be highly recommended. In this thesis it was observed that the use of Spiro-TTB or NiO as an HTL does not seem to cause a change in the degradation rate. As the driving factor behind phase transition is the presence of humidity and oxygen in the surroundings, another solution to combat the degradation is to encapsulate the cell under an inert atmosphere. Through this method, the perovskite characteristics will be preserved, as also observed by Mariotti et al. [5]. Additionally, Wang et al. suggested to protect the perovskite layer from humidity through a polymeric, hydrophobic, and thin tunnelling layer positioned between the perovskite layer and the C_{60} ETL, which could also help to reduce the frequency of carrier recombination [69]. Phase transition is strongly affected by the size and configuration of the ions in the perovskite crystal structure. When the tolerance factor of the perovskite is slightly lower than the required tolerance factor to have a stable cubic crystal structure, the perovskite exhibits a distorted cubic crystal structure. To inhibit the occurrence of this issue, the $CsPbI_2Br$ can be doped by a partial or full substitution of one ion, so that the material reaches the necessary tolerance factor to guarantee the stability of the alpha-phase. Several sources have performed investigations on this concept, noteworthy examples are: Nam et al. substitutes part of the A-site of the perovskite with potassium, to reach a stable lattice close to a cubic crystal structure [70]. Xian et al. substitutes part of the B-site with europium, the XRD pattern of the resulting material showed alpha peaks at the angles corresponding to a cubic structure, and the samples did not exhibit signs of degradation after six months at 40%RH, but they degraded in 100 hours when exposed to a higher relative humidity [71]. Yang et al. substitutes part of the B-site with germanium, resulting in an absence of delta-phase peaks in the XRD pattern of the resulting material, thus a higher phase transition stability. The samples did not degrade after 120 hours of exposure at 50-60% of relative humidity [72].

6.2 Phase segregation

The phenomenon of phase segregation is yet to be fully understood. Although its appearance throughout this thesis has been analysed from several perspectives and its dependencies have been investigated, the exact process of the phase segregation under photon excitation remains theoretical. A plausible explanation has been given at the hand of polarons and their influence [58, 73], which will be further discussed in this section.

Hoke et al. observed a difference in crystal structure between when a perovskite layer is illuminated and when it is not [57]. Bischak et al. explained the reversibility of the phenomenon with a polaronic model [58]. It was hypothesised that the created carriers induce phase segregation through photon-electron coupling during light exposure [58]. During this process, polarons are formed. An electron interacting with positive ions in polar semiconductors generates a self-induced potential at low temperatures, turning the electron into a polaron [74]. These polarons distort the surrounding lattice, and they have a lower mobility as compared to carriers [75]. The minimum Helmholtz free energy of the system is changed by these polarons, so that there is a different stable lattice, that minimises the free energy, for the illuminated and the dark conditions [58]. Miyata et al. and Nam et al. both sustain that $CsPbBr_3$ is subjected to large polaron and small polaron formation [76, 77]. It can be hypothesised that this phenomenon is also found in $CsPbI_2Br$. However, Zhang et al. observed a bandgap shift, akin to the phase segregation, in a $CsPbI_{1.8}Br_{1.2}$ nano-crystal after applying only a bias to it without any influence of injected carriers. As polarons are theoretically created by carriers, they are not solely responsible for this observed bandgap shift under bias. To account for this, the source of the phase segregation phenomenon is narrowed down to the hopping of ions in the lattice. For this movement to take place, the energy barrier constraining the ion to its position in the lattice needs to be overpassed. This energy barrier lies between 0.1 eV and 0.6 eV for $CsPbI_2Br$ [78]. This explains the connection between the phase segregation process under influence of a bias and the process under carrier injection, as they both change the available energy in the system and therefore enable the ions to overpass the aforementioned energy barrier. In inorganic perovskite the presence of caesium is responsible for relatively large structural distortions, as compared to MA and FA. Furthermore, iodide-lead bonds are generally less strongly distorted than bromide-lead bonds in the perovskite, due to the higher electronegativity of bromide [79]. The iodine consequently is more subjected to motions through the structure.

As proven by the experiments performed in section 4.4.2, phase segregation occurs noticeably quicker under influence of 10 sun laser intensity as compared to a 1 sun laser intensity. This observation can be explained through the polaronic model, as polarons are created from the injected carriers. High laser intensity induces the injection of a large number of carriers, which allows for the creation of more polarons as compared to lower laser intensities. It can be concluded that the polaron creation under photon excitation depends on the intensity of the employed laser beam.

As additionally shown in section 4.4.2, the phase segregation of an air-exposed sample is more rapid than that of one in an inert atmosphere. This is explained by the fact that the formation and the mobility of the polarons depends on the lattice dimensionality and coordination number [80]. When the sample is exposed to air, microscopic interactions at the surface between the perovskite layer and air influence the crystal structure by inducing degradation of the perovskite. This changes the coordination number, possibly causing a quicker phase segregation by allowing for more polarons to be created.

It was also determined from section 4.4.2 that phase segregation occurs less quick for thicker layers as compared to thinner layers. This can also be explained by the fact that the formation and the mobility of the polarons depends on the lattice dimensionality and coordination number [80]. For this, the dimensionality is important, which implies that phase segregation depends on the diffusion length. If the thickness of a layer overpasses the diffusion length of the material, the cross section of the layer is relatively less influenced by the created carriers than if the carriers would naturally diffuse throughout the entire thickness. Furthermore, the vertical gradient of carrier generated in the sample is more significant for thick layers, as the carrier injection is screened by the depth of the layer [2]. As the thick layers are relatively less affected by the carrier injection, relatively less polarons are created,so that the energy barrier for ion hopping is overpassed relatively less frequently. This could explain the slower phase transition of the thicker layers.

Although this thesis notably found that the investigated inorganic perovskite exhibits a quicker phase segregation for thin layers, it has been established before that organic perovskite shows the opposite. As thin layers of organic perovskite are able to screen and mediate charge interaction, they exhibit slower phase segregation as compared to thick layers [77]. However, in contrast to this, Gottesman et al. showed that the organic perovskite exhibits phase segregation due to the weakening of the bonds between the organic cation and the inorganic ions under light exposure [81].

In section 4.4.2 it was established that phase segregation occurs quicker at a second exposure of the same spot of the same sample. This could be interpreted as a proof of change in the crystal structure, which was not able to be regenerated during the period of darkness. A possible explanation was provided by Zhang et al., who proposed that the driving mechanism of phase segregation is the migration of a part of the iodide halides in the lattice towards empty sites at the surface, where they can evaporate [78]. These small losses in iodide in the lattice would make the full natural restoration of the original crystal structure impossible.

Annealed samples lose photoluminescence over time under light exposure, as found in section 5.6.2. This phenomenon could be explained by the increased occurrence of non-radiative recombination, due to the increased defect states introduced by the annealing [82]. In contrast, samples that were not annealed showed an increase in photoluminescence. Furthermore, it was found in section 4.4.2 that annealing influences the rate of phase segregation of a sample. This makes sense in the polaronic model, as annealing can introduce strains in the crystal structure through distortion and the introduction of defect atoms in the lattice, effectively changing the specific energy of the system. This change in energy then influences the formation of polarons. Particularly, defects in the lattice help the creation of small polarons, which are found to activate charge-trapping processes that decrease the photovoltaic properties of a device [79].

Through these observations, it seems plausible to link the PL shift of the $CsPbI_2Br$ under photon excitation to the formation and influence of polarons on the crystal structure. It can be suggested that stability of the perovskite is highly dependent on the homogeneity of the layer. Introducing a higher degree of homogeneity could help combat phase segregation. As implied in section 4.3, to improve the crystallinity of the material, the formation of a cubic structure should be facilitated. This implies a substitution of either the A or the B cation, to better match a symmetric cubic structure, effectively stabilising the perovskite. The precise effects are still to be investigated [60]. Furthermore, as found in section 5.6.2, the introduction of a specific strain through an annealing process could also help stabilise the cubic structure of the perovskite.

6.3 Device engineering

In order to optimise the solar cell configuration of this thesis, the HTL, perovskite layer and ETL were analysed. Firstly, the perovskite layer thickness was tuned to find an improved balance of the J_{sc}, V_{oc}, and FF, taking the extraction issues of the perovskite into account. From this analysis it was determined that the optimal layer thickness for co-evaporated, non-annealed $CsPbI_2Br$ in the employed configuration is 190 nm, as found in section 5.1. Secondly, the thickness of the C_{60} ETL was increased from 19 nm to 30 nm, in order to improve the uniformity of the layer in combination with the perovskite by decreasing the penetration of Ag through the layer towards the perovskite, as discussed in section 5.4. Thirdly, the properties of different HTL materials were investigated, namely Spiro-TTB, Spiro-MeOTAD, NiO and BF-DPB. The best results were obtained by sticking to Spiro-TTB and NiO, without visible differences in the rate of degradation of the perovskite layer, as determined in section 5.5.2. The Spiro-TTB HTL was further engineered in to achieve the best PCE of this thesis. The PCE obtained was 9.33% in reverse scan, with a stabilised PCE of 8.82%. For this, the Spiro-TTB thickness was reduced to 10 nm from 15 nm, in order to minimise the absorption of photons before they could arrive to the perovskite layer. The best cell achieved using a NiO HTL reached a stabilised PCE of 8.9%. Furthermore, after subjecting this cell to overnight light soaking, the efficiency remained stable. Lastly, an experiment was performed to investigate the effect of adding an extra HTL and an electron blocking layer on the phase stability of the perovskite. This resulted in a cell with a stabilised efficiency of 8.5%. From this result it can be concluded that the efficiency of a stable cell is notably improved through use of an HTL combination with better energy band alignment between the EBL and the perovskite with the perovskite that considers the recombination limit of the carriers.

Regarding possible future improvements, an investigation of the band alignment with perovskite of different interfaces is recommended. This could indicate that the use of more than one ETL and HTL in the same device is advantageous. This was also noted by Liu et al., who proposed a $ZnO@C_{60}$ bi-layer to replace the C_{60} layer, and observed a remarkable improvement of the efficiency of the spin coated $CsPbI_2Br$ solar cell [20]. This is explained through the improved band alignment and possibly a better adhesion to the perovskite layer.

Bibliography

[1] International Energy Agency, “Renewables 2018: Analysis and forecasts to 2023,” p. 10, 2018. [Online]. Available: www.iea.org/t{&}c/{%}0Ahttps://webstore.iea.org/download/summary/2312?fileName=English-Renewables-2018-ES.pdf{%}0Ahttps://www.oecd-ilibrary.org/energy/market-report-series-coal-2017{_}coal{_}mar-2017-en

[2] Q. Ma, “Perovskite Solar Cells via Vapour Deposition Processes,” 2017.

[3] C. Y. Chen, H. Y. Lin, K. M. Chiang, W. L. Tsai, Y. C. Huang, C. S. Tsao, and H. W. Lin, “All-Vacuum-Deposited Stoichiometrically Balanced Inorganic Cesium Lead Halide Perovskite Solar Cells with Stabilized Efficiency Exceeding 11%,” *Advanced Materials*, vol. 29, no. 12, pp. 1–7, 2017.

[4] C. G. Park, W. G. Choi, S. Na, and T. Moon, “All-Inorganic Perovskite CsPbI 2 Br Through Co-evaporation for Planar Heterojunction Solar Cells,” *Electronic Materials Letters*, vol. 15, no. 1, pp. 56–60, 2019. [Online]. Available: https://doi.org/10.1007/s13391-018-0095-1

[5] S. Mariotti, O. S. Hutter, L. J. Phillips, P. J. Yates, B. Kundu, and K. Durose, “Stability and Performance of CsPbI2Br Thin Films and Solar Cell Devices,” *ACS Applied Materials and Interfaces*, vol. 10, no. 4, pp. 3750–3760, 2018.

[6] K. Yoshikawa, H. Kawasaki, W. Yoshida, T. Irie, K. Konishi, K. Nakano, T. Uto, D. Adachi, M. Kanematsu, H. Uzu, and K. Yamamoto, “Silicon heterojunction solar cell with interdigitated back contacts for a photoconversion efficiency over 26%,” *Nature Energy*, vol. 2, p. 17032, mar 2017. [Online]. Available: https://doi.org/10.1038/nenergy.2017.32http://10.0.4.14/nenergy.2017.32

[7] A. Richter, M. Hermle, and S. W. Glunz, “Reassessment of the limiting efficiency for crystalline silicon solar cells,” *IEEE Journal of Photovoltaics*, vol. 3, no. 4, pp. 1184–1191, 2013.

[8] International Renewable Energy Agency, “Solar Photovoltaics,” 2012. [Online]. Available: http://ces.iitd.ac.in/html/solar{_}photovoltaics.html

[9] J. M. Pearce, “A Review of Solar Photovoltaic Levelized Cost of Electricity,” *Digital Commons @ Michigan Tech Department of Materials Science and Engineering*, no. April, 2018.

[10] A. Polman, M. Knight, E. Garnett, B. Ehrler, and W. Sinke, “Photovoltaic Materials - Present Efficiencies and Future Challenges,” *Science*, vol. 352, pp. aad4424–aad4424, apr 2016.

[11] NREL, “best-research-cell-efficiencies.20190802.pdf,” 2019. [Online]. Available: https://www.nrel.gov/pv/cell-efficiency.html

[12] T. Senthil and C. Kalaiselvi, “New Materials for Thin Film Solar Cells,” in *Coatings and Thin-Film Technologies*. IntechOpen, jan 2019, p. 13. [Online]. Available: https://www.intechopen.com/books/advanced-biometric-technologies/liveness-detection-in-biometricshttp://www.intechopen.com/books/trends-in-helicobacter-pylori-infection/

floating-drug-delivery-systems-for-eradication-of-helicobacter-pylori-in-treatment-of-peptic-ulcer-dh
//www.intechopen.com/books/coatings-and-thin-film-technologies/
new-materials-for-thin-film-solar-cells

[13] M. A. Green, E. D. Dunlop, D. H. Levi, J. Hohl-Ebinger, M. Yoshita, and A. W. Ho-Baillie, “Solar cell efficiency tables (version 54),” *Progress in Photovoltaics: Research and Applications*, vol. 27, no. 7, pp. 565–575, 2019.

[14] H. Megaw, “Crystal structure of barium titanate,” *Nature*, vol. 155, no. 3938, pp. 484–485, 1945.

[15] H. L. Wells, “On the caesium- and the potassium-lead halides,” *American Journal of Science*, vol. s3-45, no. 266, pp. 121–134, feb 1893. [Online]. Available: http://www.ajsonline.org/cgi/doi/10.2475/ajs.s3-45.266.121

[16] P. Reshmi Varma, *Low-Dimensional Perovskites.* Elsevier Inc., 2018. [Online]. Available: https://linkinghub.elsevier.com/retrieve/pii/B9780128129159000071

[17] A. Kojima, K. Teshima, Y. Shirai, and T. Miyasaka, “Organometal halide perovskites as visible-light sensitizers for photovoltaic cells,” *Journal of the American Chemical Society*, vol. 131, no. 17, pp. 6050–6051, 2009.

[18] H. S. Kim, C. R. Lee, J. H. Im, K. B. Lee, T. Moehl, A. Marchioro, S. J. Moon, R. Humphry-Baker, J. H. Yum, J. E. Moser, M. Grätzel, and N. G. Park, “Lead iodide perovskite sensitized all-solid-state submicron thin film mesoscopic solar cell with efficiency exceeding 9%,” *Scientific Reports*, vol. 2, pp. 1–7, 2012.

[19] R. J. Sutton, G. E. Eperon, L. Miranda, E. S. Parrott, B. A. Kamino, J. B. Patel, M. T. Hörantner, M. B. Johnston, A. A. Haghighirad, D. T. Moore, and H. J. Snaith, “Bandgap-Tunable Cesium Lead Halide Perovskites with High Thermal Stability for Efficient Solar Cells,” *Advanced Energy Materials*, vol. 6, no. 8, pp. 1–6, 2016.

[20] C. Liu, W. Li, C. Zhang, Y. Ma, J. Fan, and Y. Mai, “All-Inorganic CsPbI2Br Perovskite Solar Cells with High Efficiency Exceeding 13%,” *Journal of the American Chemical Society*, vol. 140, no. 11, pp. 3825–3828, 2018.

[21] L. Yan, Q. Xue, M. Liu, Z. Zhu, J. Tian, Z. Li, Z. Chen, Z. Chen, H. Yan, H. L. Yip, and Y. Cao, “Interface Engineering for All-Inorganic CsPbI 2 Br Perovskite Solar Cells with Efficiency over 14%,” *Advanced Materials*, vol. 30, no. 33, pp. 1–7, 2018.

[22] Geology Cafe, “Oceanography 101 Chapter 8 - Atmospheric Circulation,” 2016, accessed on 26-09-2019. [Online]. Available: http://www.geologycafe.com/oceans/chapter8.html

[23] “KINTEC Company,” accessed on 2019-07-25. [Online]. Available: http://www.kintec.hk/

[24] Sigma Aldrich and National Center for Biotechnology Information, “Molybdenum(IV) trioxide,” 2019, accessed on 03-09-2019. [Online]. Available: https://pubchem.ncbi.nlm.nih.gov/substance/24852067

[25] F. G. G. Riccardo, *Lumtec 2017 Product Catalog*, 2017.

[26] Luminescence Technology Corp., “LT-N138C Spiro-TTB,” accessed on 2019-07-25. [Online]. Available: http://www.lumtec.com.tw/portal{_}c1{_}cnt{_}page.

php?owner{_}num=c1{_}290785{&}button{_}num=c1{&}folder{_}id=32162{&}cnt{_}id=516344

[27] EPFL, “Available PVD Targets,” accessed on 2019-07-25. [Online]. Available: https://cmi.epfl.ch/thinfilms/targets.php

[28] Sigma Aldrich and National Center for Biotechnology Information, “Cesium Bromide 99.999% trace metals basis,” accessed on 2019-09-02. [Online]. Available: https://pubchem.ncbi.nlm.nih.gov/substance/24852042

[29] Alfa Aesar, “12724 Lead(II) iodide,” accessed on 2019-07-25. [Online]. Available: https://www.alfa.com/en/catalog/012724/

[30] Nano-c, “Fullerenes,” accessed on 2019-07-25. [Online]. Available: https://nano-c.com/nano-c-products/{#}fullerenes

[31] L. E. Polander, P. Pahner, M. Schwarze, M. Saalfrank, C. Koerner, and K. Leo, “Hole-transport material variation in fully vacuum deposited perovskite solar cells,” *APL Materials*, vol. 2, no. 8, p. 081503, aug 2014. [Online]. Available: http://dx.doi.org/10.1063/1.4889843http://aip.scitation.org/doi/10.1063/1.4889843

[32] C. Kulshreshtha, G. W. Kim, R. Lampande, D. H. Huh, M. Chae, and J. H. Kwon, “New interfacial materials for rapid hole-extraction in organic photovoltaic cells,” *Journal of Materials Chemistry A*, vol. 1, no. 12, p. 4077, 2013. [Online]. Available: http://xlink.rsc.org/?DOI=c3ta00808h

[33] J.-H. Jou, S. Kumar, M. Singh, Y.-H. Chen, C.-C. Chen, and M.-T. Lee, “Carrier Modulation Layer-Enhanced Organic Light-Emitting Diodes,” *Molecules*, vol. 20, no. 7, pp. 13 005–13 030, jul 2015. [Online]. Available: http://www.mdpi.com/1420-3049/20/7/13005

[34] C.-C. Chueh, C.-Z. Li, and A. K.-Y. Jen, “Recent progress and perspective in solution-processed Interfacial materials for efficient and stable polymer and organometal perovskite solar cells,” *Energy & Environmental Science*, vol. 8, no. 4, pp. 1160–1189, 2015. [Online]. Available: http://xlink.rsc.org/?DOI=C4EE03824J

[35] H. Xi, S. Tang, X. Ma, J. Chang, D. Chen, Z. Lin, P. Zhong, H. Wang, and C. Zhang, “Performance Enhancement of Planar Heterojunction Perovskite Solar Cells through Tuning the Doping Properties of Hole-Transporting Materials,” *ACS Omega*, vol. 2, no. 1, pp. 326–336, jan 2017. [Online]. Available: http://doi.wiley.com/10.1002/9780470166499.ch1https://pubs.acs.org/doi/10.1021/acsomega.6b00465

[36] K. S. Sree Harsha, *Principles of Vapor Deposition of Thin Films*, 2006.

[37] O. Malinkiewicz, A. Yella, Y. H. Lee, G. Minguez Espallargas, M. Graetzel, M. K. Nazeeruddin, and H. J. Bolink, “Perovskite solar cells employing organic charge-transport layers,” pp. 128–132.

[38] J. Borchert, H. Boht, W. Fränzel, R. Csuk, R. Scheer, and P. Pistor, “Structural investigation of co-evaporated methyl ammonium lead halide perovskite films during growth and thermal decomposition using different PbX2 (X = I, Cl) precursors,” *Journal of Materials Chemistry A*, vol. 3, no. 39, pp. 19 842–19 849, 2015.

[39] D. Zhao, W. Ke, C. R. Grice, A. J. Cimaroli, X. Tan, M. Yang, R. W. Collins, H. Zhang, K. Zhu, and Y. Yan, "Annealing-free efficient vacuum-deposited planar perovskite solar cells with evaporated fullerenes as electron-selective layers," *Nano Energy*, vol. 19, pp. 88–97, 2016. [Online]. Available: http://dx.doi.org/10.1016/j.nanoen.2015.11.008

[40] C. J. Brabec, V. Dyakonov, J. Parisi, and N. S. Sariciftci, Eds., *Organic Photovoltaics*. Berlin, Heidelberg: Springer Berlin Heidelberg, 2003. [Online]. Available: http://link.springer.com/10.1007/978-3-662-05187-0

[41] Ying-Tung Hsiao and China-Hong Chen, "Maximum power tracking for photovoltaic power system," in *Conference Record of the 2002 IEEE Industry Applications Conference. 37th IAS Annual Meeting (Cat. No.02CH37344)*, vol. 2, no. February 2002. IEEE, 2017, pp. 1035–1040. [Online]. Available: http://ieeexplore.ieee.org/document/1042685/

[42] G. Richardson, S. E. J. O'Kane, R. G. Niemann, T. A. Peltola, J. M. Foster, P. J. Cameron, and A. B. Walker, "Can slow-moving ions explain hysteresis in the current–voltage curves of perovskite solar cells?" *Energy & Environmental Science*, vol. 9, no. 4, pp. 1476–1485, 2016. [Online]. Available: http://xlink.rsc.org/?DOI=C5EE02740C

[43] D. A. Jacobs, Y. Wu, H. Shen, C. Barugkin, F. J. Beck, T. P. White, K. Weber, and K. R. Catchpole, "Hysteresis phenomena in perovskite solar cells: the many and varied effects of ionic accumulation," *Physical Chemistry Chemical Physics*, vol. 19, no. 4, pp. 3094–3103, 2017. [Online]. Available: http://xlink.rsc.org/?DOI=C6CP06989D

[44] L. Reimer, *Transmission Electron Microscopy*, 1997, vol. 36. [Online]. Available: http://link.springer.com/10.1007/978-3-662-14824-2

[45] A. Paar, "X-Ray Diffraction (XRD)." [Online]. Available: https://wiki.anton-paar.com/en/x-ray-diffraction-xrd/

[46] P. Jackson, R. Würz, U. Rau, J. Mattheis, M. Kurth, T. Schlötzer, G. Bilger, and J. H. Werner, "High quality baseline for high efficiency, Cu(In1-x,Gax)Se2 solar cells," *Progress in Photovoltaics: Research and Applications*, vol. 15, no. 6, pp. 507–519, sep 2007. [Online]. Available: http://doi.wiley.com/10.1002/pip.757

[47] M. Troviano and K. Taretto, "Urbach Energy In CIGS Extracted from Quantum Efficiency Analysis of High Performance CIGS Solar Cells," *24th European Photovoltaic Solar Energy Conference*, no. September, pp. 2933 – 2937, 2009.

[48] Cobolt, "Owner's Manual Cobolt Modulate DPSS Lasers," 2016.

[49] PerkinElmer, "LAMBDA™ UV/Vis/NIR and UV/Vis spectrophotometers – 950, 850, and 650," p. 8, accessed on 03-09-2019. [Online]. Available: https://www.perkinelmer.com/lab-solutions/resources/docs/BRO{_}Lambda950850650Americas.pdf

[50] A. Poglitsch and D. Weber, "Dynamic disorder in methylammoniumtrihalogenoplumbates (II) observed by millimeter-wave spectroscopy," *The Journal of Chemical Physics*, vol. 87, no. 11, pp. 6373–6378, 1987.

[51] H. Kronmuller and S. Parkins, *Handbook of Magnetism and Advanced Magnetic Materials*, 2007.

[52] C. Li, X. Lu, W. Ding, L. Feng, Y. Gao, and Z. Guo, "Formability of ABX 3 (X = F, Cl, Br, I) halide perovskites," *Acta Crystallographica Section B: Structural Science*, vol. 64, no. 6, pp. 702–707, 2008.

[53] P. S. Whitfield, N. Herron, W. E. Guise, K. Page, Y. Q. Cheng, I. Milas, and M. K. Crawford, "Structures, Phase Transitions and Tricritical Behavior of the Hybrid Perovskite Methyl Ammonium Lead Iodide," *Scientific Reports*, vol. 6, no. October, pp. 1–16, 2016. [Online]. Available: http://dx.doi.org/10.1038/srep35685

[54] C. Dong, X. Han, W. Li, Q. Qiu, and J. Wang, "Anti-solvent assisted multi-step deposition for efficient and stable carbon-based CsPbI 2 Br all-inorganic perovskite solar cell," *Nano Energy*, vol. 59, no. December 2018, pp. 553–559, 2019. [Online]. Available: https://doi.org/10.1016/j.nanoen.2019.02.075

[55] P. Becker, J. A. Márquez, J. Just, A. Al-Ashouri, C. Hages, H. Hempel, M. Jošt, S. Albrecht, R. Frahm, and T. Unold, "Low Temperature Synthesis of Stable γ-CsPbI 3 Perovskite Layers for Solar Cells Obtained by High Throughput Experimentation," *Advanced Energy Materials*, vol. 9, no. 22, p. 1900555, jun 2019. [Online]. Available: https://onlinelibrary.wiley.com/doi/abs/10.1002/aenm.201900555

[56] Q. Zeng, X. Zhang, C. Liu, T. Feng, Z. Chen, W. Zhang, W. Zheng, H. Zhang, and B. Yang, "Inorganic CsPbI 2 Br Perovskite Solar Cells: The Progress and Perspective," *Solar RRL*, vol. 3, no. 1, p. 1800239, 2019.

[57] E. T. Hoke, D. J. Slotcavage, E. R. Dohner, A. R. Bowring, H. I. Karunadasa, and M. D. McGehee, "Reversible photo-induced trap formation in mixed-halide hybrid perovskites for photovoltaics," *Chemical Science*, vol. 6, no. 1, pp. 613–617, 2015.

[58] C. G. Bischak, C. L. Hetherington, H. Wu, S. Aloni, D. F. Ogletree, D. T. Limmer, and N. S. Ginsberg, "Origin of Reversible Photoinduced Phase Separation in Hybrid Perovskites," *Nano Letters*, vol. 17, no. 2, pp. 1028–1033, 2017.

[59] A. J. Barker, A. Sadhanala, F. Deschler, M. Gandini, S. P. Senanayak, P. M. Pearce, E. Mosconi, A. J. Pearson, Y. Wu, A. R. Srimath Kandada, T. Leijtens, F. De Angelis, S. E. Dutton, A. Petrozza, and R. H. Friend, "Defect-Assisted Photoinduced Halide Segregation in Mixed-Halide Perovskite Thin Films," *ACS Energy Letters*, vol. 2, no. 6, pp. 1416–1424, 2017.

[60] D. J. Slotcavage, H. I. Karunadasa, and M. D. McGehee, "Light-Induced Phase Segregation in Halide-Perovskite Absorbers," *ACS Energy Letters*, vol. 1, no. 6, pp. 1199–1205, 2016.

[61] R. E. Beal, D. J. Slotcavage, T. Leijtens, A. R. Bowring, R. A. Belisle, W. H. Nguyen, G. F. Burkhard, E. T. Hoke, and M. D. McGehee, "Cesium Lead Halide Perovskites with Improved Stability for Tandem Solar Cells." *The journal of physical chemistry letters*, vol. 7, no. 5, pp. 746–51, 2016. [Online]. Available: http://www.ncbi.nlm.nih.gov/pubmed/26863290

[62] R. Kellermann, D. Taroata, A. Maltenberger, D. Hartmann, C. J. Brabec, and G. Schmid, "Low-cost copper complexes as p-dopants in solution processable hole transport layers," *Applied Physics Letters*, vol. 107, no. 10, 2015. [Online]. Available: http://dx.doi.org/10.1063/1.4930237

[63] Y. Kato, L. K. Ono, M. V. Lee, S. Wang, S. R. Raga, and Y. Qi, "Silver Iodide Formation in Methyl Ammonium Lead Iodide Perovskite Solar Cells with Silver Top Electrodes," *Advanced Materials Interfaces*, vol. 2, no. 13, pp. 2–7, 2015.

[64] C. C. Boyd, R. Cheacharoen, K. A. Bush, R. Prasanna, T. Leijtens, and M. D. McGehee, "Barrier Design to Prevent Metal-Induced Degradation and Improve Thermal Stability in Perovskite Solar Cells," *ACS Energy Letters*, vol. 3, no. 7, pp. 1772–1778, jul 2018. [Online]. Available: https://pubs.acs.org/doi/10.1021/acsenergylett.8b00926

[65] K. Wojciechowski, T. Leijtens, S. Siprova, C. Schlueter, M. T. Hörantner, J. T. W. Wang, C. Z. Li, A. K. Jen, T. L. Lee, and H. J. Snaith, "C60 as an efficient n-type compact layer in perovskite solar cells," *Journal of Physical Chemistry Letters*, vol. 6, no. 12, pp. 2399–2405, 2015.

[66] U. Hörmann, S. Zeiske, F. Piersimoni, L. Hoffmann, R. Schlesinger, N. Koch, T. Riedl, D. Andrienko, and D. Neher, "Stark effect of hybrid charge transfer states at planar ZnO/organic interfaces," *Physical Review B*, vol. 98, no. 15, p. 155312, oct 2018. [Online]. Available: https://link.aps.org/doi/10.1103/PhysRevB.98.155312

[67] S. Zhang, S. Wu, B. H. Babu, W. Chen, R. Chen, Y. Huang, Z. Yang, H. Zhu, and J. Zhou, "Adverse oxidation of CsPbI 2 Br perovskite during the crystallization process in an N 2 glove-box," *Journal of Materials Chemistry C*, vol. 7, no. 17, pp. 5067–5073, 2019.

[68] J. Lin, M. Lai, L. Dou, C. S. Kley, H. Chen, F. Peng, J. Sun, D. Lu, S. A. Hawks, C. Xie, F. Cui, A. P. Alivisatos, D. T. Limmer, and P. Yang, "Thermochromic halide perovskite solar cells," *Nature Materials*, vol. 17, no. 3, pp. 261–267, 2018. [Online]. Available: http://dx.doi.org/10.1038/s41563-017-0006-0

[69] T. P. Saragi, T. Fuhrmann-Lieker, and J. Salbeck, "Comparison of charge-carrier transport in thin films of spiro-linked compounds and their corresponding parent compounds," *Advanced Functional Materials*, vol. 16, no. 7, pp. 966–974, 2006.

[70] J. K. Nam, S. U. Chai, W. Cha, Y. J. Choi, W. Kim, M. S. Jung, J. Kwon, D. Kim, and J. H. Park, "Potassium Incorporation for Enhanced Performance and Stability of Fully Inorganic Cesium Lead Halide Perovskite Solar Cells," *Nano Letters*, vol. 17, no. 3, pp. 2028–2033, 2017.

[71] W. Xiang, Z. Wang, D. J. Kubicki, W. Tress, J. Luo, D. Prochowicz, S. Akin, L. Emsley, J. Zhou, G. Dietler, M. Grätzel, and A. Hagfeldt, "Europium-Doped CsPbI 2 Br for Stable and Highly Efficient Inorganic Perovskite Solar Cells," *Joule*, vol. 3, no. 1, pp. 205–214, 2019.

[72] F. Yang, D. Hirotani, G. Kapil, M. A. Kamarudin, C. H. Ng, Y. Zhang, Q. Shen, and S. Hayase, "All-Inorganic CsPb1-xGexI2Br Perovskite with Enhanced Phase Stability and Photovoltaic Performance," *Angewandte Chemie - International Edition*, vol. 57, no. 39, pp. 12 745–12 749, 2018.

[73] R. A. Belisle, K. A. Bush, L. Bertoluzzi, A. Gold-Parker, M. F. Toney, and M. D. McGehee, "Impact of surfaces on photoinduced halide segregation in mixed-halide perovskites," *ACS Energy Letters*, vol. 3, no. 11, pp. 2694–2700, 2018.

[74] J. T. Devreese, “Fröhlich Polarons. Lecture course including detailed theoretical derivations - 8th edition,” 2016. [Online]. Available: http://arxiv.org/abs/1611.06122

[75] F. Chevy, “Bose Polarons that Strongly Interact,” *Physics*, vol. 9, no. July, pp. 9–10, 2016.

[76] K. Miyata, D. Meggiolaro, M. Tuan Trinh, P. P. Joshi, E. Mosconi, S. C. Jones, F. De Angelis, and X. Y. Zhu, “Large polarons in lead halide perovskites,” *Science Advances*, vol. 3, no. 8, 2017.

[77] J. K. Nam, D. H. Chun, R. J. K. Rhee, J. H. Lee, and J. H. Park, “Methodologies toward Efficient and Stable Cesium Lead Halide Perovskite-Based Solar Cells,” *Advanced Science*, vol. 5, no. 8, 2018.

[78] H. Zhang, X. Fu, Y. Tang, H. Wang, C. Zhang, W. W. Yu, X. Wang, Y. Zhang, and M. Xiao, “Phase segregation due to ion migration in all-inorganic mixed-halide perovskite nanocrystals,” *Nature Communications*, vol. 10, no. 1, pp. 1–8, 2019.

[79] A. Mahata, D. Meggiolaro, and F. De Angelis, “From Large to Small Polarons in Lead, Tin, and Mixed Lead-Tin Halide Perovskites,” *Journal of Physical Chemistry Letters*, vol. 10, no. 8, pp. 1790–1798, 2019.

[80] J. P. Hague, P. E. Kornilovitch, A. S. Alexandrov, and J. H. Samson, “Effects of lattice geometry and interaction range on polaron dynamics,” *Physical Review B - Condensed Matter and Materials Physics*, vol. 73, no. 5, 2006.

[81] R. Gottesman, L. Gouda, B. S. Kalanoor, E. Haltzi, S. Tirosh, E. Rosh-Hodesh, Y. Tischler, A. Zaban, C. Quarti, E. Mosconi, and F. De Angelis, “Photoinduced reversible structural transformations in free-standing CH3NH3PbI3 perovskite films,” *Journal of Physical Chemistry Letters*, vol. 6, no. 12, pp. 2332–2338, 2015.

[82] F. Wang, S. Bai, W. Tress, A. Hagfeldt, and F. Gao, “Defects engineering for high-performance perovskite solar cells,” *npj Flexible Electronics*, vol. 2, no. 1, 2018. [Online]. Available: http://dx.doi.org/10.1038/s41528-018-0035-z

Appendix

A1 Visually degraded perovskite sample

Figure A1.1: A visually degraded 190 nm perovskite sample after long-term air-exposure

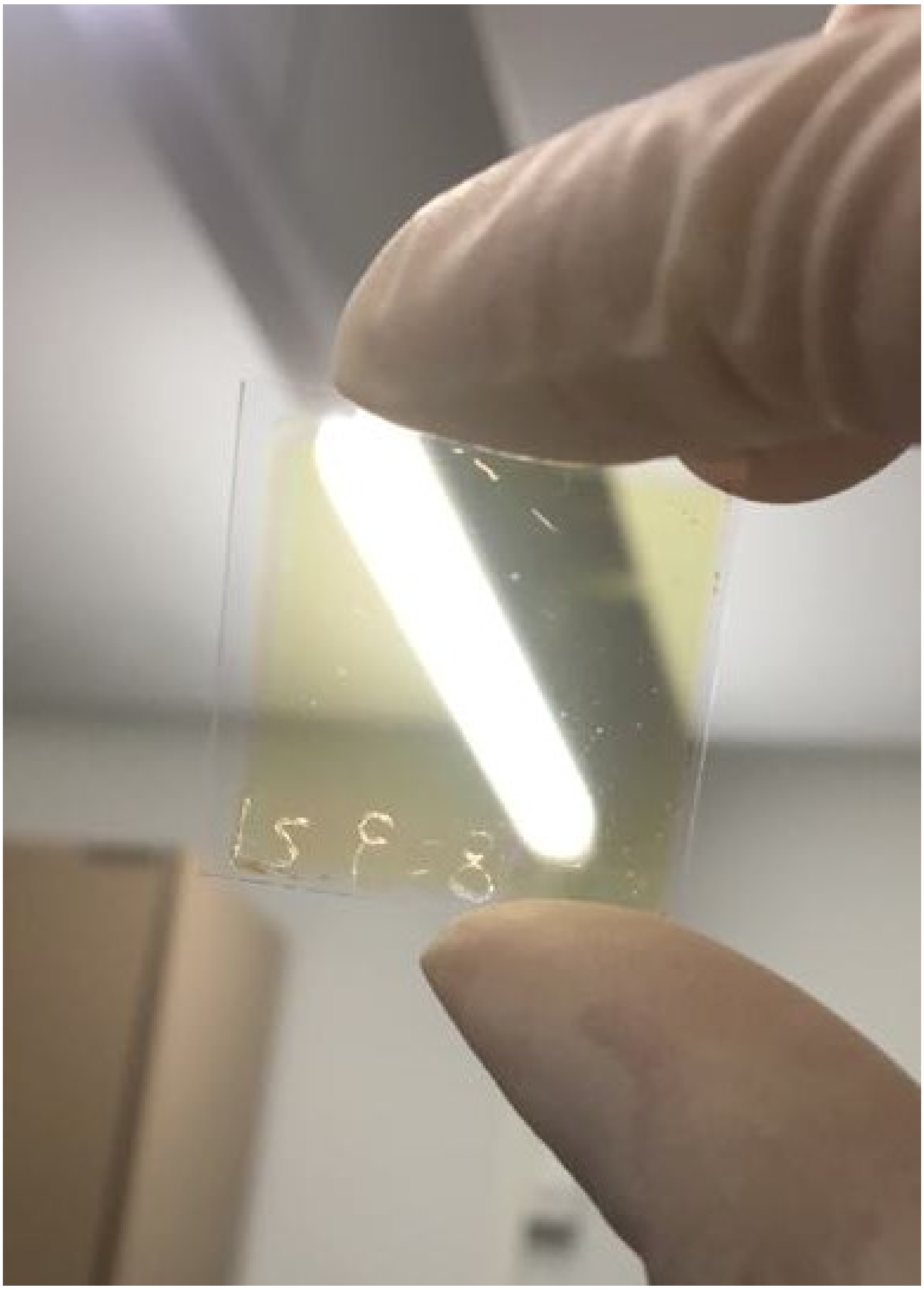

A2 Visual differences in degradation of annealed samples

Figure A2.1: Visual differences in degradation after a period of air-exposure of samples annealed at different temperatures